



CENTRO DE INVESTIGACIONES
EN ÓPTICA, A.C.

Study of interaction effects of quantum dots and gold nanoparticles with cells by Raman spectroscopy and advanced microscopy



DOCTORADO EN CIENCIAS (ÓPTICA)

Asesores: Dra. Tzarara López Luke

Dr. Elder de la Rosa Cruz

Estudiante: Elisa Iseth Cepeda Pérez

*Septiembre de 2016
León, Guanajuato, México*

Dedication

To Julia, my little princess.

Study of interaction effects of quantum dots and gold
nanoparticles with cells by Raman spectroscopy and advanced microscopy

by

Elisa Iseth Cepeda Pérez, M.Eng.

DISSERTATION

Presented to the Evaluation Committee of
Centro de Investigaciones en Óptica A.C.

in Partial Fulfillment
of the Requirements
for the Degree of

DOCTOR IN SCIENCE, OPTICS
CENTRO DE INVESTIGACIONES EN ÓPTICA A.C.

2016

ACKNOWLEDGEMENTS

I would like to sincerely thank my advisor and co-advisor, Dr. Tzarara López Luke and Dr. Elder de la Rosa Cruz for their constant support, intellectual guidance, inspiration, funding, and for introducing me to the world of nanoparticles and Raman spectroscopy. I would like to express my special gratitude to M.S Leonardo Pérez Mayén (CIO), Dr. Germán Plascencia (UTSA), Dr. Arturo Ponce (UTSA) and Dr. Jin Zhang (UCSC), for their expert suggestions, guidance and inspiration through various stages of this work. I thank to all the collaborators, including Dr. Valeria Piazza (CIO), Dr. David Monzón (CIO), Dr. Juan Vivero (UNCC), Dr. Miguel Yacaman (UTSA), Dr. Pedro Salas (UNAM-CFATA), Dr. Andrea Ceja (CIO), M.S. Iris Aguilar (ITESM), Dr. Ramón Carriles (CIO), Dr. Nancy Ornelas (CAALC), Dr. Ana Lilia González (UG), Dr. Alejandro Torres-Castro (UANL) and Dr. Alberto Hidalgo (CNR) for their support and contribution during the research work. I would also like to thank the students Patricia Tavares, Fabricio Gomez, Marco Antonio Cueto, Fernando Durán, Nayeli López, Miryam Torres and Eduardo Hernández for their valuable laboratory assistance. Thanks to all lab members of the GNAFOMA nanomaterials group. I am grateful to all the evaluation committee members, Dr. Juan Luis Pichardo (CIO) and Dr. Edgar Álvarez Zauco (UNAM). Additionally, I would like to thank laboratory technicians Christian Albor and Martin Olmos for their constant support and formidable attitude. I would also like to acknowledge the Mexican Council for Science and Technology, CONACYT for the national scholarship # 252054 and project # 230785. I appreciate the support through the projects CIO-UGTO 2013-2015, CeMIE-SOL 27 and 28, UC-MEXUS 2013, and BISNANO.

I am deeply grateful to my father José Isaac Cepeda, my mother María del Mar Pérez and José Carlos Moreno Hernández, for their constant support and inspiration. I extend my thanks to all my family members including my sisters, brothers, nephew and in-laws. I would like to thank all the people that have contributed in some way during these years.

Foreword

At present quantum dots and gold nanoparticles are widely used in bio-applications due to their size and highly efficient optical properties. The present work is focused on the study of the interactions of these materials at a cellular level. The results of this research show the way of internalization and adsorption of thioglycolic acid (TGA) capped CdTe quantum dots (TGA@CdTe QDs) into human and plant cells together with a systematic Raman spectroscopy study of their interaction with cellular molecules. Raman spectroscopy is carried out through the use of gold nanoparticles as nanosensors for SERS biomolecule detection. Naked gold nanoparticles are used to assess the interactions of the TGA@CdTe QDs with the cells whereas the SERS activity of Au/SiO₂ clouds in powder is studied for tissue applications.

The localization and interaction of TGA@CdTe QDs within the extracellular matrix (ECM) of *Haematococcus pluvialis* (Chlorophyceae) microalgae (HPM) after an incubation period of five minutes is presented. Changes in the Raman spectrum of HPM induced by the adsorption of the TGA@CdTe QDs are successfully found by using naked gold anisotropic structures as nano-sensors for the SERS effect. Raman spectroscopy results show that TGA@CdTe QDs interact with the biomolecules present in the ECM. Sample preparation and characterization by complementary techniques such as confocal and electron microscopy are also used to confirm the presence and localization of the nanoparticles in the algae. Stressed *Haematococcus Pluvialis* Microalgae (SHPM) are used as control sample since they do not present an ECM. Compared with the HPM samples, a small amount of TGA@CdTe QDs is observed on the outside of the secondary cell wall of SHPM. Therefore, it is proposed that the secondary wall prevents or reduces the interaction of QDs with the cells.

The internalization mechanisms of QDs for the variety of freshly extracted, not cultivated human cells and their specific molecular interactions remains an open topic for discussion. In this study, we also assess the internalization mechanism of TGA@CdTe quantum dots (3 nm) into non cultivated oral epithelial cells obtained from healthy donors. Naked gold nanoparticles (20 nm) are successfully used as nanosensors for surface-enhanced Raman spectroscopy to efficiently identify characteristic Raman peaks, providing new

evidence indicating that the first interactions of these QDs with epithelial cells occurred preferentially with aromatic rings and amine groups of amino acid residues and glycans from trans-membrane proteins and cytoskeleton. Using an integrative combination of advanced imaging techniques, including confocal microscopy, ultra-high resolution SEM, high resolution STEM coupled with EDX spectroscopy together with the results obtained by Raman spectroscopy, it is determined that TGA@CdTe QDs are efficiently internalized into freshly extracted oral epithelial cells only by facilitated diffusion, distributed into cytoplasm and even within the cell nucleus in three minutes. This research shows new evidence on early accumulation of QDs in plant and human cells and would further improve our understanding about their environmental impact.

In addition, Au/SiO₂ powder and gold nanoparticles in colloidal solution are synthesized and their morphology, optical, and the SERS properties have been characterized. In tissues breaded with Au/SiO₂ powder, several characteristic peaks frequently used for the diagnosis of adenocarcinoma in breast tissue and carious dental tissue in the range of the Amide III are successfully enhanced. The SERS activity of Au/SiO₂ is attributed to the properties of the silica powder structures to interact with tissue components, particularly its propensity to rehydrate in contact with the tissues promoting the formation of clusters of gold nanoparticles and also allowing the adsorption and interaction with biomolecules. Sample preparation and characterization by complementary techniques such as electron microscopy are also used to confirm the attachment of the Au/SiO₂ powder and image their locations on the tissues.

As an additional part to this research a focused ultrasound system for cellular sonoporation experiments is designed, built and tested. By means of this system it is expected that future experiments to conduct a controlled internalization of nanomaterials in cells can be performed.

Prefacio

Actualmente, tanto puntos cuánticos como nanopartículas de oro son ampliamente utilizados en bio-aplicaciones dado su tamaño y eficientes propiedades ópticas. El presente trabajo está dirigido hacia el estudio de las interacciones de estos materiales con el entorno celular. Los resultados de este estudio muestran la vía de internalización y/o adsorción de puntos cuánticos de CdTe cubiertos con ácido thioglicólico (TGA@CdTe QDs) en células animales y vegetales en conjunto con un estudio sistemático de sus interacciones con las bio-moléculas presentes en las células por medio de espectroscopia Raman. La detección de moléculas en espectroscopia Raman se llevó a cabo utilizando nanopartículas de oro como nano-sensores en SERS. De esta manera, nanopartículas de oro fueron empleadas para detectar las interacciones entre TGA@CdTe QDs y las células mientras que nubes de Au/SiO₂ en polvo fueron empleadas para estudiar tejidos.

Se estudió la localización y la interacción molecular por medio de los cambios en el espectro Raman de la microalga *Haematococcus pluvialis* (Chlorophyceae) (HPM) debidos a la presencia de TGA@CdTe QDs dentro de la matriz extracelular (ME) después de un periodo de incubación de cinco minutos. Los cambios en el espectro Raman fueron evidentes al utilizar nanopartículas de oro para obtener un incremento en la señal Raman conocido como efecto SERS. Los resultados de la espectroscopia Raman muestran que los TGA@CdTe QDs interactúan químicamente con las bio-moléculas presentes en la ME. La preparación de las muestras y su caracterización por medio de métodos complementarios como microscopía confocal y electrónica fueron empleados para confirmar la presencia y localización de las nanopartículas en las micro algas. Como muestra control se emplearon HPM estresadas (SHPM) debido a que estas no cuentan con una ME como la de las HPM. Una pequeña cantidad de TGA@CdTe QDs se observa en el exterior de la pared secundaria de las SHPM y con base en nuestros resultados experimentales se propone que esta pared secundaria previene o reduce la interacción de los TGA@CdTe QDs con estas células de planta.

Los mecanismos de internalización y las interacciones moleculares de TGA@CdTe QDs con la variedad de células humanas no cultivadas sino incubadas en fresco son ampliamente desconocidos y constituyen un tópico de interés actual. En este estudio se analizó el mecanismo de internalización de TGA@CdTe QDs en células orales epiteliales

humanas obtenidas de donadores sanos. De nueva cuenta, nanopartículas coloidales de oro fueron utilizadas para generar un realce en la señal Raman que permitió localizar los picos característicos de las células. De esta forma se encontró nueva evidencia que indica que las primeras interacciones de estos TGA@CdTe QDs con células epiteliales ocurren preferentemente con anillos aromáticos y grupos de amina de los residuos de aminoácidos y glicinas de proteínas tras-membrana y cito esqueleto. Mediante el uso de una combinación de técnicas avanzadas de imagen, incluyendo microscopía confocal, SEM y STEM de alta resolución acoplada con espectroscopia EDX, junto con los resultados obtenidos mediante espectroscopia de Raman, se determina que los TGA@CdTe QDs se internalizan eficazmente en las recién extraídas células epiteliales orales por difusión facilitada, de esta forma son distribuidos en el citoplasma e incluso dentro del núcleo de la célula en tres minutos. Esta investigación muestra nuevas evidencias sobre la acumulación temprana de los TGA@CdTe QDs en células humanas y vegetales, ampliando nuestra comprensión acerca de su impacto ambiental.

Como parte final de esta investigación, nanopartículas de oro embebidas en una matriz de SiO₂ (Au/SiO₂) en polvo y oro en solución coloidal se sintetizaron. Su morfología y características ópticas tales como actividad SERS para espectroscopia Raman fueron estudiadas sistemáticamente en tejidos *ex vivo*. En los tejidos empanados con polvo de Au/SiO₂, varios picos frecuentemente utilizados para el diagnóstico de adenocarcinoma en el tejido mamario y así como para el tejido dental cariado en el rango de la amida III se localizaron exitosamente. La actividad SERS de las nubes de Au/SiO₂ se atribuye a las propiedades de las estructuras de polvo de sílice para interactuar con los componentes del tejido, en particular su propensión a rehidratarse en contacto con los tejidos fomentando la adsorción de bio-moléculas y por otro lado promoviendo la formación de grupos de nanopartículas de oro. Nuevamente, la caracterización mediante técnicas complementarias, tales como la microscopía electrónica, se utilizaron para confirmar la fijación del polvo de Au/SiO₂ y sus ubicaciones en los tejidos.

Como parte adicional a esta investigación, un sistema de ultrasonido enfocado para experimentos celulares basados en sonoporación fue diseñado, construido y probado. Por medio de este sistema se espera llevar a cabo una serie de experimentos para internalización controlada de nano-materiales en las células.

Overview

This dissertation is organized into five chapters. Chapter one corresponds to an introduction, which provides a brief explanation about the Raman spectroscopic technique, the use of CdTe for biomedical applications, the cellular uptake processes and finally the uses of SERS powdered substrates for tissue diagnosis. Chapter two explains synthesis and characterization of thioglycolic acid capped CdTe quantum dots (TGA@CdTe QDs), naked anisotropic gold nanoparticles (AuNPs) and Au/SiO₂ powder. Chapter three describes the uptake, internalization and interaction of TGA@CdTe QDs and AuNPs with *Haematococcus Pluvialis* algae cells and human oral epithelial cells. In chapter four a systematic study of the SERS activity of Au/SiO₂ powder and AuNPs for tissue diagnosis is presented and discussed. Finally, the dissertation is summarized in chapter five with the possible future works in SERS and cellular uptake for biomedical applications. The experimental setup and preliminary experiments on cellular sonoporation mediated by focused ultrasound is presented in appendix A and the statistical and experimental description of microscopy and spectroscopy for cells and tissues is presented in appendix B.

This dissertation includes material from three published papers by the author. Chapters 2, 3 and 4 use materials from: *Interaction of TGA@CdTe Quantum Dots with an Extracellular Matrix of Haematococcus pluvialis Microalgae Detected Using Surface-Enhanced Raman Spectroscopy (SERS)*¹ coauthored with Iris Aguilar-Hernández, Tzarara López-Luke, Valeria Piazza, Ramón Carriles, Nancy Ornelas-Soto and Elder de la Rosa-Cruz, *SERS and integrative imaging upon internalization of quantum dots into human oral epithelial cells*² coauthored with Tzarara López-Luke, Germán Plascencia-Villa, Leonardo Perez-Mayen, Andrea Ceja-Fdez, Arturo Ponce, Juan Vivero-Escoto and Elder de la Rosa and *SERS-active Au/SiO₂ clouds in powder for rapid ex vivo breast adenocarcinoma diagnosis*³ coauthored with Tzarara López-Luke, Pedro Salas-Castillo, Germán Plascencia-Villa, Arturo Ponce, Juan Vivero-Escoto, Miguel José-Yacamán and Elder de la Rosa. Appendix A incorporates materials from the master's thesis by the author, entitled *Instrumentación y Control para un Sistema de medición de propiedades acústicas en materiales biológicos*⁴ and the poster *FUS SYSTEM FOR NON-DESTRUCTIVE TESTING IN BIOLOGICAL MATERIAL* presented at the ISEM-SOI 2015 conference coauthored with Patricia Tavares Ramírez, Tzarara López-Luke and Elder De la Rosa Cruz.

Table of contents

Acknowledgments	v
Foreword.....	vi
Prefacio.....	viii
Overview.....	x

Chapter one

Introduction

1.1 Quantum dots in biology, cellular interactions.....	1
1.2. Raman spectroscopy and SERS methods for cells and tissues.....	8

Chapter two

Synthesis, optical, structural and morphological characterization of TGA@CdTe QDs, naked gold nanoparticles and Au/SiO₂ powder

2.1 Thioglycolic acid capped CdTe quantum dots	15
2.1.1. Materials	
2.1.2. Synthesis of TGA-capped CdTe QDs	
2.1.3. Optical and morphological characterization	
2.2 Anisotropic naked gold nanoparticles.....	19
2.2.1. Materials	
2.2.2. Synthesis of naked and stabilized gold nanoparticles	
2.2.3. Optical and morphological characterization	
2.3. Optical characterization of the interaction between TGA@CdTe QDs and naked AuNPs.....	20
2.4. Gold nanoparticles embedded in SiO ₂ (Au/SiO ₂).....	22
2.4.1. Materials	
2.4.2. Synthesis of Au/SiO ₂ powders	
2.4.3. Optical characterization of Au/SiO ₂ powder	
2.4.4. Size, morphological characterization and elemental analysis	
Summary.....	28

Chapter three

SERS, integrative imaging and elemental analysis upon interaction of TGA@CdTe quantum dots with plant and human cells

3.1 Biological sample preparation and measurement standards.....	30
3.1.1. <i>Haematococcus pluvialis</i> microalgae cells.....	30
Morphological and optical characterization	
Optical imaging and Confocal Microscopy of algae samples	
Raman spectroscopy criteria for HPM	
3.1.2. Human oral epithelial cells.....	32
Extraction protocol for fresh cells	

Internalization of TGA@CdTe QDs in OECs	
Confocal and fluorescence microscopy	
Scanning and Transmission Electron microscopy and EDS	
Raman spectroscopy criteria for OEC	
3.2. Interaction of TGA@CdTe Quantum Dots with extracellular matrix of Haematococcus Pluvialis Microalgae	35
3.3. Interaction of TGA@CdTe quantum dots with human oral epithelial cells	44
Summary.....	53

Chapter four

SERS-active Au/SiO₂ powder for tissue diagnosis

4.1. Au/SiO ₂ clouds in powder for <i>ex vivo</i> breast adenocarcinoma diagnosis.....	55
4.1.1 Glandular breast tissue	
Breast adenocarcinoma samples	
Equipment and methods	
Raman spectroscopy	
4.1.2. SERS activity of Au/SiO ₂ clouds in glandular breast tissue	63
4.2. Au/SiO ₂ clouds in powder for dental tissue diagnosis.....	63
4.2.1. Dental tissue	
Sample preparation	
Equipment and methods	
4.2.2. SERS activity of Au/SiO ₂ clouds in dental tissue	70
Summary.....	70

Chapter five

Conclusions and future work.....	71
---	-----------

Appendix A

Focused ultrasound system for biomedical applications.....	74
---	-----------

Appendix B

Statistical and experimental description of microscopy and spectroscopy for cells and tissues.....	90
---	-----------

Chapter one

Introduction

In this introductory chapter a brief description of the methods employed and their medical applications as the motivation for this work are presented. The central objective of this work is the study of the interaction and internalization of thioglycolic acid (TGA) capped CdTe quantum dots (TGA@CdTe QDs) and naked gold nanoparticles with human and plant cells. For this two types of fresh cell have been selected; *Haematococcus pluvialis* microalgae cells and human oral epithelial cells. Raman spectroscopy is used as a tool to study the molecular interactions between the cells and the nanoparticles, specifically the Surface-Enhanced Raman Spectroscopy (SERS). The Raman study is complemented by an integrative set of microscopes and techniques; laser scanning confocal microscopy, fluorescence optical microscopy, ultra-high resolution scanning electron microscopy and scanning transmission electron microscopy. On the other hand, it is known that physical mechanisms such as focused ultrasound can control and modify the number of nanoparticles during the uptake process. A focused ultrasound system which is controlled via computer programming has been built and the principles of the uptake-modification method known as sonoporation are presented. As the final part of the work a SERS substrate for tissue diagnosis is developed.

1.1. Quantum dots in biology, cellular interactions

In recent years, the use of engineered nanoparticles in research and technology has increased rapidly.⁵ Thus at present, nanoparticles are commonly used in electronic devices, medical applications, cosmetics and food products.⁶⁻¹¹ In the case of biomedicine, nanomaterials have been employed as imaging tools, drug delivery carriers, nanosensors and gene delivery therapy.¹²⁻¹⁴ This development increases the chance of human exposure to nanoparticles due to their small size (1-100 nm), since they can potentially penetrate physiological barriers and invade all parts of the body, tissues, cells and even subcellular compartments.¹⁵ Therefore, some concerns have emerged because the exposure to some nanoparticles may lead to adverse health effects.¹³ A great interest in the understanding of the interactions of nanoparticles with

living cells has recently increased given the need to achieve their safe and beneficial use, and avoid possible biological hazards.¹⁶ In addition, nanoparticles with engineered surface properties, may pass through the cell membrane without disrupting it, enter directly into the cytosol thus interacting with other cellular components.^{15, 17} Within the different nanostructured materials Quantum Dots (QDs) are attractive for biotechnology applications, partially due to their optical properties. Among several other uses, QD have been used for long-term tracking of biological processes in living systems and biological imaging with reduced photo-bleaching.¹⁸ QDs are mostly synthesized in a non-polar organic solvent and therefore have a hydrophobic surface that often leads to aggregation in aqueous media, limiting their biological application.^{19, 20} Considering this problem, modified CdTe QDs are one of the most successful type of materials applied to biotechnology. CdTe QDs have been encapsulated or surface-modified with stabilizer thiols in order to prevent aggregation and increase water-solubility and biocompatibility.^{20, 21} Some CdTe QD stabilizer thiols are: thioglycolic acid (TGA), 3-mercaptopropionic acid (MPA) and mercaptoethanol (ME). TGA and MPA stabilized CdTe QDs have been tested in the most common buffers (pH=5-11) for the indirect immunofluorescence labeling of cells.^{5, 21, 22} Nevertheless, when CdTe QDs are used to decorate living cells, their toxicity represents a problem. It is believed that the main cause of CdTe QDs cytotoxicity is the generation of reactive oxygen species (ROS) caused by the release of Cd²⁺ ions, and the formation of TeO₂ and CdO.^{21, 23, 24} The addition of surface coatings to the QDs, such as ZnS, polyacrylate or dihydrolipoic acid, reduces the QD surface oxidation and the subsequent liberation of free Cd²⁺ improving the biocompatibility.^{21, 25} Some studies have concluded that, by conjugating CdTe QD with antioxidants, toxicity can be reduced.^{21, 24} It has been reported that Bovine Serum Albumin (BSA) could significantly decrease QD-induced toxicity.²⁴ The ability of quantum dots (QDs) to penetrate the membrane is mainly governed by their physical properties including size (< 10 nm), surface chemical composition and charge. QDs can be covalently bioconjugated to proteins and antibodies and electrostatically linked to DNA.^{5, 15, 26} Due to their optical and chemical properties, such as fine tunable fluorescence wavelength by nanoparticle size dependence, sharp

and symmetrical fluorescence peak, strong and stable emission, high quantum yield, brightness, photo-stability, and high resistance to photo-bleaching, making QDs a good choice for imaging probes.²⁰

The two most common types of QDs synthesis are the organometallic and aqueous synthesis. The organometallic route promotes QDs with excellent optical properties, but such organic synthesized QDs are of hydrophobic nature and cannot be directly used in bio-applications. This hydrophobicity often leads to irreversible aggregation and poor colloidal stability in aqueous media, thus limiting their biological application. Many different strategies to improve solubility of QDs have been introduced over the past few years.^{19, 20} Therefore a change of medium with hydrophilic ligands exchange and polymer or silica coating is required to obtain QDs with aqueous dispersibility. This involves complicated manipulations, that cause adverse effects on optical/ physical/chemical properties of the QDs.²⁷

The aqueous synthetic methods are known to be simpler, cheaper, and more environmentally friendly. The QDs synthesized by wet chemical methods are naturally water-dispersed without any posttreatment due to the presence of a large amount of hydrophilic ligand molecules. However, it has been reported that aqueous prepared QDs often possess poor optical properties and in both types of synthesis a high level of toxicity has been reported. The development of non-cytotoxic QDs for imaging, sensors and targeting has been of great interest.^{20, 28} As has been reported for CdTe QDs, surface oxidation leads to the formation of reduced Cd on the QD surface and the release of free cadmium ions, which is correlated with cell death. The cytotoxicity of QDs is not only caused by the nanocrystalline particle itself, but also by the thiol surface-covering molecules of the QD. When QDs are only present in the medium surrounding the cells, they cytotoxic effects are smaller compared to QDs ingested by cells. Recent research shows that TGA@CdTe QD toxicity is related to the release of free cadmium ions (Cd^{2+}), the formation of TeO_2 and the existence of CdO.^{23, 24} Free radicals and their interaction with individual cellular components result in cellular malfunction and eventually cause cell death.²⁴ Therefore, a considerable presence of Cd in cell samples could indicate QD toxicity due to Cd^{2+} ions. However, surface coatings such as ZnS, polyacrylate and dihydrolipoic acid reduces the QD surface oxidation and the subsequent release of free Cd^{2+} improving

biocompatibility.²⁴ The potential toxicity of CdTe QDs has been studied and it has been proposed that the use of antioxidants such as bovine serum albumin (BSA) could protect against the QD toxicity.²⁴

For instance, QDs have often been encapsulated or surface-modified in order to prevent aggregation and increase water-solubility and biocompatibility.^{18, 20, 25} One successful example is the CdTe owing to its strong photoluminescence (PL) in the visible region. Preparation techniques enable a facile aqueous synthesis of CdTe QDs capped by thiol groups whose photoluminescence covers most part of the visible region extending to the near IR with quantum yields of up to 70-80 %. This efficiency is similar to the best organometallic materials.²⁹

There are many reported biological experiments on the accumulation and internalization of thiol-capped QDs and these are most often performed with immortalized cell lines because they are often available and are reproducible. However it has been reported that cell lines differ from the *in vivo* extracted cells in many important aspects.³⁰ Immortalized cell lines are adapted to growth in culture and the lack of tissue architecture and heterogeneous population of cell types often precludes cell-cell interaction and secretion among other functions related to the membrane within a tissue context.³¹ As has been reported cell lines tend to lose tissue-specific functions and acquire a different molecular phenotype from cells *in vivo*. Moreover, it is known that cell lines and primary cells differ in protein levels and proteomes.³⁰ Thus animal experiments, studies in primary cell lines or fresh extracted cells are often preferred despite their complexity.³² It is why the present research is focused on the study of the interaction of fresh cells with QD. The work involves interactions with a plant and a human cell type.

A complete understanding of how a microalgae responds to adverse environmental conditions such as the presence of heavy metals³³ is an open issue and for the case of HPM has become critical due to the increasing interest in this organism as a biotechnological source of the ketocarotenoid astaxanthin.³⁴⁻³⁷ HPM display green color due to the high contents of photosynthetic pigments, chlorophyll and β -carotene.³⁴ Typical HPMs that have less than three weeks exhibit an extracellular matrix (ECM) of variable thickness that consists mostly of hydroxyproline-rich glycoproteins.^{38, 39} At these age HPMs show little to no

presence of the chemical non-enzymatic antioxidant astaxanthin, making them more susceptible to ROS.^{34, 40, 41}

The interaction of plant cells with TGA@CdTe QDs is studied in *Haematococcus pluvialis* (Chlorophyceae) Microalgae cells (HPM) which is a freshwater unicellular microalgae studied for its adaptive response under conditions of environmental stress such as nutrient depletion, high salinity, high light intensities, or the presence of reactive oxygen species.³⁷ Stressed *Haematococcus pluvialis* Microalgae (SHPM) undergo several morphological and biochemical changes.^{34, 37} When stress conditions are present, HPM grow a thick outer secondary wall, exhibit a decrease in chloroplasts and protein content, and accumulate astaxanthin, turning into red color cyst cells that have virtually lost all the ECM.^{38, 39, 42} A schematic diagram of the main differences between HPM and SHPM cells before and after applying stress conditions is shown in figure 1. Internalization of QDs in plant and algal cells is not common since QDs generally are adsorbed into the cell wall.¹⁰ In plants, the cell wall pore size ranges between 5 and 20 nm.⁴³ It has been stated that in certain algae species QDs can damage the wall and membrane and are known to generate reactive oxygen species within the microalgae, thus inducing the activation of enzymatic antioxidant systems.^{40, 43} For instance, it has been reported that higher oxidative stress is observed when microalgae are incubated with QDs.⁴¹

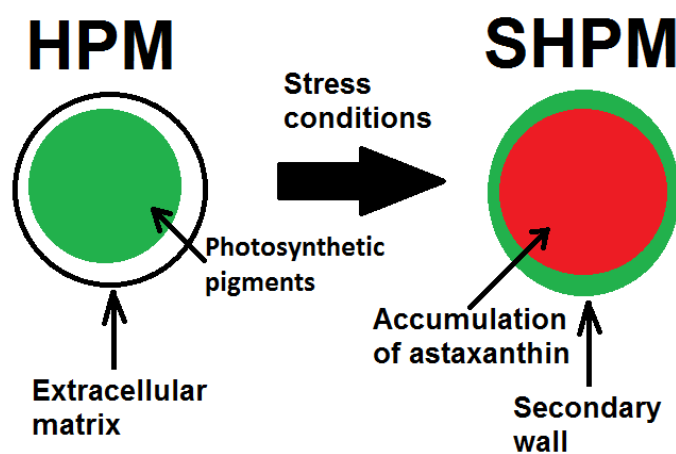


Figure 1. Schematic diagram showing the main differences between HPM and SHPM cells before and after applying stress conditions.

The interactions between eukaryotic animal cells and QDs have been studied in freshly extracted human oral epithelial cells. The principal patterns of epithelial differentiation are represented by keratinization and non-keratinization. These cells are located on the stratified squamous epithelium which consists of squamous epithelial cells arranged in layers upon a basal membrane. This type of epithelium is found in regions in which the tissue is subject to constant abrasion, and is structured in layers so that the upper layers can be sequentially sloughed off and replaced before the basement membrane is exposed. It can be found in the outermost layer of the skin and the inner lining of the mouth, esophagus, and vagina. For these type of cells, only one layer is in contact with the basement membrane while the other layers adhere to one another to maintain structural integrity. Although this epithelium is referred to as squamous, not all the cells within the layers are flattened and there are no intercellular spaces. The main function of non-keratinized surfaces is to prevent tissue from drying out.

The mucosal lining of the oral cavity and esophagus functions to protect the underlying tissue from mechanical damage and from the entry of microorganisms and toxic materials that may be present in the oropharynx. The epithelium is constantly replaced by cell division in the deeper layers, and turnover is faster in the lining than in the masticatory regions. As keratinocytes enter into differentiation, they become larger and begin to flatten and to accumulate cytokeratin filaments. In addition to the keratins, the differentiating keratinocytes synthesize and retain a number of specific proteins, including profilaggrin, involucrin, and other precursors of the thickening of the cell envelope in the most superficial layers. There is a rapid clearance of surface cells, which acts as a protective mechanism by limiting colonization and invasion of microorganism adherent to the mucosal surface. The early accumulation and uptake process of TGA capped CdTe QDs on fresh cells is largely unknown^{5, 21, 27} and as for the HPM their study requires the use of different microscopy methods.

During the development of this work various microscopy techniques have been used. In the following paragraphs the most commonly used microscopy methods that allow to study the presence and location of nanomaterials in cells are presented. At present fluorescence imaging has turned into a powerful tool in modern biological investigations due to the sensitivity and specificity of fluorescence measurements. Also the high-quality of

fluorescence probes and labeling protocols expanded its applications for studying molecular and cellular systems.⁴⁴ The simplest expression of fluorescence microscopy corresponds to the acquisition of images of a biological system using the fluorescence properties of the sample. However, there is much more information which comes from a deeper understanding of this fluorescence properties. By optimizing the excitation criteria, the image quality can be improved and this opens the door for a refined understanding of the sophisticated applications of fluorescence such as information regarding molecular and cellular processes. Fluorescence microscopy has played a key role in the biological and biomedical sciences because it provides biochemical, biophysical and the morphological status of cells and tissues. The development of new fluorescent probes together with the microscopy techniques such as multiphoton microscopy has boomed in recent years. In specific the research of engineered nano-fluorophores offers new alternatives for improvement for the entire field, due to the specific, tunable and excellent optical properties of these materials. Fluorescence microscopy has evolved over the last 30 years, electronic images are the typical output and the resolution and detector system have become constant research topics.⁴⁴

It is known that the response of single cells to a certain stimulus is often heterogeneous. Therefore, biochemical and physiological measurements acquired in two dimensions may fail to accurately represent the magnitude of individual cellular changes. To study the responses of single cells, sectioning approaches are needed. Confocal microscopy is one method to assess single cell physiology with high spatial and temporal resolution.⁴⁴

On the other hand electron microscopy offers structural and compositional information, with a high resolution. By transmission electron microscopy one can indentify the location and means of entry of materials for thin cellular samples at a nanometric scale.⁴⁵ When studying cell samples by electron microscopy, cell fixation is the most important step since little mistakes at this step may be reflected in wrong results and false data.⁴⁶ At first, the fresh cells should be immobilized and all biochemical processes must be halted to avoid changes in the ultrastructure. The fixative must be strong enough to avert the adverse affects of the dehydration and embedding procedures. Each fixative has its advantages and disadvantages. And it is known that primary fixation with glutaraldehyde and formaldehyde, followed by osmium tetroxide is the prefered sequence for ultrastructure preservation of

biological samples. Before sample preparation one must have some knowledge about the type cell, for example knowing what the ultrastructure of the living cell looks like. The final appearance of the cells should not be in conflict with the living appearance of it. This is why it is recommended to monitor the electron cellular imaging technique with other optical microscopy techniques. If the fixation process is carefully selected and studied, electron microscopy offers an excellent option to help monitor the location of engineered nanoparticles after cellular adsorption.

1.2. Raman spectroscopy and SERS methods for cells and tissues

Raman spectroscopy is a scattering spectroscopic technique based on the inelastic scattering of monochromatic light.⁴⁷ When a sample is excited with a monochromatic light most of the photons are elastically scattered with the same energy as the incident photons, this type of scattering is called Rayleigh scattering. However, a small fraction of the scattered photons (~ 1 in 10 million) come from an energetic interaction with the sample, so that the scattered photons have a different frequency than the incident photons.⁴⁸ Photons of the laser light are absorbed by the sample and then reemitted. The energy of the scattered photons after interaction with the sample is directly related to the energy levels of the material comprising the sample. In this way the chemical structure of a sample can be studied. In the literature on Raman spectroscopy a shift in the frequency of the reemitted photons (up or down) in comparison with original monochromatic frequency is called the Raman shift effect. Thus this shift provides information about vibrational, rotational and other low frequency transitions in molecules.

From a physical point of view the Raman effect is based on molecular deformations in electric field E determined by molecular polarizability α . The strength of the electric field (E) of the electromagnetic wave from the laser beam induces an electric dipole moment $P = \alpha E$ which deforms molecules upon interaction with the sample, thus the laser beam excites molecules and transforms them into oscillating dipoles. Because of these periodical deformation, molecules start vibrating with a characteristic frequency. The amplitude of vibration is called a nuclear displacement. A molecule with no Raman-active modes absorbs

a photon with a certain frequency, and then returns back to the same basic vibrational state emitting light with the same frequency as an excitation source. This type of interaction is called an elastic Rayleigh scattering. A Raman-active molecule absorbs a photon with frequency ν_f and part of the photon's energy is transferred to the Raman-active mode with frequency ν_m and the resulting frequency of scattered light is reduced to $\nu_f - \nu_m$. This Raman frequency is called Stokes frequency. A third type of photon scattering occurs when a photon with frequency ν_f is absorbed by a Raman-active molecule that is already in the excited vibrational state then the excessive energy of excited Raman active mode is released, molecule returns to the basic vibrational state and the resulting frequency of scattered light goes up to $\nu_f + \nu_m$. This Raman frequency is called Anti-Stokes frequency. It is known that spontaneous Raman scattering is very weak and instruments such as notch filters, tunable filters, laser stop apertures, double and triple spectrometric systems are used to reduce Rayleigh scattering and obtain high-quality Raman spectra.

Four major components typically resume a Raman system. These are the excitation source, sample illumination system and light collection optics, wavelength selector and detector. The sample is illuminated with a laser beam whose wavelength is selected from the characteristics of the sample then the scattered light is collected with a lens and filtered to obtain the Raman spectrum of a sample. As mentioned above, spontaneous Raman scattering is very weak and usually the main difficulty of Raman spectroscopy is separating the intense Rayleigh scattering from the Raman signal. To solve these problem, the spectral range close to the laser line where the stray light has the most prominent effect can be removed by means of interference (notch) filters which cut-off spectral range of $120 \pm 80 \text{ cm}^{-1}$ from the laser line. This method is efficient in stray light elimination but it does not allow detection of low-frequency Raman modes in the range below 100 cm^{-1} . Also stray light is generated in the spectrometer mainly upon light dispersion on gratings therefore Raman spectrometers typically use holographic gratings which normally have much less manufacturing defects in their structure and multiple dispersion stages are used as a way of stray light reduction. To detect Raman-active modes with frequencies as low as $3\text{-}5 \text{ cm}^{-1}$ double and triple spectrometers without use of notch filters have been developed.

Because the Raman signal intensity is normally weak researchers are nowadays working on improving Raman spectroscopy techniques that involve different ways of sample preparation, sample illumination or scattered light detection. Such as stimulated Raman in which the sample is irradiated with a very strong laser pulse allowing the observation of non-linear effects on the Raman signal. It has been reported that in comparison with continuous wave lasers (with electric field of about only $10^4 \text{ V}\cdot\text{cm}^{-1}$) pulsed lasers (electric field of about $10^9 \text{ V}\cdot\text{cm}^{-1}$) transform a much larger portion of incident light into useful Raman scattering improving the signal-to-noise ratio.

Coherent Anti-Stokes Raman (CARS) is another type of “non-linear” Raman spectroscopy. In these technique two very strong collinear lasers irradiate a sample. As an example to understand this technique we can think that the frequency of the first laser is constant, while the frequency of the second one is tuned so that the frequency difference between the two lasers equals exactly the frequency of some Raman-active mode of interest. Thus resulting in an extremely strong particular mode. CARS only one strong Raman peak of interest is obtained.

Some samples can absorb a certain laser beam energy and generate fluorescence which contaminates Raman spectrum especially when UV lasers are used. However, under certain conditions some of these fluorescent molecules can produce strong Raman scattering instead of fluorescence, this effect is known as Resonance Raman (RR). These effect takes place when the excitation laser frequency is chosen in a way that it crosses frequencies of electronic excited states and resonates with them. The chromophoric group, responsible for the molecule’s coloration, experiences the highest level of enhancement because the chromophoric group normally has the highest level of light absorption. Tunable lasers are the most appropriate choice for the RR technique, even when the frequency of the laser does not exactly match the desired electronic excited states an impressive enhancement of Raman signal occurs.

In SERS, the Raman signal from molecules adsorbed on certain metal surfaces can be 5-6 orders of magnitude stronger than the Raman signal from the same molecules in bulk volume. The exact reason for such dramatic improvement is still under discussion but the latest explanations point to the fact that since the intensity of Raman signal is proportional to

the square of electric dipole moment $P = \alpha E$, there are two possible reasons - the enhancement of polarizability α , and the enhancement of electrical field E . The enhancement of polarizability may occur because of a charge-transfer effect or chemical bond formation between metal surface and molecules under observation, known as chemical enhancement. On the other hand, the interaction of the laser beam with irregularities on the metal surface such as metallic particles excite conduction electrons at the metal surface leading to a surface plasma resonance and strong enhancement of electric field E , known as electromagnetic enhancement. The most common substrates used for SERS are electrochemically etched silver electrodes as well as silver and gold colloids with average particle size below 20 nm. The signal enhancement can be so dramatic that weak Raman bands can clearly appear in the SERS spectrum, also, trace contaminants of the sample could be expressed. But it also occurs that, because of chemical interactions with the metal surface, peaks which are strong in conventional Raman might not be present in SERS. These non-linear character of signal intensity as a function of concentration may complicate things therefore, a careful consideration of all physical and chemical factors should be done while interpreting SERS spectra. Qualitative analysis of biochemical and structural changes and interaction of solids with tissues at nanoscale plays a central role of modern medicine. Some of these changes are highly related to the development of disease processes, and may provide important clues for specific and efficient diagnosis.⁴⁹

Raman spectroscopy can be used to identify the vibrational energy levels of the molecules present in a sample, which are unique for individual molecules and associated with the vibrations of specific chemical bonds of the interaction between solids and bio-specimens.^{50,51} In 2006, Kneipp et al. published a detailed study on the SERS effect produced by aggregates of gold and silver nanoparticles. In this study they show that the enhancement is greater when nanoaggregates composed of gold or silver nanoparticles are in the vicinity of the biomolecules in comparison with the use of isolated nanoparticles. In particular they propose the use of these aggregates as an excellent choice to study biological systems, such as cells, using Raman spectroscopy. This work is based on the method proposed by Kneipp, wherein the formation of nano-clusters is promoted for molecular detection in cellular systems.⁵²

In this work SERS is used as a tool for detecting the molecular structural changes due to an interaction of the QDs with the cells. The spectroscopic observation of the interaction of nanoparticles, such as QDs, with cells using gold nano-aggregates has been proposed by Kneipp et al. and is of particular interest for bioaccumulation studies and drug delivery.⁵²

The accumulation and uptake process of TGA@CdTe QDs on fresh human cells is largely unknown and the early bioaccumulation of TGA@CdTe QDs on living microalgae cells is a topic open for discussion.^{5, 21, 27} With the aim of contributing on this topic SERS is used as a tool for detecting possible molecular structural changes due to an interaction of the QDs with the cells. Therefore, the early interaction of OECs and HPM with TGA@CdTe QDs using SERS as a tool for detecting possible molecular structural changes is the central theme of this study. SERS is obtained through anisotropic gold nanoparticles (AuNPs), which did not alter the previously reported characteristic Raman signal of the OEC or HPM. Spectral differences between OEC-AuNPs and OEC-AuNPs-BSA-QDs have been successfully obtained and suggest that the internalization of QDs may occur mainly by facilitated diffusion. For the case of HPM, SHPM are used as control sample since they do not present an ECM. This successful detection of changes in the Raman spectra has not been reported before and may lead to a deeper understanding of the response mechanisms of human cells in the presence of QDs. Also spectral differences between HPM/AuNPs and HPM-QDs/AuNPs are found.

At nano-scale, there are several techniques of characterization that can provide diagnosis for cancerous specimens such as targeted molecular imaging, ultrasound imaging by magnetic nanoparticles and nanoparticle-enhanced magnetic resonance⁵³⁻⁵⁵ and some can be tested in real time;⁵⁶ however, these techniques alone cannot provide a diagnosis due to the poor spatial resolution and molecular level analysis. In this way, high spatial resolution microscopy techniques such as confocal microscopy, electron microscopy and its analytical techniques can resolve at nanometric scale the interaction and structure of bio-specimens.^{57,}

58

Moreover recent uses of Raman spectroscopy in biological measurements and applications are particularly oriented to clinical examinations related to the detection of

malignancies and cancer in tissues.⁵⁹ Raman spectroscopy also provides substantial information about the sample identity; however, for biological samples it is necessary to reduce the power of the laser sources, which results in a reduction of the signal used to extract information from the samples.⁶⁰ As previously mentioned SERS is a powerful, ultrasensitive, and non-destructive spectroscopic technique that can detect analytes down to the single molecule level while simultaneously providing molecular specific information.^{61, 62} SERS is a technique resulting in strongly increased Raman signals of molecules at or near metal nanostructures, typically noble metals such as gold and silver. Effective SERS depends on the increase in the Raman cross section as a result of the excitation of surface plasmons, which are collective oscillations of the conduction electrons against the background of metal surfaces. When the exciting light is resonant with the dipolar plasmon of a metallic nanoparticle this will radiate light characteristic of dipolar radiation, and given the relationship between this radiation and the incident light, certain spots near to the region of metallic nanoparticles show enhancement.⁶³ The SERS effect produced by metallic nanoparticles enhances the inelastic scattering signal allowing single-molecule detection. In particular, this vibrational spectroscopic technique has been extensively used for characterization of biological samples.⁶⁴ In 1997 it was published that regions of very high electromagnetic enhancement are necessary to observe the Raman scattering of single molecules. Nanoparticle aggregates contain at least one nanoparticle junction, by means of scanning probe microscopy it was observed that in the junction or close interaction ($\sim 2\text{nm}$) of plasmonic objects which radius of curvature is within the nm scale, a concentration of the electromagnetic field occurs and as a result, an amplification in the near field between and around is obtained.⁶⁵ The locations where such amplification occurs are called hot spots. In addition, the use of silica particles either decorated or covered with gold for SERS effect in biological applications has been widely reported and discussed due to the large adsorption properties with biomolecules. This adsorption facilitates the conjugation and localization of the metallic nanoparticles at suitable distances from target biomolecules, generating the optimal conditions for SERS effects.^{61, 62, 66, 67} One of the many biomedical applications of SERS is on tissue characterization, diagnosis of malignancies, particularly for cancer detection. Mortality rates of breast cancer have increased in the last 40 years in most Latin America in part by deficient diagnosis.⁶⁸ Development of appropriate diagnostic tools is a

relevant problem.⁶⁹ Even in developed countries like United States, the mortality of breast cancer achieves 40,000 women per year.⁶⁰ Minimally invasive optical imaging and spectroscopic techniques have the potential to improve early diagnosis of breast cancer, specifically through a large number of Raman active molecules present in biopsies of breast tissue.⁶⁰ The SERS technique has also shown promise for hard dental tissue characterization. This because of the simple sample preparation and the linear response to mineral concentrations.⁷⁰ The formation of dental tissue involves complex molecular and cellular events and its Raman spectrum is characterized by large proportions of organic materials compared to other hard tissues.⁷¹ It has been previously reported that the study of the evolution of lesions in dental tissue can help us to understand better the process of decay and more adequately assess when tooth extraction is required.⁷² Thus in the future Raman spectroscopy could reduce the use of ionizing radiation commonly used in teeth diagnosis.

A study of the SERS effects on normal glandular breast tissue and breast adenocarcinoma and carious dental tissue upon interaction with Au/SiO₂ powder compared with the SERS signals obtained by incubating the tissues with naked colloidal gold nanoparticles (AuNPs) has been carried out. The optical effects observed upon interaction of the tissues with powdered Au/SiO₂ shows potential of these material to serve as a tool for rapid soft and hard tissue diagnosis complementary to other established techniques.

Chapter two

Synthesis, optical, structural and morphological characterization of TGA@CdTe QDs, naked gold nanoparticles and Au/SiO₂ powder

In this chapter a wet chemical synthesis for thiol capped CdTe QDs and the synthesis of naked gold colloidal nanoparticles following the Martin method and Au/SiO₂ powder are presented. The optical characterization of these materials is based on the UV-Vis and photoluminescence spectra while structural and morphological characterization methods are: x-ray diffraction, Fourier transform infrared spectroscopy, SEM, TEM, and HRTEM respectively.

Both TGA@CdTe QDs and naked gold nanoparticles (AuNPs) have been prepared in water since the objective is to use them in bio-applications. While in case of silica powder with adsorbed gold nanoparticles the goal is that the powder has hydrophilic properties allowing its compatibility to the tissues.

2.1 Thioglycolic acid capped CdTe QDs

2.1.1. Materials

All chemicals used in this work are analytical grade or highest purity. Cadmium perchlorate hydrate (Cd (ClO₄)₂·6H₂O), thioglycolic acid (TGA) and sodium hydroxide have been purchased from Sigma-Aldrich. Aluminum telluride (Al₂Te₃), was purchased from Advanced Chemicals. Sulfuric acid and acetone were purchased from Karal. Deionized water was purchased from Quimicurt.

2.1.2. Synthesis of TGA-capped CdTe quantum dots

The synthesis of TGA-capped CdTe quantum dots (TGA@CdTe QDs) was carried out by following a protocol reported in the literature.⁷³ The experimental setup for the synthesis is shown in figure 2. Briefly, 2.35 mmol of Cd (ClO₄)₂·6H₂O and 5.7 mmol of the binder stabilizer (TGA) are added to 125 mL of distilled water. The solution

was stirred during 5 minutes. The pH is adjusted (pH=11.2-11.8) by adding 1.0 M solution of NaOH. During this step the solution may remain turbid due to the incomplete solubility of cadmium. The solution is refluxed at 100 °C during 20 minutes under N₂ atmosphere. The H₂Te gas generated, by the reaction of 0.2 g (0.416 mmol) of Al₂Te₃ and 20 mL of 0.5 M H₂SO₄ under stirring and N₂ atmosphere, is passed through the solution together with a slow nitrogen flow for ~20 min to the Cd-TGA solution flask to afford the formation of the TGA@CdTe QDs. The reaction time for the growth of QDs is different depending on the nanocrystal size to be obtained, the reflux time is varied from 30 minutes to 6 days.

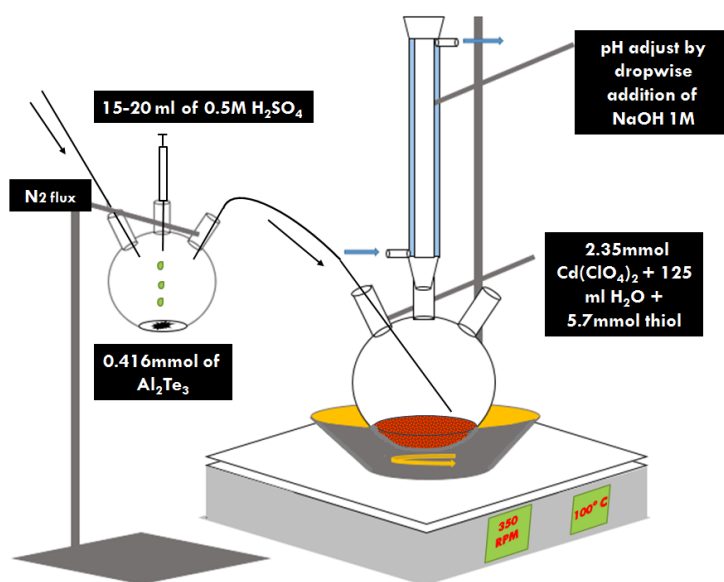


Figure 2. Experimental setup for the synthesis of TGA@CdTe QDs.

2.1.3. Optical and morphological characterization

The UV-Vis absorption spectra of colloidal TGA@CdTe QDs have been measured in transmittance using an Agilent Technologies Cary Series UV-Vis-NIR spectrophotometer (Cary 5000). Photoluminescence (PL) characterization of the TGA@CdTe QD, cell and cell-QD is performed using a 75 W Xenon lamp. All measurements have been taken under identical conditions. The fluorescence emission is analyzed with an Acton Research modular 2300 spectrofluorometer and a R955 Hamamatsu photomultiplier tube for visible emission under excitation of 350-500 nm.

The system is PC controlled through the Spectra-Sense software. All measurements have been performed at room temperature (24°C).

Figure 3 (a) shows the PL and (b) the UV-Vis spectrum of some of the as-prepared colloidal TGA@CdTe QDs. Samples have been obtained with the maximum emission peak centered in the range of 520-600 nm and 550-620 nm for the absorption. The photoluminescence is obtained by exciting the QDs at 390 nm. The emission spectra showed a wide band, as an indication that the sample contained a certain range of QD sizes.⁷⁴

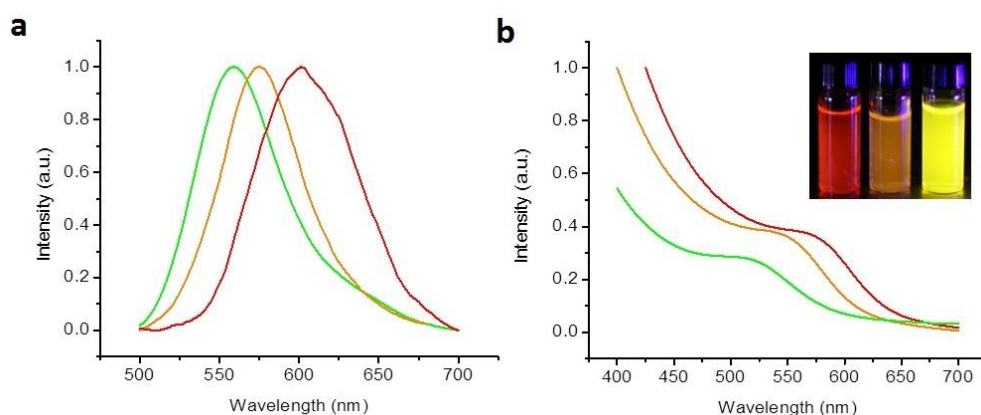


Figure 3. Emission and absorption spectra of the as-prepared TGA-CdTe QDs samples.

Electron microscopy imaging is obtained using a JEOL ARM 200F microscope operated at 200 kV in STEM (BF/HAADF) mode. Ultra-high resolution Scanning Electron Microscopy (SEM) images have been obtained using a Field-emission gun (FEG) HITACHI S-5500 microscope coupled with Dual BF/ADF detector and energy dispersive X-ray spectroscopy (EDS) to perform chemical elemental analysis.

The samples that were used to study the interaction with cells correspond to an emission centered at 560 nm. In figure 4 high resolution TEM (HRTEM) images of the TGA@CdTe QD are shown. The average sizes measured from the TEM images are ~2.5 nm and ~3 nm, where the maximum of the emission spectrum is centered at 560 nm (figure 3 (a)) and 575 nm (figure 3 (b)) respectively. The interplanar spacing is about 0.23 nm, which corresponded to the (220) plane of the cubic CdTe.⁷⁵ To

confirm the average size of the TGA@CdTe QDs, the empirical fitting function, deduced by Yu et al.⁷⁶ is used:

$$D = (9.8127 \times 10^{-7}) \lambda^3 - (1.7147 \times 10^{-3}) \lambda^2 + (1.0064) \lambda - 194.84$$

Where D (nm) is the diameter of the QD, and λ (nm) is the wavelength of the first excitonic absorption peak. The calculated size of the TGA@CdTe QDs samples are ~2.8 nm and ~3.3 nm for samples (a) and (b), which corresponded to the average size observed by HRTEM images. The concentration of QDs is around $0.60 \times 10^{-5} \text{ mol L}^{-1}$, which is determined based on previous reports.⁷⁶ The concentration in the quantities used is suitable for cell-nanoparticle interactions and toxicity analysis purposes.⁷⁷ Zeta potential of QDs has been measured, resulting in a negative value of -27.3 mV as an indication of the presence of the TGA group. As it has been shown in previous reports, the thiol capping by thioglycolic acid of water-dispersible CdTe QDs consists of a chemical bond between the hydrophobic sulfhydryl group and the QD surface. Meanwhile, the hydrophilic carboxylic acid group is free for molecular interactions and to enhance the colloidal stability of the TGA@CdTe CDs in aqueous media. The carboxylic acid groups are mainly deprotonated in aqueous solution affording carboxylate moieties, which change the surface charge of the TGA@CdTe QDs to negative values (-27.3 mV). As a result, the QDs nanoparticles are stable due to high electrostatic repulsion between them.^{73, 78, 79}

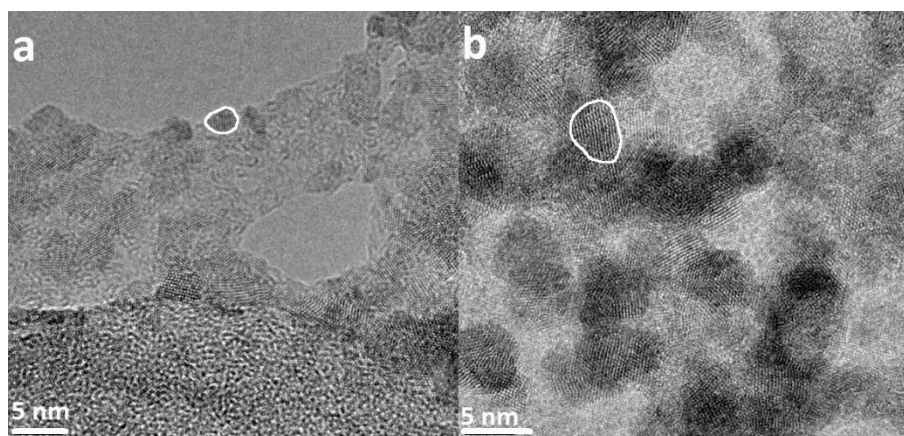


Figure 4. HRTEM of TGA@CdTe QDs. With an overall diameter of (a) 2.8 nm and (b) 3.3 nm calculated by the empirical function reported by Yu et al.⁷⁶

2.2. Anisotropic naked gold nanoparticles

2.2.1. Materials

All chemicals used in this work are analytical grade or highest purity. Gold (III) chloride hydrate and sodium citrate have been purchased from Sigma-Aldrich. Sodium borohydride and deionized water have been purchased from Fluka and Quimicurt respectively.

2.2.2. Synthesis gold nanoparticles

The preparation of gold nanoparticles is based on the method reported by Martin et al.⁸⁰ Firstly, 1.0 mL of 1.0 M HAuCl_4 solution are added to 90 mL of distilled water under stirring; after 1 minute, 1 mL of a previously cooled (5 °C) 0.1 M NaBH_4 solution are added. The newly formed gold nanoparticles are left unturned at room temperature for 48 hours allowing the formation of anisotropic nanoparticles.⁸¹

2.2.3. Optical and morphological characterization

The optical and morphological characterization is carried out with the methods and the equipment described in the previous section.

Figure 5 shows the UV-Vis spectrum of AuNPs dispersed in aqueous solution. The localized surface plasmon resonance (LSPR) is centered at 530 nm.

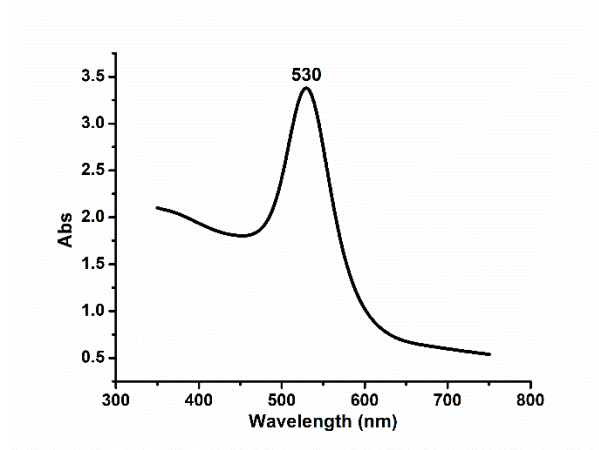


Figure 5. UV-Vis spectrum of AuNPs dispersed in aqueous solution.

Figure 6 (a) shows TEM image of the mixture of anisotropic and spherical gold nanoparticles (AuNPs) with an average diameter size of ~20 nm, see figure 6 (b).

Using the methodology reported by Liu et al.,⁸² the gold nanoparticles molar concentration is estimated to be $\sim 5.4 \times 10^{-10}$ mol L⁻¹.

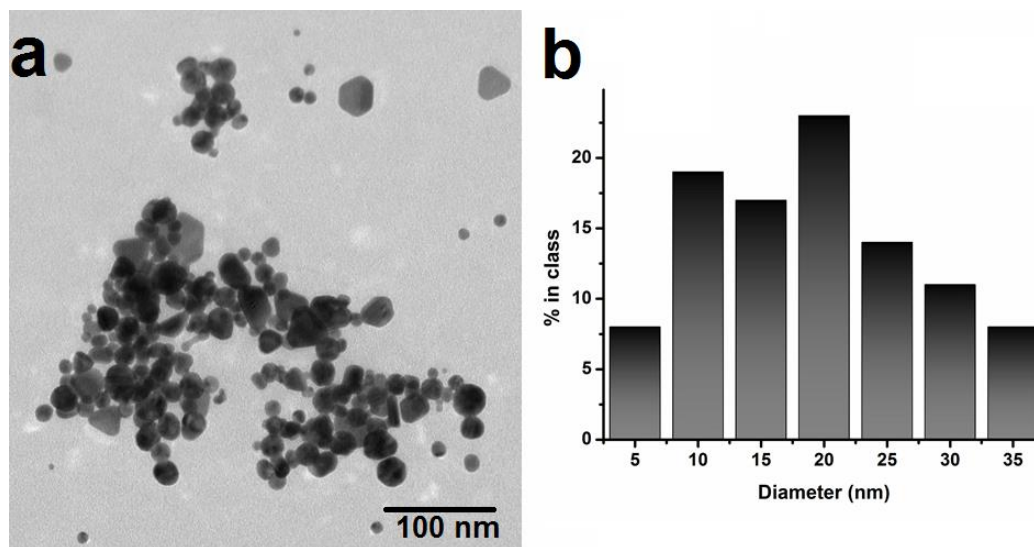


Figure 6. TEM image of the gold nanoparticles (AuNPs) and particle size distribution of the gold nanoparticles.

TEM imaging of AuNPs reveals their anisotropic structure (Fig. 5).⁸³ These structures are the result of the NaBH₄ gold reduction, the absence of a dispersant and the 48 hours of incubation time.^{84, 85} These factors are known to promote anisotropic structures resulting from a tendency to aggregate due to the absence of an electrostatic repulsion between the nanoparticles.⁸⁶⁻⁸⁸ Nevertheless, in this study, the AuNPs possessed a slightly negative charge (~ -10 mV, determined by zeta potential), probably due to the adsorption of negative Cl⁻ ions on the surface of the AuNPs.⁸⁹

2.3. Optical characterization of the interaction between TGA@CdTe QDs and naked AuNPs

The interaction between TGA@CdTe QDs and naked AuNPs dispersed in water is analyzed using UV-Vis absorption and photoluminescence (PL) spectra. The results are summarized in figure 7 for the case of a TGA@CdTe QDs sample (a) with an absorption peak centered at 520 nm and the emission peak located at 560 nm under excitation at 400 nm. The emission spectra shows a wide band of 63 nm, meaning that the sample contains a distribution of

nanocrystal sizes.⁷⁴ Figure 7 (b) shows the UV-Vis spectrum of AuNPs dispersed in aqueous solution. The localized surface plasmon resonance (LSPR) is centered at 530 nm. The wide band in the absorption is consistent with some agglomeration of the particles, due to the lack of surfactant.⁸¹ The UV-Vis spectrum of AuNPs mixed with TGA@CdTe QDs is also presented to show that the absorption of AuNPs remains unchanged. The PL of QDs is monitored in a mixture of QDs with different concentrations of AuNPs and no changes on the emission wavelength of the QDs due to the presence of AuNPs are found, see figure 7 (c). The changes in emission intensity of the QDs in the presence of AuNPs, which SRP is close to the emission of the QD have been widely reported as a consequence of energy transfer from the QD to the AuNP.⁹⁰

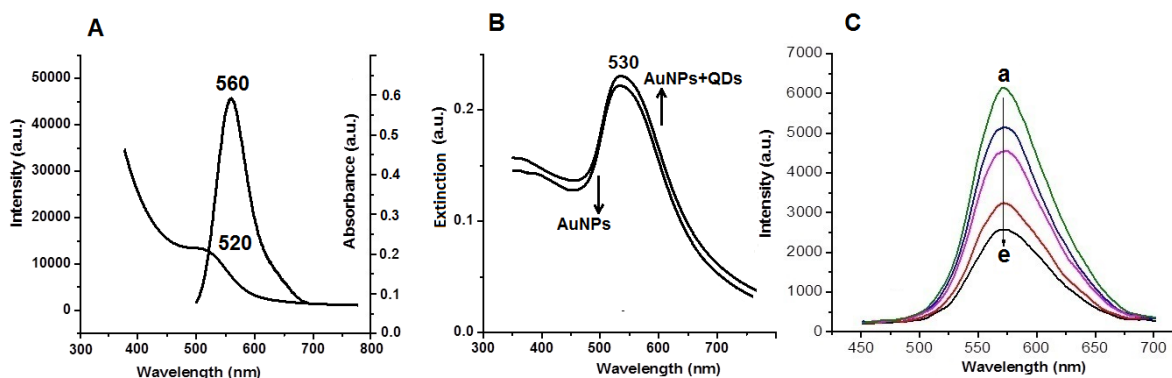


Figure 7. (a) Photoluminescence (PL) and absorption spectra of TGA@CdTe QD. (b) Absorption spectra of AuNPs and AuNPs+ TGA@CdTe QDs. (c) PL spectra of TGA@CdTe QD ($0.56 \times 10^{-5} \text{ mol L}^{-1}$) in the presence of AuNPs at various concentrations (a-e: $0, 0.25, 0.5, 0.75$ and $1.2 \times 10^{-10} \text{ mol L}^{-1}$).

Since the well-dispersed AuNPs possess slightly negative charge ($\sim 10 \text{ mV}$) probably due to the adsorption of ions on the surface of the AuNPs⁸⁹, and the zeta potential of TGA@CdTe QDs is measured to be -27.3 mV due to the ionization of the $-\text{COOH}$ group⁹¹, there is no electrostatic attraction between the negatively charged AuNPs and QDs. Moreover the absorption spectrum of AuNPs remained unchanged in the presence of TGA@CdTe QDs therefore the observed fluorescence decrease of TGA@CdTe QDs in the presence of AuNPs should be attributed to the inner filter effect in which gold nanoparticles absorb photons coming from the excited states of the QDs and a chemical interaction does not occur between the two nanoparticles.⁹²

2.4. Gold nanoparticles embedded in SiO₂ (Au/SiO₂)

2.4.1. Materials

Tetrachloroauric acid (HAuCl₄), cetyltrimethylammonium bromide (CTAB), ammonium hydroxide (NH₄OH), and tetraethyl orthosilicate (TEOS) are used reagent grade and highest purity from Sigma-Aldrich. Absolut ethanol was purchased from Jalmek.

2.4.2. Synthesis of Au/SiO₂ powders

The Au/SiO₂ powder is a mixture of AuNPs embedded into SiO₂ rod-shaped structures (Au/SiO₂ clouds) and SiO₂ spheres. AuNPs embedded into SiO₂ clouds were synthesized following the Turkevich method. Gold reduction occurs by addition of a 1% citrate solution to a boiling solution of 1.0 mmol HAuCl₄ under vigorous stirring. After the reduction, a red wine color, characteristic of AuNPs, was obtained.⁹³ Separately, 0.48 g of CTAB were dissolved in 15 mL of ethanol and 6 mL of NH₄OH. To this solution, the as-prepared AuNPs seeds (0.25 mL) were then added, under vigorous stirring, to 10 mL of 0.5 mmol HAuCl₄ followed by 25 mL of H₂O. Finally, this solution was mixed with the previously prepared solution containing CTAB. The mixture was stirred for 15 minutes and then TEOS was dropwise added inducing the formation of Au/SiO₂ clouds and SiO₂ nanoparticles according to the well-known Stöber method by hydrolysis and condensation of TEOS in the presence of a surfactant.⁹⁴ At first, to obtain the Au/SiO₂ rod-shaped clouds, the molar ratio of the reaction mixture was within the range of 200-400 (CTAB): 1000 (H₂O): 20 (NH₄OH): 1.4 - 2.8 (TEOS).⁹⁵ The colloidal solution was heated at 100 °C for 24 hours. For the elimination of excess CTAB, the nanoparticles were calcined at 500 °C, thereby obtaining a mixture of semitransparent and flocculent SiO₂ matrix embedded with gold nanoparticles (Au/SiO₂ clouds) and SiO₂ nanoparticles. Thus, the Au/SiO₂ product was obtained with a concentration of approximately fifteen SiO₂ nanoparticles per Au/SiO₂ cloud structure. Each Au/SiO₂ cloud contained an average of ~750 AuNPs.

2.4.3. Optical characterization of Au/SiO₂ powder

The optical and morphological characterization is carried out by the methods and equipment previously described.

Figure 8 shows the UV-Vis spectrum of (a) Au/SiO₂ powder, (b) colloidal gold synthesized by the Turkevich method, which was used to prepare Au/SiO₂, (c) AuNPs synthesized by the Martin method and (d) SiO₂ nanoparticles. For Au/SiO₂ and the colloidal gold nanoparticle seeds the SRP is centered at 514 nm. For the colloidal AuNPs the SRP is centered at 524 nm, and the wide band is indicative of some degree of aggregation of the colloidal nanoparticles due to the lack of surfactant.⁸¹ The absorption spectra of the Au/SiO₂ samples showed wider bands, which is consistent with the existence of various particle sizes, some degree of agglomeration of the particles, but mainly due to the interplay between with the silica environments.⁶² Also the concentration of AuNPs in colloidal solution is estimated from the extinction coefficient of gold, resulting to be $\sim 6.9 \times 10^{10}$ particles/ml; in good accordance with previous reports.^{96, 97}

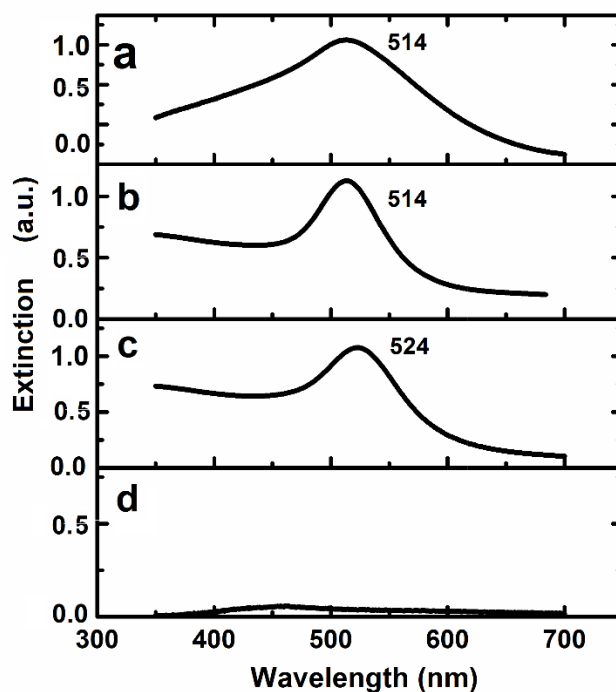


Figure 8. UV-Vis absorption spectra of (a) Au/SiO₂, (b) colloidal gold synthesized by the Turkevich method, used to prepare Au/SiO₂, (c) AuNPs synthesized by the Martin method and (d) SiO₂ nanoparticles.

2.4.4. Size, morphological characterization and elemental analysis

The size and morphology of the colloidal gold and the as prepared Au/SiO₂ powder are shown in figures 9 and 10. SiO₂ nanoparticles have been obtained with an overall diameter of 400 nm, highly homogeneous and with a narrow size distribution (figure 10 (a)). The gold nanoparticles found embedded on the SiO₂ structures had a size distribution of 5-20 nm (figure 10 (b)) and evenly distributed over all the silicon oxide structural matrix. The size of the colloidal gold nanoparticles (AuNPs) is in the range of 5-40 nm, see Fig. 6 (b).

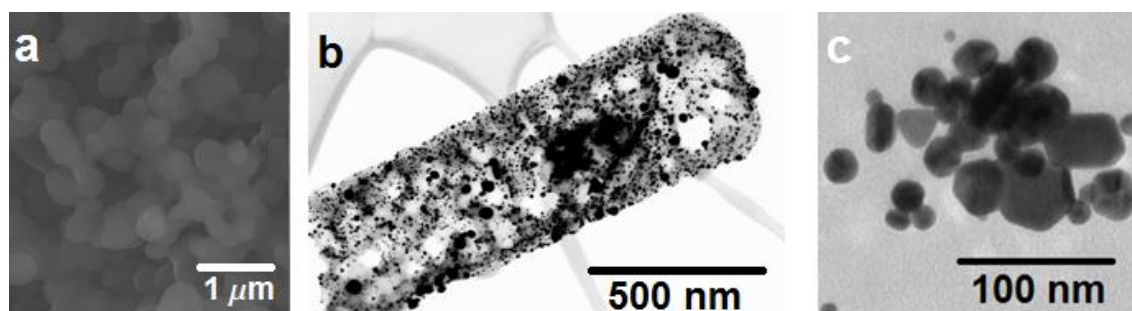


Figure 9. Electron microscopy micrographs. (a) SEM image of SiO₂ nanoparticles with an average size of 500 nm and (b) BF-STEM imaging of gold nanoparticles, with average diameter of 20 nm into Au/SiO₂ cloud. (c) BF-STEM imaging of AuNPs.

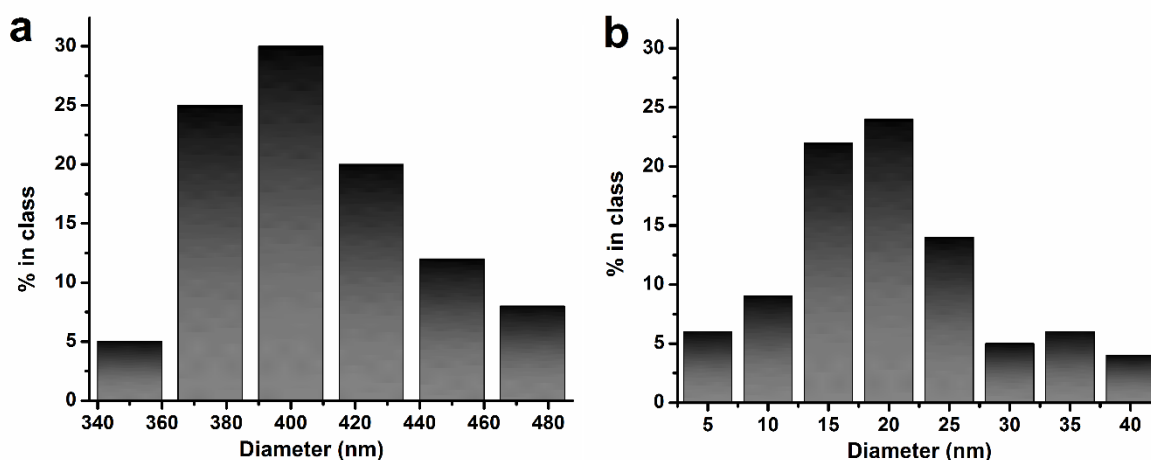


Figure 10. Particle size distribution of (a) SiO₂ and (b) gold nanoparticles embedded in the SiO₂ clouds.

For the Au/SiO₂ structures, the presence and location of gold nanoparticles embedded into SiO₂ is confirmed by the elemental mapping through EDS microanalysis. The embedded gold nanoparticles obtained with diameter of 20 nm are effectively visualized to be evenly distributed throughout the SiO₂ structures, giving a hybrid nanostructure with of 0.5 to 1.5 μm for width and length respectively, see figure 11.

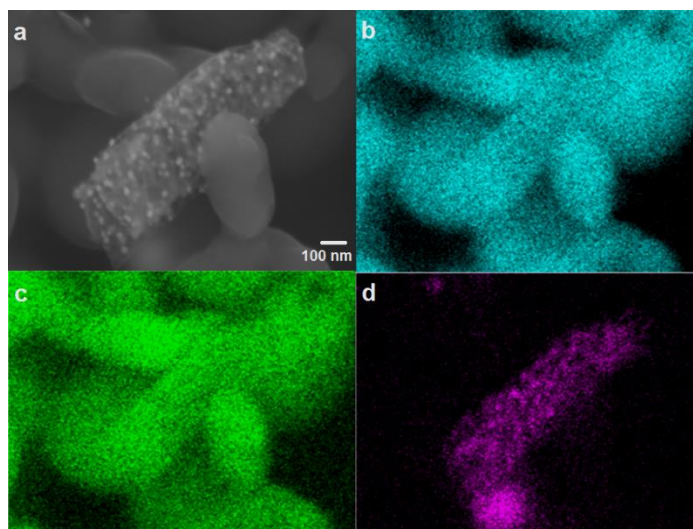


Figure 11. (a) SEM image of an Au/SiO₂ cloud surrounded by SiO₂ NPs and its elemental EDS mapping: (b) oxygen, (c) silicon and (d) gold.

All samples have been dispersed in distilled water and show a negative zeta potential, -22.4 mV and -26 mV for Au/SiO₂ and SiO₂ samples respectively. The zeta potential of colloidal AuNPs is measured to be -44 mV. Powder samples containing Au/SiO₂ structures showed the characteristic color of gold seeds, as is shown in figure 12. In the image, gold nanoparticle seeds are represented by the red solution and the Au/SiO₂ powder is reddish, as seen in figure 12 (a) and (b), respectively. The SiO₂ powder is white (see figure 12 (c)). The LSRP of spherical gold nanoparticles situated in 514 nm, is consistent with the overall size of ~20 nm and the red color of gold nanoparticles as prepared by following the Turkevich method.⁹⁸



Figure 12. Color of (a) colloidal gold nanoparticles (red solution), used as a seed for the synthesis of (b) Au/SiO₂ (red powder) and (c) SiO₂ nanoparticles in powder.

The X-ray diffraction (XRD) patterns of the Au/SiO₂ and SiO₂ powders have been obtained using a Bruker D2 Phaser with a Bragg-Brentano array. by XRD. The patterns of the as-prepared Au/SiO₂ and SiO₂ samples are presented in Figure 11. Peaks at $2\theta = 38.3^\circ$, 44.5° , 64.8° , and 77.7° are assigned to (111), (200), (220), and (311) reflection lines, respectively. Indicating the formation of a face-centered cubic phase of metallic gold (figure 13 (a) and (b)).⁹⁹, which correlated with the electron microscopy of the nanoparticles (figure 9 (a) and (b)). No impurities have been observed and the absence of any diffraction peaks for SiO₂ nanoparticles indicates its amorphous nature, since crystallization temperature of amorphous silica to crystalline phase occurs only at temperatures around 1300 °C (figure 13 (c)).¹⁰⁰

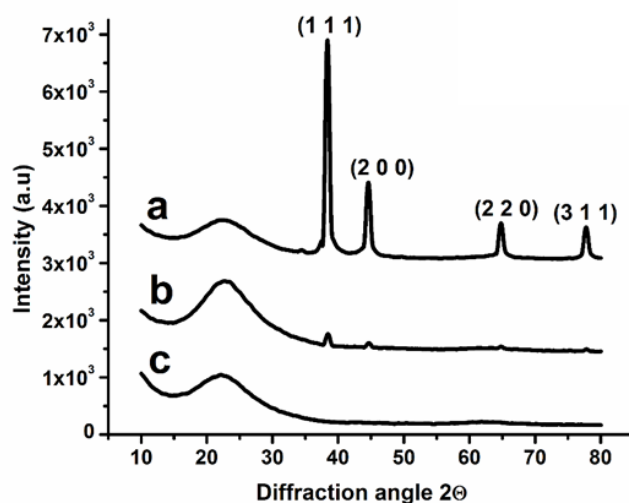


Figure 13. Representative XRD patterns of (a) Au/SiO₂ structures mixed with SiO₂ in proportion of 1:15, (b) Au/SiO₂ structures mixed with SiO₂ in proportion of 1:40 and (c) SiO₂. The patterns (a) and (b) can be indexed as a gold (FCC) structure.

The Fourier transform infrared (FTIR) spectra have been obtained using a Perkin-Elmer spectrophotometer with a deuterated triglycine sulfate detector and a spectral resolution of 4 cm⁻¹. The Au/SiO₂ and SiO₂ samples showed the characteristic stretching vibrations in IR for silica materials, as shown in figure 14. The broad absorption band 3600-3100 cm⁻¹ is assigned to the $\nu(\text{OH})^*$ stretching vibration of surface hydroxyl groups involved in hydrogen bonding with water molecules and/or adjacent silanols. The band at 1640-1630 cm⁻¹ corresponds to the $\delta(\text{OH})^*$ bending vibration of adsorbed water molecules and/or silanols. The broad absorption bands in the 1100-650 cm⁻¹ region corresponded to Si-O-Si, $\nu(\text{Si-O})$ in Si-OH surface groups, $\delta(\text{OH})$ of the Si-O-H angle, and $\delta(\text{O-Si-OH})$ of the O-Si-OH

angle.⁹⁹ While for AuNPs the $\nu(\text{OH})$ stretching vibration (3500-3000 cm^{-1}) of surface hydroxyl groups involved in hydrogen bonding with water molecules is found.

*Symbols: δ bending, ν stretching

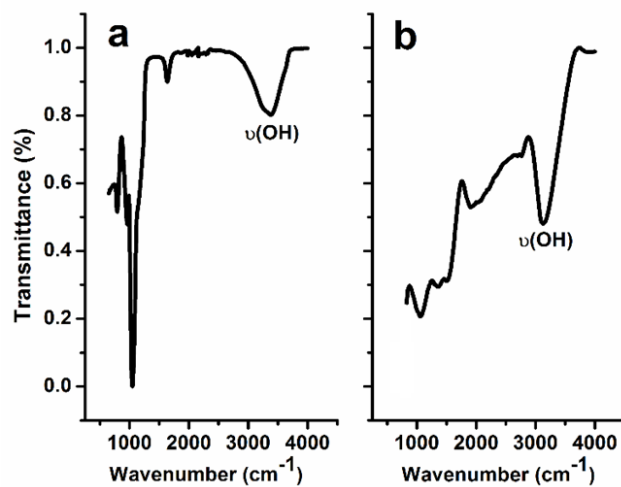


Figure 14. Normalized FTIR spectra of: a) Au/SiO₂ powder and b) AuNPs in colloidal solution.

Summary

Water soluble TGA@CdTe QDs have been obtained by a wet chemical synthesis. The reaction condition facilitates the formation of mixed CdTe(S) nanocrystals and TGA-capped CdTe QDs. It has been reported that core-shell nanocrystals (TGA-CdS-CdTe) may form during the synthesis process. The presence of a core-shell structure might be a reason for the wide band in the PL spectra, a more detailed characterization of this could be accomplished in the future. The effective capping of the material explains the high photo-stability of these nanocrystals, because it has been reported that the main photo-degradation mechanism is the photo-oxidation of surface tellurium atoms.

TEM imaging of AuNPs revealed their anisotropic structure.⁸³ These structures are the result of the NaBH₄ gold reduction, the absence of a dispersant and the 48 hours of incubation time.^{84, 85} These factors are known to promote anisotropic structures resulting from a tendency to aggregate due to the absence of an electrostatic repulsion between the nanoparticles.⁸⁶⁻⁸⁸ Nevertheless, in this study, the AuNPs possessed a slightly negative charge (~ -10 mV, determined by zeta potential), probably due to the adsorption of negative Cl⁻ ions on the surface of the AuNPs.⁸⁹

The interaction between TGA@CdTe QDs and AuNPs is analyzed and resulted in an inner filter effect where no evidence of a chemical bond is observed between the two nanoparticles.

A facile method for the synthesis of Au/SiO₂ powder is presented with the aid of the cationic surfactant CTAB. The formation of the Au/SiO₂ powder can be rationalized based on the surfactant-templated sol-gel method. When the silica precursor, TEOS, was injected into the gold seeds solution, it hydrolyzed and condensed into silicate polyanions. These negatively charged polyanions interacted via electrostatic interactions with the positively charged groups of the surfactant CTAB, which was surrounding the AuNPs. This process promoted the growth of the silica structure around the AuNPs, while inhibiting the TEOS homogeneous nucleation process.^{101, 102} While TEOS was being added dropwise, depending on the availability of AuNPs and the changes in the molar ratio of CTAB/H₂O/NH₄OH/TEOS, rod-shaped Au/SiO₂ clouds were first formed and later the SiO₂ spherical nanoparticles.⁹⁵ The number of AuNPs per unit volume in the Au/SiO₂ clouds is limited by inter-particle Coulombic repulsion, as in the case of the attachment of gold colloids on planar silica surfaces.¹⁰¹

Chapter three

Interaction of TGA@CdTe quantum dots with plant and human cells

In this chapter, the results obtained from the study of interaction between plant and human cells with thioglycolic acid (TGA) capped CdTe quantum dots (TGA@CdTe QDs) are presented and discussed.

Changes in the Raman spectrum of *Haematococcus pluvialis* (Chlorophyceae) microalgae (HPM) induced by the adsorption of TGA@CdTe QDs on its extracellular matrix (ECM) have been found. Non-functionalized gold anisotropic structures (AuNPs) have been successfully used as nano-sensors for surface-enhanced Raman spectroscopy in these microalgae cells. Raman spectroscopy results show that TGA@CdTe QDs interact with the ECM and this interaction is likely mediated by saccharides. Also the possible effects of reactive oxygen species (ROS) are mainly expressed in relation to chloroplasts. TGA@CdTe QDs are absorbed and localized within the ECM after an incubation period of five minutes.

The internalization mechanism of TGA@CdTe QDs using non cultivated oral epithelial cells obtained from healthy donors is studied. AuNPs have been also used as nanosensors for surface-enhanced Raman spectroscopy to efficiently identify characteristic Raman peaks, providing new evidence indicating that the first interactions of these QDs with epithelial cells occurred preferentially with aromatic rings and amine groups of amino acid residues and glycans from trans-membrane proteins and cytoskeleton. Using an integrative combination of advanced imaging techniques, including confocal microscopy, ultra-high resolution SEM, high resolution STEM coupled with EDX spectroscopy together with the results obtained by Raman spectroscopy, it is determined that thioglycolic acid capped CdTe QDs are efficiently internalized into freshly extracted oral epithelial cells only by facilitated diffusion, distributed into cytoplasm and even within the cell nucleus in three minutes.

3.1. Biological sample preparation and measurement standards

3.1.1. *Haematococcus pluvialis* microalgae cells

HPM have been obtained from the Culture Collection of Algae at The University of Texas at Austin (UTEX). HPM have been cultured at room temperature in Erlenmeyer flasks and kept in orbital shakers under illumination with white fluorescent lights ($125 \mu\text{mol photons m}^{-2}\text{s}^{-1}$) and a 12:12 light-dark photoperiod. The culture media consisted of standard Wright's Cryptophyte (WC). In order to induce stress in the HPM, a nitrogen-limited culture is prepared; this together with four days of continuous illumination lead to the development of red cysts.¹⁰³ The nitrogen-limited culture had five times less nitrogen than the standard WC media. Algae concentrations in cell culture were 145500 and 125000 cells/mL for HPM and SHPM respectively.

Sample preparation has been conducted at room temperature (24 °C). The algae have been rinsed with deionized water in order to remove traces of culture media. A volume of 200 μl of cells suspended in WC have been dispersed in 1 ml of deionized water, stirred for a few seconds and centrifuged at 3600 rpm for 3 minutes. The supernatant is decanted and the cells have been suspended in 1 ml of deionized water. At this point the sample is divided into 2 Eppendorf tubes, each one containing 500 μl of algae dispersed in deionized water; additional 500 μl of deionized water were added to each tube. A sample of algae suspended in deionized water is used as control sample. The cell-QDs sample is obtained by the addition of 100 μl of QDs to cells, followed by a 5-minute incubation period; the excess of TGA@CdTe QDs is removed by centrifugation. The samples are suspended in 0.5 ml of deionized water and 50 μl of the suspension are taken and placed on microscope slides for confocal microscopy.

For Raman spectroscopy measurements, 200 μl of AuNPs are added. After an incubation time of 30 minutes the samples have been centrifuged and 50 μl are taken and placed on a silicon wafer.^{104, 105} For EDS measurements 25 μl of the algae suspension are taken and placed on a silicon wafer in a preheated oven at 100°C for three minutes and then cooled to room temperature. HPM have been selected by their encystment stage: to obtain data for HPM, only non-mobile (green vegetative cells) *palmella* stage cells

have been considered, whereas for SHPM mature cyst cells have been studied.¹⁰⁶ The results shown are the average of these measurements.

Morphological and optical characterization. FE-SEM images are acquired with a JEOL JSM-7800F microscope; EDS analysis is performed with an Oxford Instruments analyzer. Microphotographs of the cells have been taken at 1 kV while the EDS analysis is performed at 8-10 kV. Three individual cells from each wafer have been selected randomly. For each alga one SEM image is obtained and the EDS analysis is performed on 6 different regions of the surface.

Optical imaging and Confocal Microscopy of algae samples. Bright-field imaging is performed using an Olympus IX81 microscope controlled by an Olympus IX2-UCB microscope controller. A 20 X objective lens is used. Confocal Microscopy is performed using a Zeiss LSM-710-NLO confocal microscope. The algae samples have been excited at 405 nm and the emission is collected in three different spectral regions: 440-476 nm, 592-631 nm and 670-707 nm corresponding to carotenoid, QD and chlorophyll emission, respectively. Z-stacks have been collected for the selected algae with 20X/0.4 objective lens.

Raman spectroscopy criteria for HPM. Three cells from each wafer have been selected randomly. About 150 Raman spectra have been recorded in different points for each of the selected algae, and averaged to obtain a representative spectrum of each cell sample. The spectra have been collected using a Renishaw Raman System (inVia Raman Microscope) with a 20 X objective lens; the excitation laser wavelength is 785 nm with a power of approximately 5mW on the sample. The integration time for each Raman measurement is 1s and one accumulation has been taken at each measurement point.¹⁰⁷ For the Raman signal detection, the laser light is directly focused onto the surface of the sample. Cell and cell-QDs-AuNPs samples have been measured on dry silicon substrates prepared with the previously mentioned method; the peak frequencies have been calibrated by means of the silicon wafer.¹⁰⁵

3.1.2. Human oral epithelial cells

Oral Epithelial Cells (OECs) have been collected from 20 healthy subjects, which have been chosen by age range between 21 to 31 years old (no smokers). All the subjects were asked not to drink coffee at least twelve hours before the experiment. The OECs samples have been obtained by mechanical exfoliation. To ensure reproducibility, the samples have been taken with an interdental brush using teeth positions as reference points and the samples have been taken from opposing buccal surfaces of first premolar, second premolar, first molar and second molar on both sides.¹⁰⁸ The subjects rinsed their mouth with distilled water before taking the samples.¹⁰⁸ Two samples from every subject have been taken and a total of 40 OECs samples have been collected. Each sample is divided in two, one part is prepared for optical fluorescence and confocal microscopy, and the other part is used in the SEM and the Raman analysis.

Internalization of TGA@CdTe QDs in OECs. The experiment is carried out at room temperature (24°C). To avoid possible interactions of TGA@CdTe QDs with the variety of elements present in the standard PBS, a sodium chloride solution (0.9%) with a pH= ~7 is used. The cells were used immediately after the extraction (“fresh”) with incubation times of 3 minutes. After obtaining the sample, the interdental brush impregnated with OECs is immersed in 1.0 mL of saline solution, stirred for a few seconds and centrifuged at 3600 rpm for 3 minutes. The supernatant is decanted and the OECs have been suspended in 0.5 mL of saline solution. At this point, the sample is divided into four, each one containing 250 µL of OECs dispersed in saline solution. 250 µL of additional saline solution have been added to all four. The control samples are the OECs suspended in saline solution. OECs-BSA sample is obtained by adding 50 µL of BSA to the OECs. After incubation for 5 minutes, the excess of BSA is removed by centrifugation. OECs-QDs sample is obtained by adding 100 µL of QDs (0.56×10^{-5} mol L⁻¹) to the OECs. After incubation for 3 minutes, the excess of TGA@CdTe QDs is removed by centrifugation. Finally, OECs-BSA-QDs have been obtained by adding 50 µL of BSA to the OECs. After incubation for 5 minutes, 100 µL of TGA@CdTe QDs have been added to the OECs-QDs sample. The sample is

further incubated for 3 minutes, and the excess of BSA and TGA@CdTe QDs is removed by centrifugation at 3600 rpm for 3 minutes. All the samples have been suspended in 0.5 mL of saline solution and then two aliquots of 50 μL of each solution are extract and placed on a slide and a silicon wafer. The slide is immediately covered and analyzed under the microscope. This protocol is summarized in figure 15.

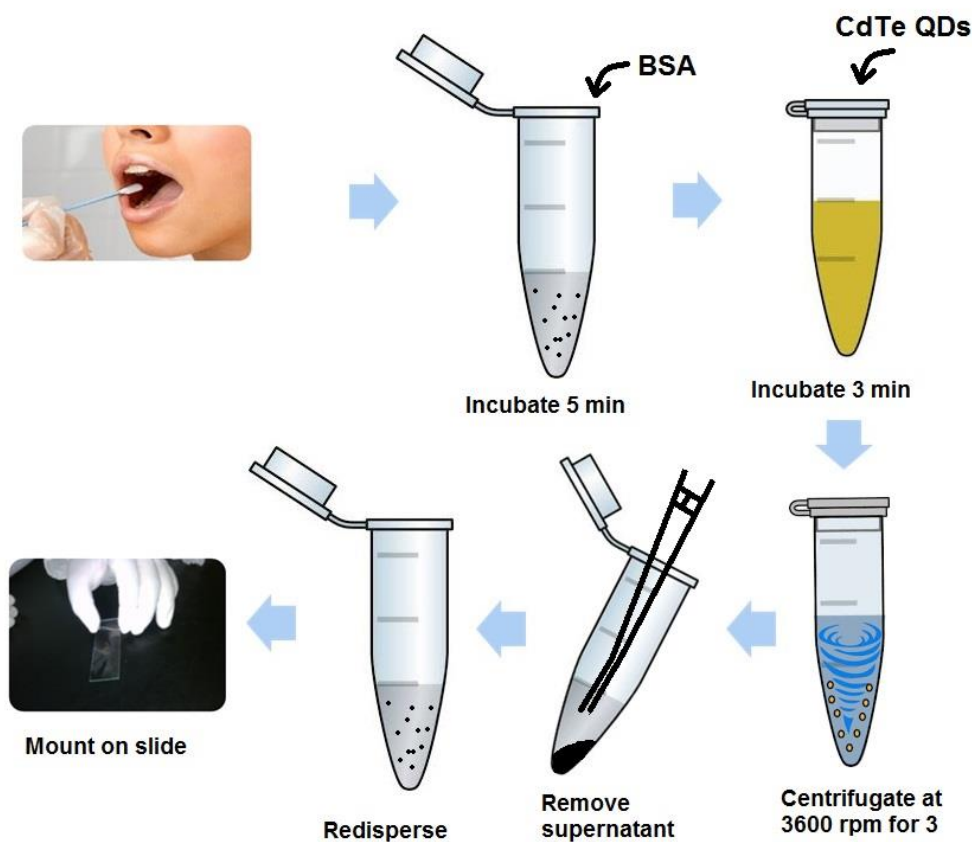


Figure 15. Flowchart of the protocol for sample preparation of oral cells with TGA@CdTe QDs.

Confocal and fluorescence microscopy. The OECs obtained by exfoliation are re-suspended in 1.0 mL of saline solution and 100 μL of NucBlue, Hoechst 33342 are added. After 15 minutes of incubation OECs are centrifuged at 3600 rpm for 3 minutes, the supernatant is removed and the NucBlue-stained OECs are suspended in 1.0 mL of saline solution. Finally, the OECs are incubated in the presence of TGA@CdTe QDs as is described above. Finally, 20 μL of NucBlue-stained OECs-QD sample are placed on the slide and analyzed using the confocal microscope.¹⁰⁹ Confocal microscopy images are obtained by using an Olympus Fluoview FV 1000

laser scanning confocal fluorescence microscope. The nuclei marker (NucBlue, Hoechst 33342) is excited at 405 nm and the OECs-BSA-QDs at 488 nm. The nucleus dye emission is observed at 425-475 nm and the QDs emission at 500-550 nm.

Fluorescence imaging is performed using an Olympus IX81 microscope coupled by an Olympus IX2-UCB microscope controller. The samples are excited using an X-Cite Series 120Q UV lamp coupled to the Olympus microscope, the fluorescence filters at 545-580 and 470-490 nm have been used. The emission is collected at 610 and 520 nm, respectively.

Scanning and Transmission Electron microscopy and EDS. To investigate the localization of AuNPs and TGA@CdTe QDs in the cells, OECs have been analyzed by electron microscopy. The cell samples have been fixed with 4% formaldehyde/2% glutaraldehyde for 4 h at room temperature and rinsed with phosphate buffered saline (PBS). Then the cells have been post-fixed with 1% osmium tetroxide and washed with distilled water. The samples have been dehydrated through ethanol series and finally embedded with LX112 resin. Ultrathin sections (100 nm) have been obtained with an ultramicrotome (Leica Ultracut S). Electron microscopy imaging is obtained using a JEOL ARM 200F microscope operated at 200 kV in STEM (BF/HAADF) mode. Ultra-high resolution Scanning Electron Microscopy (SEM) images have been obtained using a Field-emission gun (FEG) HITACHI S-5500 microscope coupled with Dual BF/ADF detector and energy dispersive X-ray spectroscopy (EDS) to perform chemical elemental analysis.

Raman spectroscopy criteria for OECs. Three fresh OECs from each wafer have been selected randomly. About 150 Raman spectra have been obtained in different points of each OEC sample. Raman spectra with clear peaks have been selected and averaged and thus a representative spectrum of each OEC sample is obtained. Raman spectra have been collected with a Renishaw Raman System (inVia Raman Microscope) with a 20 X objective lens and the excitation laser is operated at 785 nm. The integration time for each Raman measurement is 1s based on some reports.¹⁰⁷ For the Raman signal detection, the laser excitation light is directly focused onto the

surface of the sample with a laser power of ~5 mW. The peak frequencies have been calibrated by means of the silicon wafer.¹⁰⁵ BSA and BSA with TGA@CdTe QDs, have been measured in solution¹¹⁰ using 100 μL of TGA@CdTe QDs and 150 μL of BSA. BSA sample is incubated for 3 minutes with TGA@CdTe QDs before measurement. The laser excitation light is directly focused onto the surface of the sample solution (250 μL).⁶² 30 samples have been prepared and Raman spectra have been obtained in about 200 different cellular positions. The final Raman spectra is the result of the average of approximately 1000 measurements at different OEC locations.

3.2. Interaction of TGA@CdTe Quantum Dots with extracellular matrix of *Haematococcus Pluvialis* Microalgae

The average size of the TGA@CdTe QD that have been used for the study of the interaction with the microalgae cells is ~ 2.8 nm. The concentration of QDs is around $0.56 \times 10^{-5} \text{ mol L}^{-1}$, also derived from the first excitonic absorption peak.⁷⁶ According to previous reports, these concentration is suitable for our purposes.⁷⁷ Colloidal naked anisotropic gold nanoparticles (AuNPs) with an average diameter of ~20 nm and a concentration of $\sim 7.1 \times 10^{10}$ particles/ml have been used; these estimates have been obtained based on previous reports.^{96, 97}

PL spectra of the algae samples have been acquired to assess the emission wavelength of the QD after incubation with the microalgae. These measurements also helped to estimate the overlapping of the fluorescence emitted by the QDs and algal auto-fluorescence. The excitation wavelength in all cases is 400 nm. Figure 16 shows the PL spectrum of (a) HPM, (b) SHPM and the normalized PL spectrum of (c) HPM-QD and (d) SHPM-QD both in the presence and absence of AuNPs; the emission band located at 449 nm corresponds to primary carotenoids, and the band at 682 nm can be attributed to chlorophyll in the photosystem II.¹¹¹ The band at 470-550 nm is related to the presence of secondary carotenoids, which in this case it corresponds to astaxanthin.¹¹² Therefore the presence of these band is more remarkable in figure 16 (b). However, in figure 16 (c) and (d) this band overlaps with the strong fluorescence of the QDs. On the other hand, non-stressed cells have a higher emission associated to chlorophyll (figure 16 (a)) than in the case of stressed cells (figure 16 (b)). Both samples containing QDs

(figure 16 (c) and (d)) exhibit a strong emission at 562 nm, which is attributed to the presence of QDs, and smaller peaks corresponding to the photosynthetic pigments (449 and 682nm). The presence of AuNPs does not alter the emission wavelength of the samples, only intensity changes are observed.

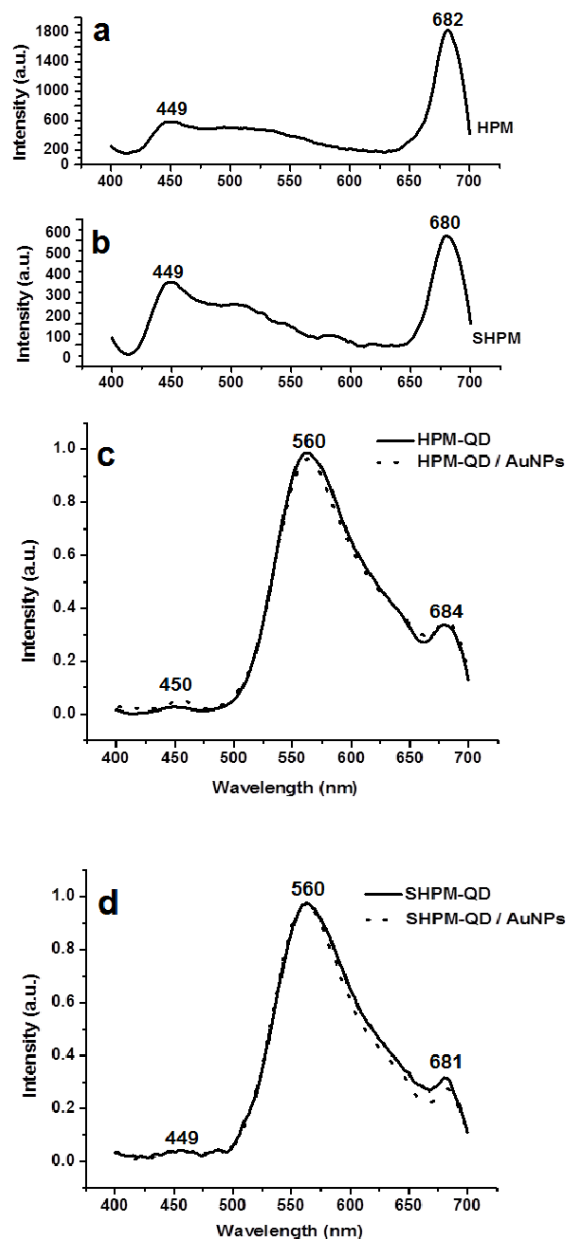


Figure 16. Photoluminescence (PL) spectrum of (a) HPM, (b) SHPM, (c) HPM-QD and HPM-QD/AuNPs and (d) SHPM-QD and SHPM-QD/AuNPs. Samples have been excited at 400 nm.

Figure 17 shows images of HPM and SHPM samples with and without QDs obtained by optical microscopy and SEM. Panels (a) through (d) show fresh algae in bright field. The presence of the ECM is clearly visible in HPM and HPM-QDs samples as a nearly transparent layer of variable thickness, see Figure 17 (a) and (b), and HPM-QDs sample shows a change in color (see figure 17 (a) and (b)) while as expected the ECM is absent in SHPM and SHPM-QDs cells, see figure 17 (c) and (d). Mature cyst SHPM show no significant changes in color when viewed in bright field (see figure 17 (c) and (d)). SEM images of algae fixed on silicon are displayed in figure 17 (e) to (h). A distinctive round shape is observed in the control cells, see panels (e) and (g). The collapse in the structure of the algae is observed for the HPM-QDs sample (see figure 17 (f)), indicating damage to the cell. SHPM-QDs do not show such damage (see panel (h)), which it is attributed to the existence of the secondary wall.

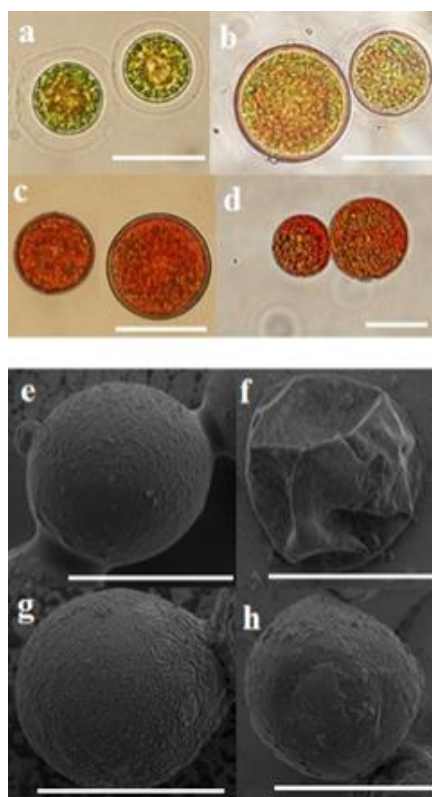


Figure 17. Bright field microscopic images of fresh HPM samples. Non- mobile “palmella” stage: (a) HPM, (b) HPM-QD; and mature cyst: (c) SHPM, (d) SHPM-QD. SEM images of HPM fixed on silicon: (e) HPM, (f) HPM-QD, (g) SHPM, (h) SHPM-QD. Scale bar represents 20 μm .

After 5 minutes of incubation TGA@CdTe QDs are not internalized and accumulate in the ECM of HPM. In contrast, confocal images for SHPM-QD show a very small

amount of QDs on the outside of the secondary wall. The secondary wall of SHPM is thought to be acting as a barrier. Since HPM has no such secondary wall, TGA@CdTe QDs could adsorb onto the ECM. Even if QDs cause damage to the robust cell wall of HPM, no evidence of internalization is obtained even for a two-hour incubation. This is consistent with that reported by Mahan et.al.⁴³ Probably complete internalization is prevented by the thick cell wall of these algae.

In HPM-QD, cell disruption is observed in most algae, see fig. 17 (f). This damage to the cell structure may be a consequence of ROS and/or the occurrence of cadmium ions. Both sources of CdTe QDs toxicity have been widely discussed and reported.^{23,24} Also Cd²⁺ ions could have been attracted to the cell membrane, because of its negative potential.¹¹³ The cell wall of SHPM is around 2 µm thick and has low permeability therefore it is mechanically and chemically resistant to nanoparticles.³⁸ Consequently, during the incubation period, few QDs are capable of interacting with the secondary wall of SHPM.

The presence of cadmium and tellurium on the surface of QD-treated algae is analyzed by EDS element analysis; obtained EDS spectra in the range of 2 to 5 keV are shown in Figure 18. The elements found in the cell-QDs samples are as following: cadmium (Cd), tellurium (Te), carbon (C), Oxygen (O), nitrogen (N), phosphorus (P), sulfur (S), sodium (Na) and chlorine (Cl), as obtained by EDS analysis for the different algae samples. For the HPM-QD samples, cadmium and tellurium are found with a large concentration of cadmium (~15.6%) and tellurium (~3.9%) (see figure 18 (a) and (b)). In contrast, for SHPM-QD, smaller amounts of cadmium (~2.8%) and tellurium (~0.4%) are observed than in the case of HPM-QD (see figure 18 (b) and (d)). EDS analysis is obtained for a drop of QDs, as a control sample; a greater presence of cadmium is observed compared to that of tellurium. This has been widely reported as a result of the presence of CdS in the colloidal synthesis which could take the form of a shell around the CdTe core created by mercapto-groups covalently attached to the surface cadmium atoms⁷³.

Figure 18 (e) shows the EDS spectrum obtained for a HPM-QDs/ AuNPs, the inset shows AuNPs aggregates that have been found on the cell sample. This aggregates are known to promote surface-enhanced Raman spectroscopy SERS due to the high local optical fields in the hot spots of gold cluster structures. As reported, AuNPs

aggregates in a size range of 100-150 nm and consisting of a minimum of 5-10 individual nanoparticles provide at least one hot spot exhibiting an enhancement at a level that makes these nanostructures SERS-active for non-resonant single-molecule Raman detection.¹⁰⁷

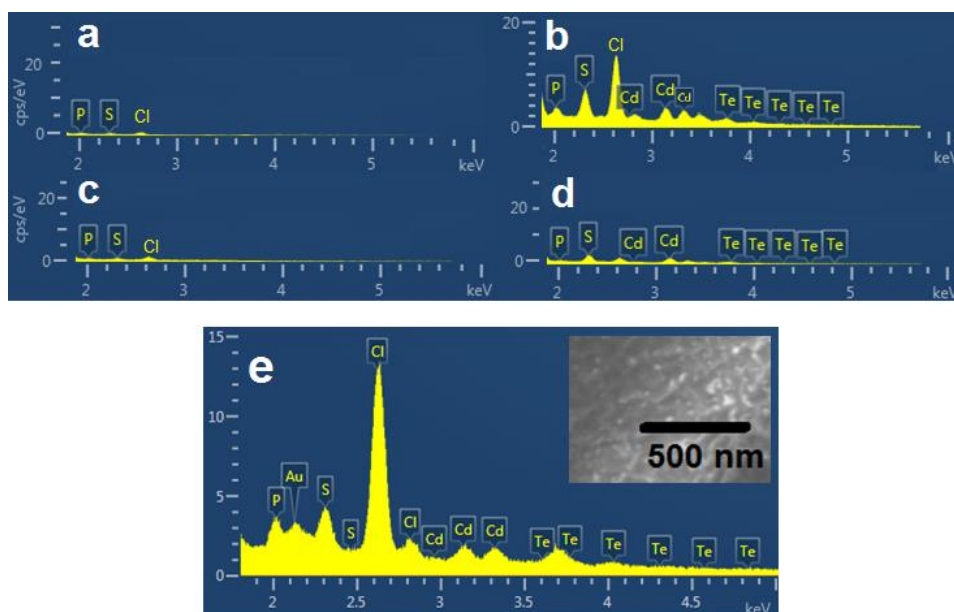


Figure 18. EDS spectrum showing the composition of (a) HPM, (b) HPM-QD, (c) SHPM, (d) SHPM-QD and (e) HPM-QDs/AuNPs, in the range of 2 to 5 keV. The inset in (e) shows the adsorbed AuNPs.

The localization of the TGA@CdTe QDs in the ECM of HPM is observed by confocal microscopy. Emission and excitation ranges have been proposed based on the PL spectra of the selected QDs. Samples have been excited at 405 nm and the emission is collected in three specific bands: 440-476 nm, 560-631 nm, and 670-707 nm, corresponding to the emission of primary carotenoids, QDs, and chlorophyll, respectively. The plane in depth at which the diameter of the algae is maximum is regarded as the central plane for the Z scan, based on previously reported criteria.¹¹⁴ To delimit the ECM and the plasmalemma, the emission of chlorophyll (shown in red) is taken as reference since it is known that chlorophyll is not present in the ECM.³⁸ In HPM (figure 19 (a)-(d)), a considerable auto-fluorescence due to chlorophyll is seen while the signal from the primary carotenoids is low. HPM-QD (figure 19 (e)-(h)) show similar chlorophyll auto-fluorescence and the QDs appear to be localized within the ECM. The SHPM-QD sample shows non-specific localization of the QDs, which

appear to be in some parts on the outside of the secondary wall (figure 19 (m)-(p)). These results are in agreement with the spectra shown in figure 16 (c) and (d). The small signal observed in the band of 562-631 nm in HPM and SHPM samples (see figures. 19 (d) and (l)) corresponds to secondary carotenoids, see figure 16 (a) and (b).

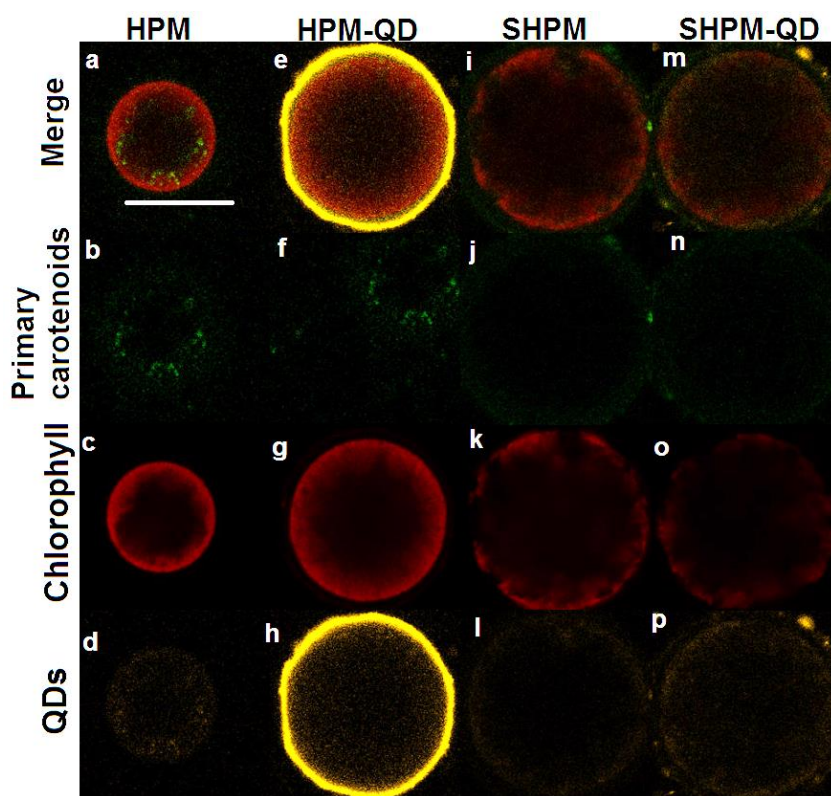


Figure 19. Confocal microscopy images of microalgae. (a-d) HPM, (e-h) HPM-QD, (i-l) SHPM, (m-p) SHPM-QD. First row corresponds to all emissions. Second row shows the fluorescence of primary carotenoids, third row corresponds to chlorophyll emission and fourth row corresponds to QD emission. Samples have been excited at 405 nm and the emission is collected in three specific bands: 440-476 nm, 592-631 nm, and 670-707 nm, corresponding to the emission of carotenoids, QDs, and chlorophyll, respectively. Scale bar 20 μ m.

Internalization of AuNPs is not observed. AuNPs are adsorbed on the surface of cells in the conditions necessary to promote SERS, as is the formation of gold nanoaggregate cluster structures, formed by individual nanoparticles.^{52, 64, 83, 107} Since TGA@CdTe QDs are also not internalized but adsorbed and distributed in the ECM, this meets the optimum conditions for SERS enhancement that enables chemical probing of the interaction of QD with the ECM in the nano-environment of the AuNPs.

Figure 20 displays the SERS spectra obtained for the HPM and SHPM samples. The AuNPs enhanced the Raman signal by \sim 5 times in comparison when using

samples without AuNPs, see figure 20 (a) and (b) (B and C). Figure 20 (a(C)) shows the Raman spectrum of HPM/AuNPs, characteristic peaks associated to chlorophyll (746, 987, 1046, 1285, 1305, 1327, 1490, 1550 and 1611 cm^{-1})¹¹⁵⁻¹¹⁹ and carbohydrates (1069 and 1112 cm^{-1})^{39, 116, 120, 121} are present. As reported around 42% of HPM volume is constituted by chloroplasts.³⁹ The bands at 1157 and 1526 cm^{-1} are assigned to the presence of both primary and secondary carotenoids, being the primary carotenoids those known to be found in a higher concentration in the HPM, see figure 20 (a (C)).³⁵ In the Raman spectrum of HPM-QDs/AuNPs, some peaks associated with chlorophyll increased their intensity, these peaks are marked with stars in figure 20 (a (D)), and the range between 915 and 1004 cm^{-1} shows significant changes. For instance, whereas HPM/AuNPs (figure 20 (a (C)) shows a band at 963 cm^{-1} attributed to the O-C-H bending vibration of carbohydrates, features at 940 cm^{-1} appear in HPM-QDs/AuNPs (figure 20 (a (D))).^{121, 122}

Peaks associated to chlorophyll are absent or minimal in the SHPM/AuNPs (figure 20 (b (C)) sample, however, carotenoid (964, 1006, 1157, 1193, 1275, 1445, 1521 and 1596 cm^{-1})^{35, 115, 122-125} and lipid (876 cm^{-1})¹²⁰ bands corresponding to astaxanthin accumulation^{36, 38} are present, see figure 20 (b). This result is expected and is consistent with previous reports.^{34, 35, 38} Both SHPM/AuNPs (figure 20 (b (C)) and SHPM-QD/AuNPs (figure 18 (b (D))) show a peak at 876 cm^{-1} assigned to carbohydrates and lipids in agreement with the presence of a thick cell wall made of polysaccharides like algaenan and mannan³⁸ (figure 20 (b (C))). The band at 1157 cm^{-1} is assigned to ν_2 carotenoids (stretching C-C) while the band at 1521-1522 cm^{-1} is assigned to ν_1 carotenoids (in-phase C=C).^{35, 126} Overall, no spectral changes after incubation with QDs have been detected for SHPM-QD/AuNPs (figure 20 (b (D))).

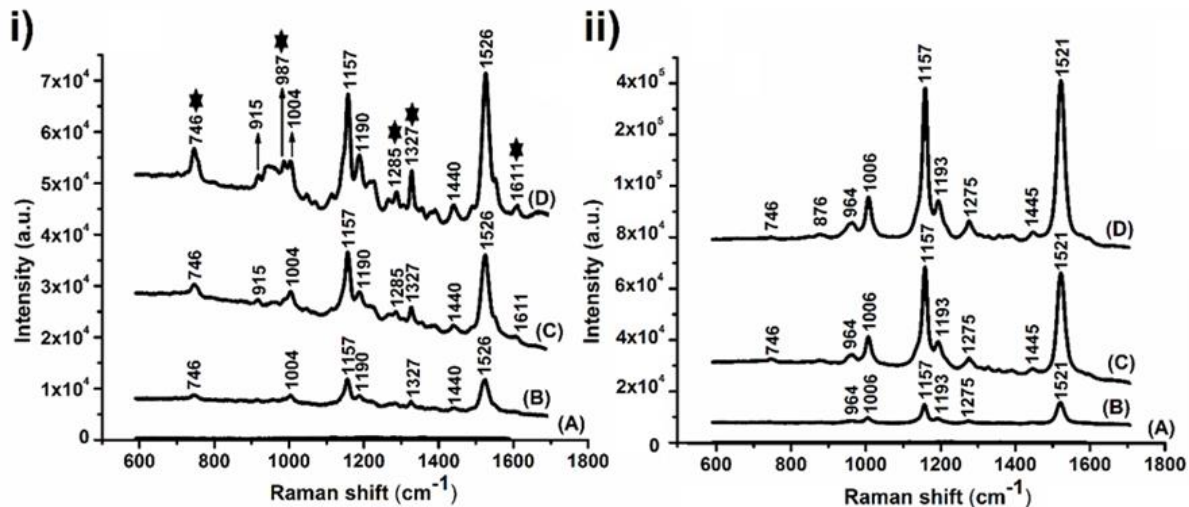


Figure 20. i) Raman spectra obtained from: (A) AuNPs, (B) HPM, (C) HPM/AuNPs and (D) HPM-QDs/AuNPs. Stars indicate the bands that increased intensity after incubation with TGA@CdTe QDs. ii) Raman spectra obtained from: (A) AuNPs, (B) SHPM, (C) SHPM/AuNPs and (D) SHPM-QDs/AuNPs.

The SERS effect is obtained by the incubation of the algae with the naked AuNPs which do not present any bands in the Raman spectrum. Since the SRP of the AuNPs is located at 535 nm while the excitation signal used is 785 nm, the SERS effect is due to the easy adsorption of these small AuNPs on the cell surface and the formation of aggregates that could resonate at wavelengths greater than its SRP. ^{52, 64, 107}

Differences in the Raman shifts between HPM/AuNPs and HPM-QDs/AuNPs samples have been found at the 915- 1004 cm⁻¹ band. The band at 985 cm⁻¹ is presented as a shoulder in HPM/AuNPs whereas in HPM-QDs/AuNPs a defined peak is observed, matching the intensity of the characteristic peak at 1004 cm⁻¹ assigned to ν_3 carotenoids (CH₃ stretching mode).

In-plane C-C stretching modes of pure TGA and TGA@CdTe QDs have been reported at 992-994 cm⁻¹ ^{127, 128} and the shift toward lower frequencies (~10 cm⁻¹) or the enhancement of this band has been reported in relation to changes in the interaction of the sulfur atom from the TGA molecule and the QD. The enhancement of the 987 cm⁻¹ band in the HPM-QDs/AuNPs spectrum may be related to changes between the QD core and the TGA capping agent produced by an interaction with the ECM. The main spectral differences between HPM/AuNPs and HPM-QDs/AuNPs manifest in a band assigned mostly to carbohydrates. This is because the main component of the ECM of HPM are glycoproteins which have a high carbohydrate content such that protein content constitutes in some cases

only 5 % of the glycoprotein weight.¹²⁹ Also the chemical composition of the ECM and the algae cell wall consists of cellulose, polysaccharides, and the aforementioned glycoproteins. Therefore it has numerous binding sites for TGA@CdTe QDs through nonspecific interactions (such as electrostatic, hydrophobic, and hydrogen bonding) or the interaction between the carboxylic groups (-COOH) of the TGA and the amine groups (-NH₂) of the ECM and the algal cell wall.⁴³ Moreover the band with maximum at 940 cm⁻¹ has been reported as out-of-phase C-O-C ring vibrations of polysaccharides¹³⁰. Therefore, the manifestation of this band after incubation with TGA@CdTe QDs strongly suggests the interaction of the TGA@CdTe QDs with the saccharides. Moreover, sugar-modified TGA@CdTe QDs have been widely discussed and can be produced by simple incubation of TGA@CdTe with saccharides.¹³¹ As it has been reported, quantum yields are related to traps on the surface of CdTe QDs that mainly originate from Te atoms with dangling bonds and these traps could be occupied by saccharides that can adhere to the surface of the CdTe QDs by electrostatic forces. This occurs for example with D-glucose, one of the sugars present in plant cells.¹³¹

Previous reports show that Raman modes corresponding to the crystalline core, Te defects of the CdTe QDs and the interactions between the QD core and the thiol capping have been found in the low Raman shift regime (100 -310 cm⁻¹) and vibrational modes of the thiol capping agents have been reported between 310 and 1750 cm⁻¹.¹²⁷ Reported TGA@CdTe QDs shifts are not found in any spectra of the algae samples due to their weak Raman scattering in aqueous media compared to elastic scattering.¹²⁷

Several peaks of HPM-QDs/AuNPs, in the region of 1100-1620 cm⁻¹ assigned to chlorophyll increased their intensity (~3 times) compared to the intensities of the same peaks of HPM/AuNPs and with reference to the characteristic peaks of carotenoid bands (1157-1526 cm⁻¹). This increase of the intensity given the presence of the TGA@CdTe QDs may indicate that ROS are already attacking the HPM. This is consistent with previous reports indicating that when HPM are exposed to ROS, the chloroplast are found to be the main site of oxidative damage.⁴² Therefore the increase in intensity of chlorophyll-associated bands in HPM-QDs/AuNPs could be a direct result of ROS interacting with the chloroplasts and damaging the structure, thus releasing the chlorophyll.

Raman spectrum of SHPM exhibits no changes after incubation with QDs, indicating that the interaction between the TGA@CdTe QD and the secondary cell wall is very low. However, a small presence of TGA CdTe-QDs in SHPM-QDs sample is confirmed by EDS analysis, the PL spectrum and confocal microscopy. A protective role of astaxanthin against QD toxicity is not confirmed due to the absence of internalized QDs in SHPM-QD.

3.3. Interaction of TGA@CdTe quantum dots with human oral epithelial cells

For experiments with human oral epithelial cells (OEC), colloidal TGA@CdTe QDs, with the maximum absorption and emission peaks centered at 520 nm and 560 nm, respectively, are used. The average size of the TGA@CdTe QDs is ~3.3 nm. The concentration of QDs is around 0.60×10^{-5} mol L⁻¹, which is determined based on previous reports.⁷⁶ The concentration is suitable for cell-nanoparticle interactions and toxicity analysis purposes.⁷⁷ Zeta potential of QDs is measured, resulting in a negative value of -27.3 mV as an indication of the presence of the TGA group. AuNPs with an average diameter size of ~20 nm and a molar concentration of $\sim 5.4 \times 10^{-10}$ mol L⁻¹, using the methodology reported by Liu et al. have been selected.⁸²

OECs are transparent and their auto-fluorescence is not considerable when excited at 470-490 nm and collecting the emission at 520 nm.¹³² Therefore the need to use markers to distinguish the main organelles of the cell such as the nucleus are necessary and relevant. Figure 21 shows fresh OECs viewed under the optical fluorescence microscope. OEC samples have been excited at 470-490 nm and the emission is collected at 520-560 nm. Figure 21 (a) and (b) shows OECs, in the absence of BSA-TGA@CdTe QDs, displaying a low auto-fluorescence. Figure 21 (c) and (d) show images of OECs incubated in the presence of TGA@CdTe QDs, all OECs showed some signals of cellular damage (lack of nuclei and/or cell membrane disruption). Figure 21 (e-h) show the micrograph of OECs incubated with both BSA and TGA@CdTe QDs (OEC-BSA-QDs). Some of the structural features like a well-defined nucleus and morphology of the OECs due to the presence of TGA@CdTe QDs are observed. In addition, it can be proposed that the TGA@CdTe QDs have been evenly distributed all over the cell body. Figure 21 (i) shows the bright field image of OECs

incubated in the presence of BSA and TGA@CdTe QDs. This figure shows that the morphology of the OECs remains after being exposed to TGA@CdTe QDs for three minutes, as an indication of the decrease of toxicity due to the presence of BSA.

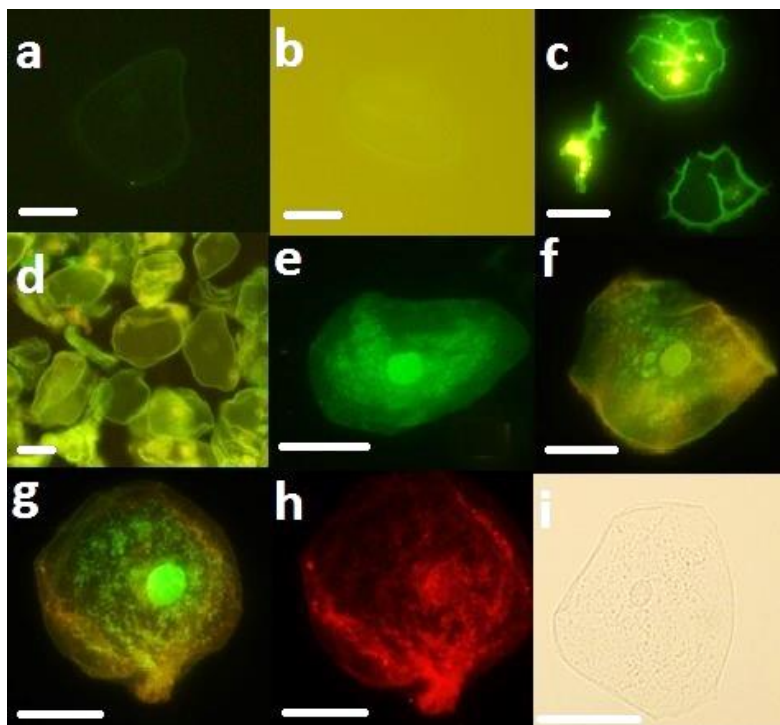


Figure 21. Fresh OEC viewed under the optical microscope. (a), (b), (c), (d), (e), (f) and (g) have been excited at 470-490 nm and the emission is collected at 520 nm. In (h) the OEC is excited at 545-580 nm and the emission is collected at 610 nm. (a) One OEC, (b) one OEC incubated with BSA, (c) and (d) OEC incubated with QDs1. (e) One OEC incubated with BSA and later in QDs1. (f) one OEC incubated with BSA and later in QDs2. (g) and (h) have been OEC incubated with BSA and later in TGA-CdTe QDs, the capture wavelength is 520 nm and 610 nm respectively. (i) One OEC incubated with BSA and later in TGA-CdTe QDs in bright field. Scale bar represents 20 μm .

Figure 22 shows images obtained by confocal microscopy of a fresh OEC stained with a conventional nuclear staining (NucBlue) and TGA@CdTe QDs. Figure 22 (a-c) shows the cell nucleus for the emissions at 425-475 nm (conventional staining figure 22 (a)), 500-550 nm (TGA@CdTe QDs figure 22 (b)) and the overlap of both emissions (figure 22 (c)). The conventional staining matches the emission of TGA@CdTe QDs, see figure 22 (c). Figure 22 (d) shows the resulting images of the OEC depth scanning having an emission at 500-550 nm. Images have been acquired every 0.6 μm thickness and the highest nucleus intensity is observed at 8.4 μm below the cell surface. A significant concentration of TGA@CdTe QDs is observed inside the nucleus overlapping with the conventional nuclear-staining solution.

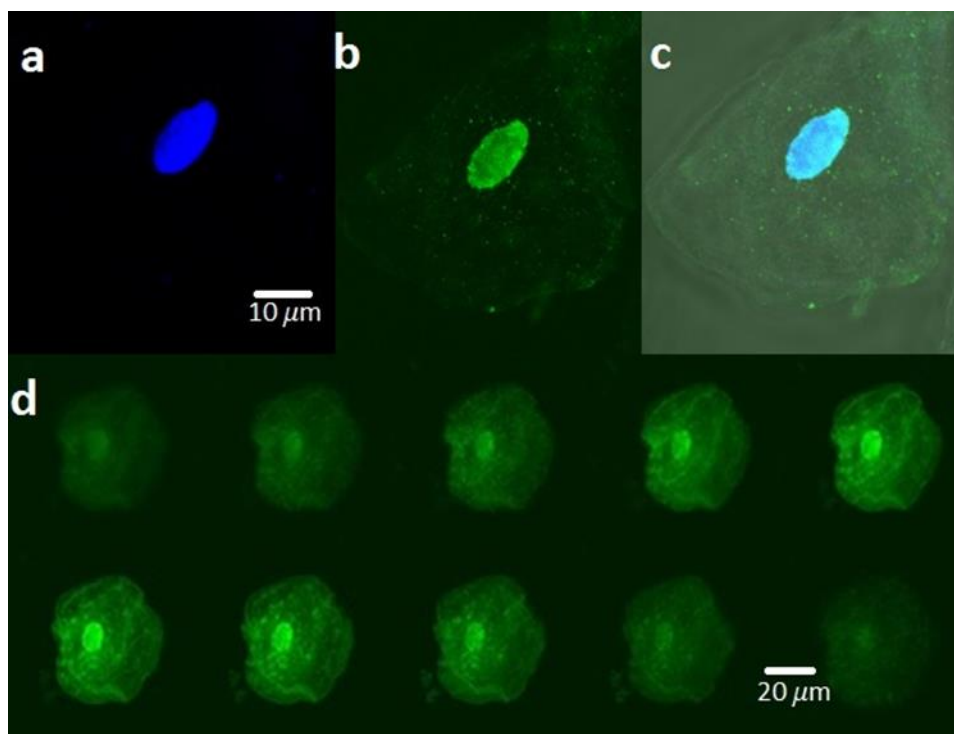


Figure 22. OEC stained using a nucleus conventional marker (NucBlue™) and TGA@CdTe QDs. (a) OEC emission at 425-475 nm (blue). (b) OEC emission at 500-550 nm (green). (c) Merge of both emissions. (d) Series of z-stacks in depth from the OEC emission at 500-550 nm.

Figure 23 shows SEM images of OECs having irregular patterns of microridges and rod-like elements, corresponding to bacteria adhered to the membranes (figure 23 b (A)). OECs incubated with TGA@CdTe QDs showed signs of damage such as the disruption of portions of the cell membrane (figure 23 b (B)). Some OECs also exhibited a total loss of texture and ruptures in the membrane (figure 23c). The OEC incubated with AuNPs-BSA-QDs revealed the presence of AuNPs on the surface of the cell (figure 23 d). OECs have been not stained with heavy metals to avoid noise signals and facilitate location of electron-dense QDs and AuNPs. Due to their small size, TGA@CdTe QDs can easily pass cell membrane and distribute into the whole cytoplasm with eventual location within the nucleus.²¹ This behavior is observed by fluorescence and confocal microscopy (figures. 18 and 19). Due to the high affinity of QDs for proteins and nucleic acids, their interaction with these molecules may cause protein dysfunction and genotoxicity with different levels of susceptibility to exert cytotoxic effects. These toxic effects may occur within five minutes.^{23, 24} In this work, it is observed that after the first three minutes of incubation, the TGA@CdTe QDs are efficiently internalized inside OECs, but a high level of cytotoxicity is observed. However, the

antioxidant effect of BSA^{24, 133} had an indispensable role to reduce such fast cell death. The rapid and efficient distribution of the TGA@CdTe QDs inside of the cells is probably due to facilitated diffusion. This internalization mechanism is based on integral membrane proteins that interact with charged, hydrophilic and polar molecules, which are in the same size range of TGA@CdTe QDs.^{24, 134-136}

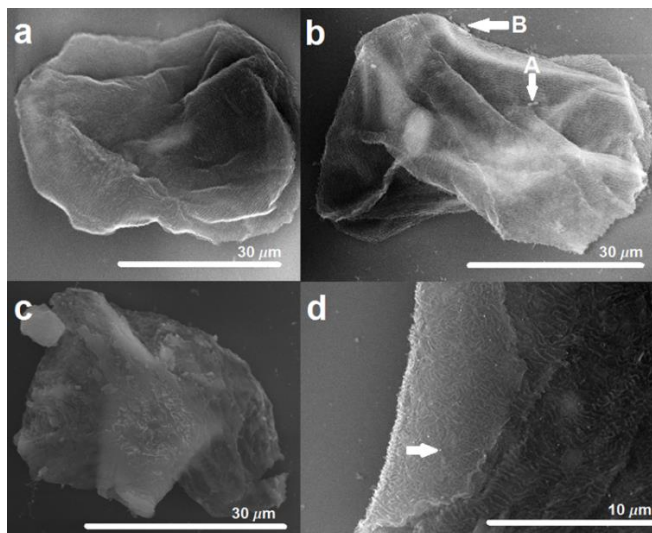


Figure 23. SEM imaging of oral epithelial cells. (a) OEC. (b) OEC-BSA-QDs, white arrow: (A) bacteria adhered to the cell membrane and (B) detachment of the membrane material. (c) Damaged OEC-QDs. (d) OEC-AuNPs-BSA-QDs, white arrow indicates the presence of gold nanoparticles.

Imaging of whole OECs through ultra-high resolution SEM provided initial insights of the morphological changes and cellular responses of OECs upon interaction with TGA@CdTe QDs. The SEM samples are not stained with heavy metals nor coated; therefore, the contrast or electron-dense regions corresponded specifically to sites of adsorption of inorganic particles. In comparison with control, OECs incubated with TGA@CdTe QDs showed early signs of response to QDs. Specific signs include: cell shrinkage, membrane protrusions and loss of characteristic microvilli. The OECs samples that have been treated with BSA showed an evident reduction of the adverse responses. In these samples, the OECs kept the cell integrity, morphology and membrane arrangement. Even in the presence of BSA, the high affinity of OECs for TGA@CdTe and AuNPs is evident, since we found nanoparticles attached all over the cell membranes (white dots in figures 23 b-c-d).

The presence of gold, cadmium and tellurium on the surface of QD-treated oral epithelial cells is analyzed by EDS element analysis. The EDS spectra is obtained in the range of 1 to 5 keV (figure 24). The elements found in the cell-QDs samples are the following: gold (Au), cadmium (Cd), tellurium (Te), carbon (C), Oxygen (O), sulfur (S), sodium (Na) and chlorine (Cl).

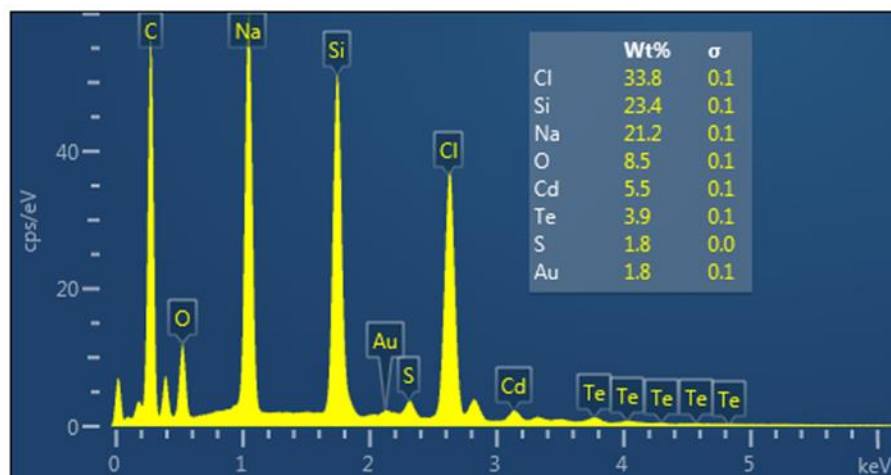


Figure 24. EDS spectrum showing the elemental composition of an OEC containing AuNPs-BSA-QDs.

To shed light on the internalization and intracellular location of TGA@CdTe QDs and AuNPs, STEM images of ultra-thin sections of the OEC samples have been acquired. Figure 25 (a) shows an OEC incubated with TGA@CdTe QDs presenting some of the characteristic features of the cell such as the nucleus (A), detachment of membrane portions (B) and glycosylated membrane components functioning as receptors (C).¹³⁷ Figure 25 (b) shows a magnified image of the cell membrane, it is observed that some cilia fibers have a high content of TGA@CdTe QDs (A). The presence of TGA@CdTe QDs across the cell membrane is also observed (B). Moreover, inside the cell body, TGA@CdTe QDs appear to be located in the cytoskeleton (C). The existence of early endosomes is not observed. The presence of TGA@CdTe QDs in tonofilaments is generally observed throughout the cell and in the inner part of the nucleus (figure 25 (c)). This is consistent with the results obtained by optical microscopy. Finally; in OECs incubated with both AuNPs and TGA@CdTe QDs, it is observed that the AuNPs could have been internalized through an endocytic pathway. Figure 25 (d) shows plasma membrane invagination and early endosomes formed during the internalization of AuNPs. Interestingly, oral cavity microorganisms have been also found in

the samples. A dividing coccus or diplococci (Figure 25 d (A)) with its multiple layer wall, could be adhered via glycocalyx to the epithelial microvilli-like protrusions (figure 25 d (B)).¹³⁷

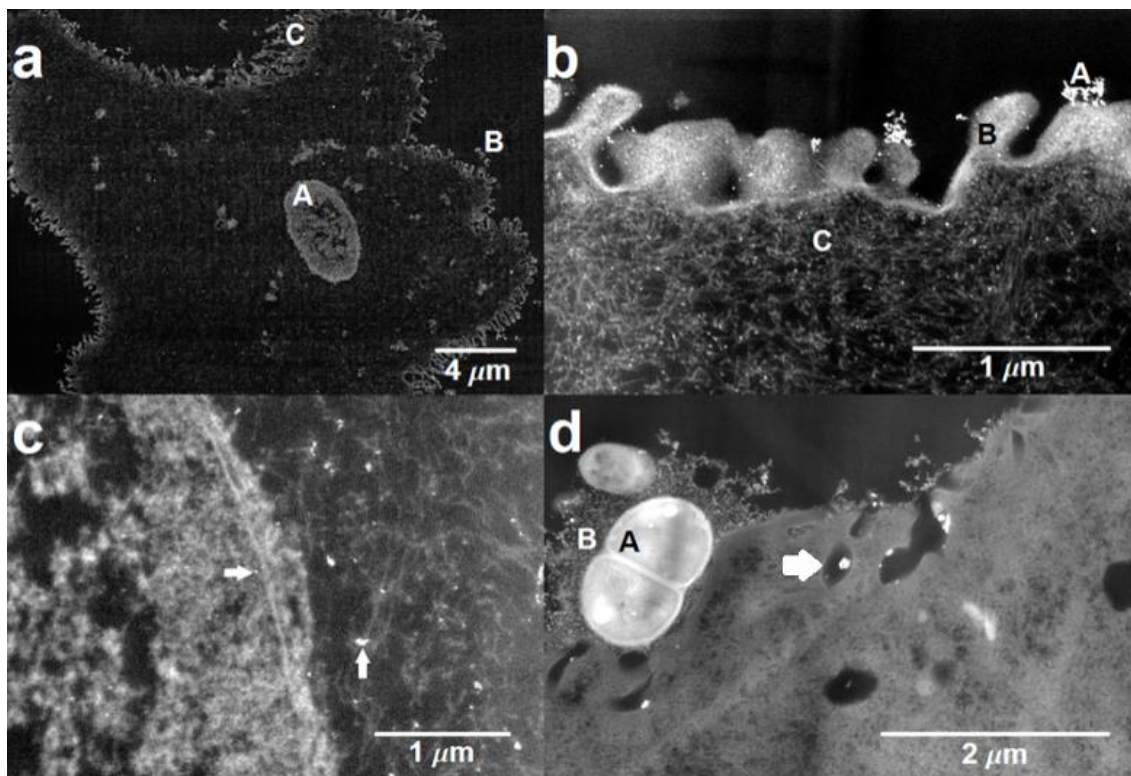


Figure 25. Ultrastructural location of TGA@CdTe QDs and AuNPs. STEM images illustrating: (a) OEC-BSA-QDs where (A) is the nucleus, (B) disruption of the cell membrane and (C) cilia. (b) OEC-BSA-QDs where cilia fibers can be observed with a high content of TGA@CdTe QDs (A). (c) Zoom in to the cell nucleus and its environment in a OEC-BSA-QDs sample, white arrows indicate the presence of TGA@CdTe QDs. (d) OEC-AuNPs-BSA-QDs: (A) A dividing coccus or diplococci with a multiple layer wall adhered via glycocalyx (B) to the epithelial microvilli-like protrusion. The white arrow points to AuNPs sequestered in an early endosome.

Annular dark field (ADF)-STEM imaging of ultra-thin sections clearly revealed the accumulation into membrane components of the TGA@CdTe QDs and AuNPs even after only few minutes of incubation. The advantage of using ADF detector is that it provided a Z-contrast image (where Z is atomic number), which helps to efficiently locate the high contrast inorganic particles. TGA@CdTe QDs entered quickly and efficiently into the cells; upon internalization, the particles are distributed all over the cytoplasm with eventual nuclear invasion (figure 25 c). Due to the size and high affinity of QDs for biomolecules, because of the presence of the thiol capping agent, the interactions with the membrane biomolecules are observed. These interactions resulted in cell damage and alterations of the integrity and

arrangement of bio-membrane structures. The absence of early endosomes, which is usually associated to endocytosis, provided insights of the possible mechanisms of internalization of TGA@CdTe QDs. We hypothesize that the internalization is carried out through facilitated diffusion mechanism. The QDs and proteins have similar dimensions and the formation of QD-peptide conjugates has already been studied. The conjugation of TGA@CdTe QDs with sugars and glycoproteins has also been widely reported.¹³⁸⁻¹⁴⁰ In contrast, AuNPs internalize in OEC via endocytosis as previously reported for Au particles in the same size range. The results obtained in this work with STEM imaging are in good agreement with previous reports.^{141, 142} An important consideration for both nanoparticles is their high affinity for proteins causing their adsorption through electrostatic interactions.^{143, 144} Therefore, the AuNPs may locate in the vicinity of TGA@CdTe QDs inside and outside the cells.

The Raman spectra of pure AuNPs did not present any spectral features (figure 26 (a)). Spectral features of the cells incubated with and without BSA (not shown) are identical. Moreover, no changes in the Raman spectrum of BSA have been found after incubation with TGA@CdTe QDs (figure 26 b-c). The naked AuNPs have been used to promote SERS on the OEC samples. In the absence of AuNPs, no Raman peaks have been obtained (figure 26 (d)). The Raman spectra have been acquired in the amide III region, since this region does not present interference with OH vibrations from H₂O. In addition, amide III region has been used as a direct qualitative indicator for conformational change in proteins.¹⁴⁵ Figures 26 (e) and (f) show the Raman spectra of OECs in the presence of AuNPs and BSA-QDs-AuNPs, respectively. The Raman signal of OEC-BSA-AuNPs is presented in figure 26 (e) and yields peaks at 918, 1120, 1246, 1353, 1433 and 1470 cm⁻¹. These peaks are assigned to C-C stretch of proline ring, C-C stretching mode of lipids and proteins, amide III of amino acids, tryptophan, CH₂ (lipids in normal tissue) and lipids, respectively.^{59, 105, 108, 146} As it has been reported, spectral features of healthy OECs are dominated by the CH₂ band and a higher lipid content.¹⁰⁸ The Raman spectra of OEC-BSA-QDs-AuNPs (figure 26 (f)) showed peaks at 845, 938, 1030, 1120, 1253, 1322 and 1407 cm⁻¹. These peaks correspond to glucose, collagen, phenylalanine of collagen/ keratin, C-C stretching mode of lipids and proteins, amide III, CH₃CH₂ twisting of collagen and bending modes of methyl groups (collagen), respectively.^{59, 105, 108}.

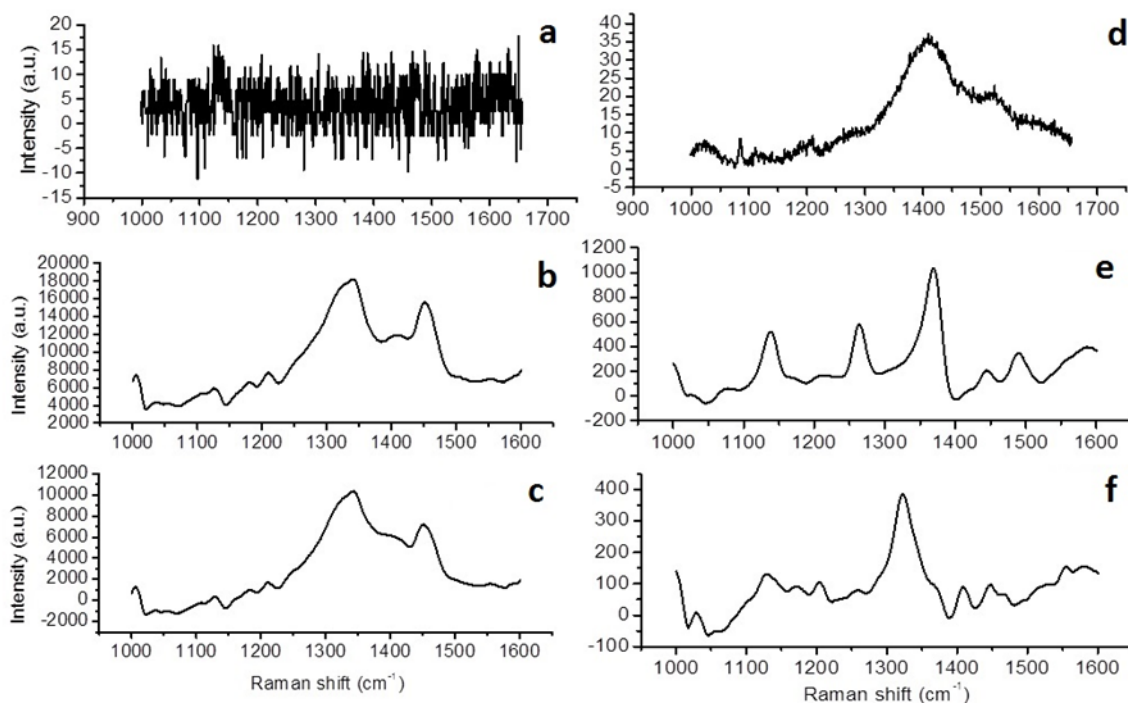


Figure 26. (a) Raman spectra of AuNPs. (b) Raman spectra of BSA. (c) Raman spectra of BSA - QDs (d) Raman spectra of OEC. (e) Raman spectra of OEC with AuNPs. (f) Raman spectra of OEC -AuNPs-BSA - QDs.

To gain a deeper and more accurate knowledge of the specific interactions occurring at the molecular level, we identified characteristic SERS peaks on OECs upon interactions with TGA@CdTe QDs and TGA@CdTe QDs-AuNPs. From the spectroscopic analysis, a significant enhancement of up to $\sim 10^4$ in the OECs Raman signals is observed when using AuNPs as nanosensors. As it has been widely reported, nano-rods, aggregated Au nanostructures and cluster structures formed by individual gold nanoparticles could show SERS activity due to the formation of hot-spots.^{52, 64, 83, 107} On the other hand, it is known that proteins may be absorbed onto the surface of the colloidal nanoparticles mainly through electrostatic interactions forming a layer known as “protein corona”. In our case, the enhanced bands due to the presence of AuNPs are assigned to vibrations of functional groups of protein residues (aromatic groups and amines) and glycans attributed to glycoproteins located in glycocalyx.¹⁴⁴

in this work, the enhancement of the Raman signal due to the presence of SERS substrates is calculated by using the formula: $E = (A_{\text{SERS}}) / (A_{\text{REF}})$; where A_{SERS} is the area of the SERS peak (from the OEC-BSA-AuNPs average spectrum, see figure 26 (e)) and A_{REF} corresponds to the calculated area obtained for the same integration interval from the OEC-BSA average Raman spectrum (see figure 26 (d)). The integration intervals were selected from the medium height of the approximate Gaussian curve to the maximum peak value. Baseline corrections, when applied under the same criteria to A_{SERS} and A_{REF} or smoothing by the Stavitzky-Golay method (second polynomial order 5-point window) did not alter the enhancement result in order of magnitude. When making a comparison between the Raman spectra of OEC-BSA-AuNPs with OEC-BSA-QD-AuNPs it can be concluded that there are molecular changes due the presence of TGA@CdTe QDs in the cells. One of the main components of OECs membranes are glycoproteins and collagen.^{59, 147, 148} Additionally, one of the main proteins in the cytoskeleton is keratin.¹⁴⁹ Evident changes in the region of the amine III (1200-1350 cm^{-1}) related to glycans, collagen, keratin and protein residues are observed after the incubation of the OECs with TGA@CdTe QDs (figure 26 (e) and (f)). These changes may be due to the interaction of TGA@CdTe QDs with glycoproteins and membrane proteins during the internalization process.

Summary

The findings of this study show that TGA@CdTe QDs interact with the ECM of *Haematococcus pluvialis* microalgae cells. Evidence of an interaction between the ECM and TGA@CdTe QDs in the Raman spectrum of a unicellular microalga is obtained by surface-enhanced Raman spectroscopy: the Raman signal is increased by ~ 500% when using aggregated AuNPs. Changes between the Raman spectrum of HPM/AuNPs and HPM-QDs/AuNPs have been found and suggest the existence of interactions between the -COOH group of TGA@CdTe QDs with saccharides present in the ECM as well as possible damage to chloroplasts due to ROS. While for SHPM and SHPM-QDs no changes in the Raman spectra have been detected. Future endeavors will focus on the detection and isolation of sugars present in the ECM to analyze and validate these observations and the possible formation of QDs conjugates.

As a result of this research, it is proposed that TGA@CdTe QDs internalize into human oral epithelial cells by facilitated diffusion. This process is mediated by the interaction with the membrane proteins and it occurred within the first few minutes. Advanced imaging integrating confocal and SEM microscopy allowed to reveal the early interactions of TGA@CdTe QDs and AuNPs in whole OECs. Meanwhile, STEM-EDX confirmed adsorption of particles onto cell membranes, distribution into cytoplasm/cytoskeleton and achieving nuclear invasion with early signs of toxicity. Specific interactions occurring at molecular level have been identified by Raman spectroscopy. Our results showed characteristic SERS peaks corresponding to biomolecules present in the cilia elements and in the cytoskeleton. Characteristic Raman signals have been increased up to $\sim 10^4$ by using AuNPs. Cell damage due to TGA@CdTe QD cytotoxicity is observed and diminished by using BSA during the cell uptake process. Raman spectroscopy offers an alternative for rapid and non-invasive analysis of adsorption and interaction of engineered nanoparticles with cellular models. The chemical interactions between TGA@CdTe QD and AuNPs after being adsorbed and internalized by the cells is an important issue that should be studied in depth in the future. The findings of this research should be taken into

account for the analysis and design of functional nanoparticles intended for bio-applications to reduce or avoid cytotoxicity.

Chapter four

SERS-active Au/SiO₂ powder for tissue diagnosis

In this chapter the results obtained with the SERS activity of Au/SiO₂ powder and gold nanoparticles in colloidal solution are presented and analyzed. A brief description of the types of soft and hard tissues used in this research is exposed.

By breeding the tissues with Au/SiO₂ powder, several characteristic peaks frequently used for adenocarcinoma diagnosis in the range of the Amide III are successfully enhanced. The SERS activity of Au/SiO₂ is attributed to the properties of the silica powder structures to interact with tissue components, particularly their propensity to rehydrate in contact with the tissues promoting the formation of clusters of gold nanoparticles and also allowing the adsorption and interaction with biomolecules. Characterization by complementary techniques such as electron microscopy are also used to confirm the attachment of the samples to tissues and image their locations within the tissues. In addition, this material is also tested for dental tissue diagnosis and, as in the case of glandular tissue, characteristic Raman bands are successfully enhanced.

4.1. Au/SiO₂ clouds in powder for *ex vivo* breast adenocarcinoma diagnosis

4.1.1. Glandular breast tissue (GBT)

The breast tissues comprise mainly glandular tissues and supporting (stromal) tissues.¹⁵⁰ The glandular part of the breast includes the lobules and ducts that lead out to the nipple. The cells of the lobules are responsible for milk production. The support tissue of the breast includes fatty tissue and fibrous connective tissue that give the breast its size and shape.¹⁵¹

It has been reported that the primarily component of breast tissue is fat. Normal breast tissue contains both glandular and adipose tissues. Glandular tissue consists of ducts lined by epithelial cells and a supportive collagenous extracellular matrix. Adipose tissue is primarily composed of adipocytes (it corresponds to cells containing large amounts of cytoplasmic fat), although small quantities of extracellular matrix are present. Ducts represent only a small volume of the tissue.⁶⁰ Figure 27 shows a representative diagram of the different tissues of the breast.

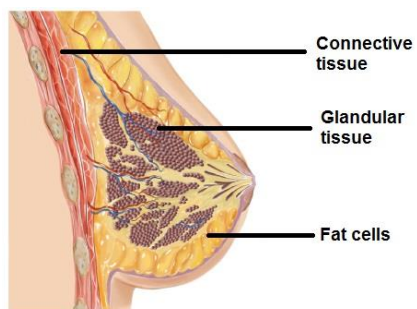


Figure 27. Representative diagram of the different tissues comprising the breast.

In figure 28 an image of the adenocarcinoma that is used for this work is shown, regions of abnormal cell growth are observed. Given the lack of directional cell structure it can be inferred that the image shows cancerous cells of a tumor.

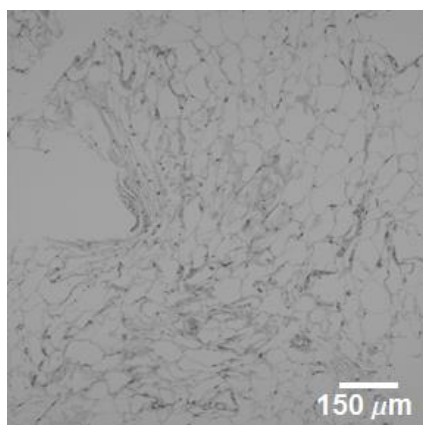


Figure 28. Cancerous GBT tumor cells.

Breast adenocarcinoma samples. Tissues were obtained from patients undergoing surgical breast biopsy mammoplasties and mastectomies. The samples have been routinely processed and examined by an experienced breast pathologist from the pathology department of the Instituto de Seguridad y Servicios Sociales de los Trabajadores del Estado (ISSSTE) in Guanajuato State (Mexico). Upon removal, the samples were fixed in formalin. Specimens have been rinsed in phosphate-buffered saline (PBS) before the Raman measurements to reduce the formalin fixation artifacts on the Raman spectra.¹⁵² Each sample was divided, and either incubated for one hour in naked AuNPs or breaded with Au/SiO₂ and incubated for

five minutes. A total of 150 spectra have been examined by using Raman spectroscopy: 70 normal and 80 malignant lesions diagnosed as adenocarcinoma.

Equipment and methods. FE-SEM was performed in a JEOL JSM-7800F microscope coupled with x-ray energy dispersive spectroscopy (EDS). The UV-Vis absorption spectra of colloidal AuNPs and Au/SiO₂ have been obtained by transmittance using an Agilent Technologies Cary Series UV-Vis-NIR spectrophotometer (Cary 5000). All measurements have been carried out under room temperature. XRD patterns have been obtained using a Bruker D2 Phaser with a Bragg-Brentano array. A Renishaw Raman System (Via Raman microscopy) with an objective lens of 20 X magnification and a spot size of 5 μm is used, the excitation laser was operated at 785 nm using a power of ~5 mW. The integration time for each Raman measurement is one second to avoid sample damage as reported by Kneipp et al.¹⁰⁷. For the Raman signal enhancement 0.1 mg of Au/SiO₂ powder has been spread on the surface of a wet tissue in an area of approximately 8 square millimeters and after an incubation time of five minutes the sample was ready for Raman spectroscopy measurements. By following this procedure, between 6 and 7 Au/SiO₂ clouds can be found in the irradiation spot. In the case of colloidal gold nanoparticles, the tissues have been incubated for one hour in 0.5 ml of AuNPs. Around 150 spectra of selected areas (~22500 μm²) of the tissue samples have been obtained. These areas were selected using tissue pathology criteria.¹⁵³ By averaging the spectra obtained for each type of sample the representative spectrum is found. Also different areas have been measured by duplicate on the same tissue sample to identify characteristic Raman signals and evaluate their reproducibility. The differences found in the Raman signal between points in the mapped areas; attributed to the natural irregularities of the tissue, are not noticeable when considering the overall averages.

4.1.2. SERS activity of AuSiO₂ powder in glandular breast tissue

To observe the distribution of gold in the tissue samples after they have been breaded with Au/SiO₂ or incubated with AuNPs, an EDS analysis is performed and the results obtained are shown in figure 29. Greater dispersion of gold nanoparticle cluster structures is observed for the Au/SiO₂ sample, while in the sample incubated with AuNPs the particles appear to be in bigger clusters, see figure 29 (a) and (b).

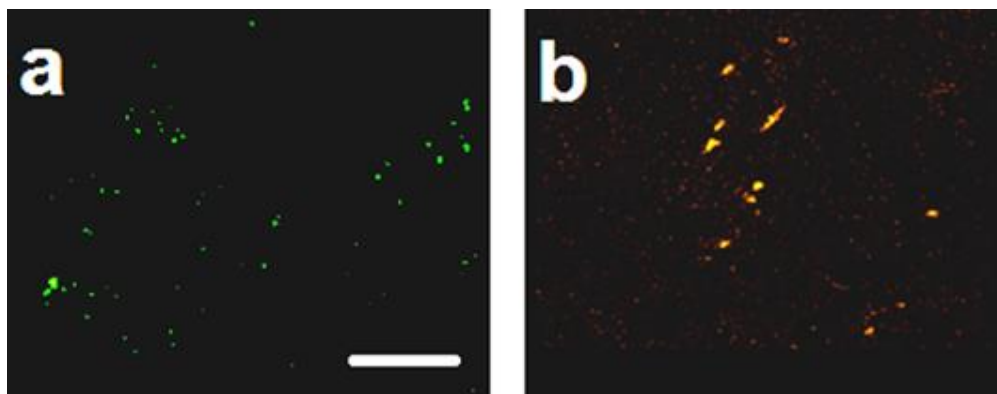


Figure 29. EDS analysis showing the distribution of gold in breast glandular tissue when using (a) Au/SiO₂ powder and (b) AuNPs. Scale bar is 2.5 μm.

Raman spectroscopy. Both Au/SiO₂ powder and AuNPs samples do not exhibit Raman peaks (figure 30 A, B (a) and (b) respectively). The Raman spectrum of normal and adenocarcinoma samples shows similar characteristics thus hindering their distinction (figure 30 A and B (c)). After incubation in AuNPs an enhancement in the signal is obtained, and some distinction between the two tissues is achieved. In normal tissue the peak at 1300 cm⁻¹ (fatty acids), marked with a black circle, continues to be the most intense in the region near to the Amide III allowing the presence of a subtle shift at 1260 cm⁻¹ (figure 30 A (d)). The ubiquitous presence of peaks at 1300 and 1440 cm⁻¹ in all spectra is one of the characteristics of normal glandular tissue. Spectral characteristics of adenocarcinoma reveal an enhancement in the peak at 1367 cm⁻¹ (tryptophan, α-helix), marked with a black circle (figure 30 A (d)). However, the strong presence of the peak at 1300 cm⁻¹ limits a possible diagnosis based solely on this spectrum. As a comparison the spectra obtained using Au/SiO₂ powder are shown in figure 30 A (e) for normal and figure 30 B (e) adenocarcinoma samples.

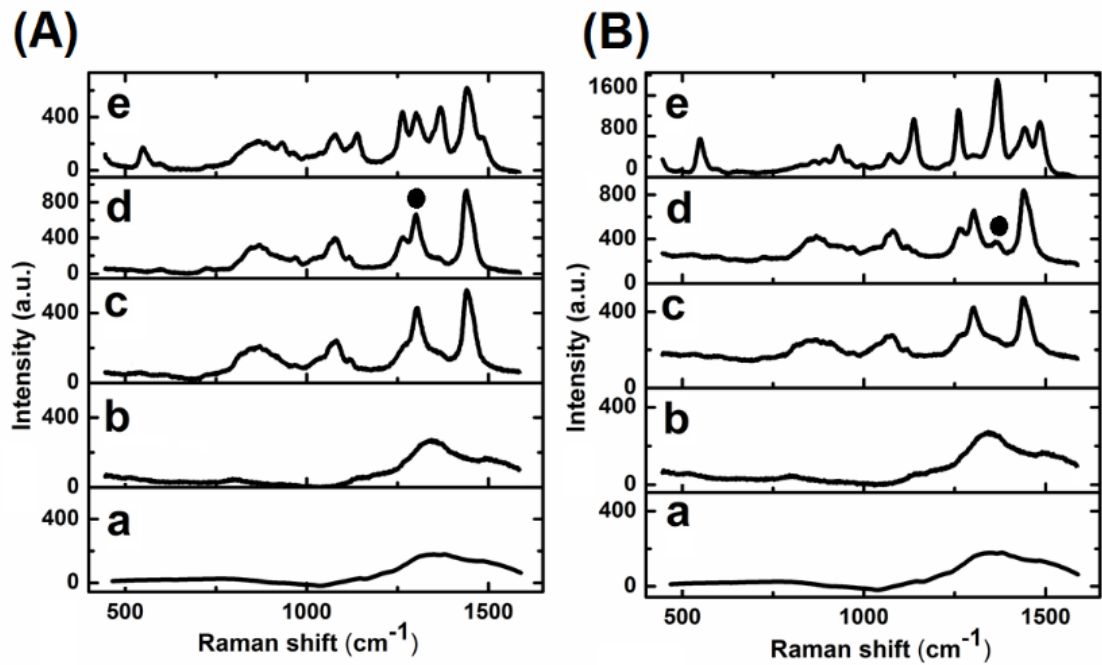


Figure 30. Raman signals of (A): (a) Au/SiO₂ powder and (b) AuNPs respectively. (c) Raman signal of normal tissue. SERS spectra obtained from normal tissue (d) incubated with AuNPs, (e) breaded with Au/SiO₂. (B): (a) and (b) show the Raman signals of Au/SiO₂ powder and AuNPs respectively. (c) Raman signal of adenocarcinoma. SERS spectra obtained from adenocarcinoma (d) incubated with AuNPs, (e) breaded with Au/SiO₂. The peaks at 1300 cm⁻¹ corresponding to fatty acids (A d) and 1367 cm⁻¹ assigned to proteins (B d) are marked with a black circle. All spectra have been acquired following 785 nm excitation.

The Raman signal obtained from normal glandular tissue by using Au/SiO₂ powder (figure 31 (a)) yields peaks at 548 (cholesterol), 886 (proteins), 932 (collagen/ Si-O⁻), 963 (lipids), 1076 (lipids in normal tissues), 1139 (fatty acids/ Si-O⁻), 1263 (Amide III protein band), 1300 (fatty acids), 1367 (tryptophan, α-helix), 1440 (CH₂ deformation of collagen and lipids), and 1482 cm⁻¹ (Amide II, formalin) and are in agreement with results reported recently.^{59, 60, 154} Some of the above peaks are rather absent or unclear in the spectra obtained using AuNPs (figure 6 A (d)). The Raman signals of adenocarcinoma are displayed in figure 31 (b). Au/SiO₂ breaded adenocarcinoma shows peaks at 548 (cholesterol), 863 (collagen), 892 (protein), 931(collagen/Si-O⁻), 958 (cholesterol/carotenoids), 988 (proteins), 1070 (proline-collagen), 1138 (fatty acids/ Si-O⁻), 1260 (Amide III), 1367 (tryptophan, α-helix), 1440 (CH₂ deformation of collagen and lipids) and 1484 cm⁻¹ (Amide II, formalin), see figure 31 (b). In this case the characteristic peak of at 1300 cm⁻¹ is practically absent and the protein peak at 1260 cm⁻¹ gains prominence with reference to the peak at 1440 cm⁻¹ attributed to fat.^{59, 154-156} For both tissues, the peaks around 1480 cm⁻¹ are assigned to formalin.^{59, 152}

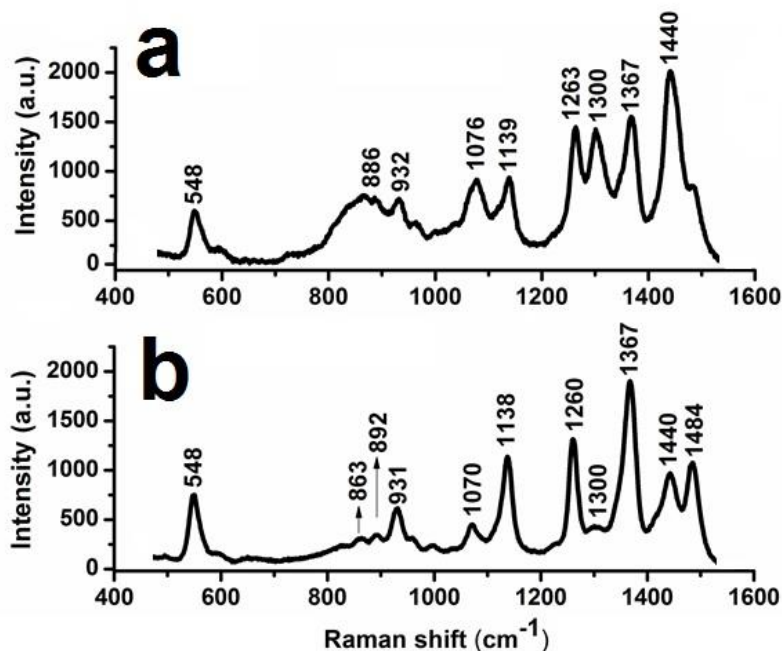


Figure 31. (a) Representative SERS spectra obtained from normal tissue breaded with Au/SiO₂ and (b) SERS spectra obtained from adenocarcinoma breaded with Au/SiO₂. All spectra have been acquired following 785 nm excitation.

Figure 32 (a) shows a plot of the integrated Raman signal for the tissues at different regions of the Raman spectrum when using naked AuNPs and Au/SiO₂. Figure 32 (b) shows the average values of the enhancement in the Raman signal vs. different regions of the spectrum when using naked AuNPs and Au/SiO₂. Each plot represents the average values from 50 spectra and error bars show the standard deviations. Using Au/SiO₂ resulted in a considerably higher enhancement, as shown in figure 32 (b). The peak of maximum SERS activity is observed in the middle region of the spectrum (1200~1370 cm⁻¹) when using Au/SiO₂.

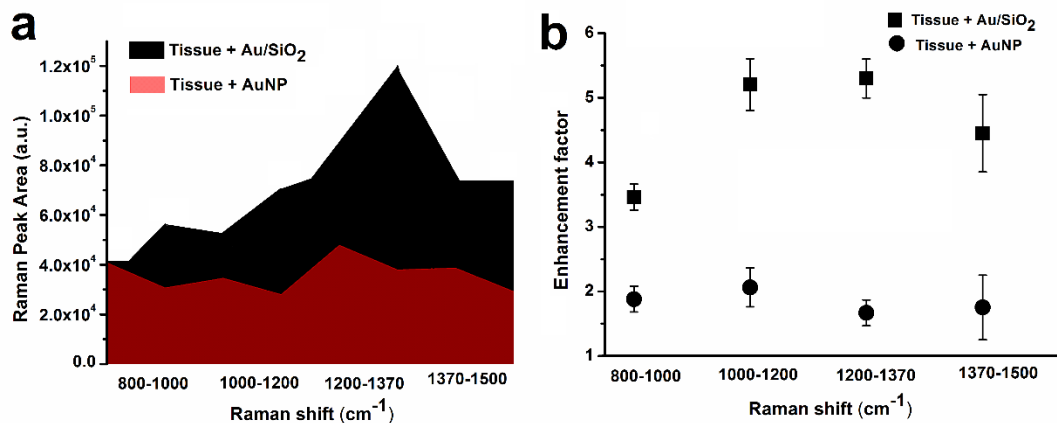


Figure 32. (a) A plot of the integrated Raman signal vs. different regions of the spectrum when using naked AuNPs and Au/SiO₂. (b) A plot of the averages of the enhancement in the Raman signal vs. different regions of the spectrum, for Au/SiO₂ and AuNPs. Error bars show the standard deviations. Each graph represents the average from 50 SERS spectra.

The Raman spectra have been acquired in the Amide III region, since it does not present interfering OH vibrations from H₂O and has been used as a direct qualitative indicator for conformational change in proteins.¹⁴⁵

Incubation times to obtain enhanced Raman signals by using gold colloidal nanoparticles have been reported in a range from half an hour to 24 hours.^{157, 158} As it has been reported, the incubation of cells and tissues with AuNPs may promote the formation of gold nano-clusters formed by individual nanoparticles of colloidal AuNPs and this results in an increase of the Raman signals due to the formation of hot spots (enhanced localized electromagnetic fields).^{64, 107, 159, 160} While the interaction of tissues with naked AuNPs resulted in an increase of the Raman signal intensity (see figure 44 A and B (c)), this overall increase is not useful for an effective diagnostic because of the similarities observed in the spectra of both types of samples. This is due to a lack of specific affinity between AuNPs and the biomolecules in the tissue.^{52, 107, 161}

When Au/SiO₂ powders have been used to enhance the Raman signal, the characteristic peaks of normal tissue and adenocarcinoma are clearly observed after an incubation of five minutes, allowing to distinguish between the tissues. Previously reported spectral features due to Si-O⁻ stretching bonds are found at 930 and 1140 cm⁻¹ in Au/SiO₂ breasted tissue samples and also low-frequency oligomeric features probably due to ring breathing modes are found at 500–550 cm⁻¹ in Au/SiO₂ breasted samples.¹⁵⁴ These enhancement of the Raman signal is the result of the electromagnetic field improvement

produced by the formation of cluster gold nano-structures during the process of hydration of the Au/SiO₂ clouds on the wet tissue and the adsorption of biomolecules into the SiO₂ matrix.
66

In particular, an improvement of the Raman signal is observed in the Amide III region of the spectrum. This indicates that proteins are adsorbed in the vicinity of the after mentioned hotspots. As has been widely reported proteins adsorb strongly into SiO₂ nanoparticles.^{159, 160} The surface chemistry of the Au/SiO₂ clouds (hydrophilic OH- presence) ensures the interaction with this protein molecules, specifically collagen in the case of glandular breast tissues. This is why the use of gold decorated SiO₂ nanoparticles has been widely applied to SERS studies with biomedical analysis purposes and it is especially useful in the case of breast cancer tissue where, among others, the expression of proteins plays an important role.^{162, 163} Moreover carboxylic groups of fatty acids may be covalently incorporated into silanol groups present on the surface of the Au/SiO₂ structures by Si-O-Si bonds.^{67, 99, 100, 154, 161, 164} A significant increase in the Raman signal is observed with the use of Au/SiO₂ powders, the enhancement turned out to be up to three times more sensitive compared to the use of naked AuNPs thereby demonstrating the importance of the SiO₂ structure for breast tissue studies. Differentiation between types of adenocarcinoma is not contemplated as part of this study. However, given the appropriate SERS activity of this material for breast tissue applications, this distinction could be studied in detail in a later work. Moreover calculations based on the previously presented concentrations indicate that in the spot-size surface of the objective lens a greater amount of gold nanoparticles can be found when using colloidal AuNPs (7×10^4 nanoparticles) than in the case of Au/SiO₂ powder (6×10^3 nanoparticles).^{96, 97} Therefore given the increase in Raman signal in the area of the Amide III the use of Au/SiO₂ powder is an effective way to improve interaction between the gold nanoparticles and the tissue, resulting in a considerable and useful enhancement of the Raman signal. These results confirm that Au/SiO₂ structures have the potential to be useful for future applications in tissue diagnosis. The methodology proposed here for the preparation of Au/SiO₂ breasted tissue is simple, reliable and does not require additional instrumentation than the Raman spectrometer.

4.2. Au/SiO₂ clouds in powder for dental caries diagnosis.

4.2.1 Dental tissue

Teeth are composed of four dental tissues. Enamel, dentin and cementum are hard tissues. The pulp, or the center of the tooth that contains nerves, blood vessels and connective tissue is a soft, or non-calcified, tissue.¹⁶⁵ Cementum is composed of a specialized calcified substance and covers the root of the tooth. The part of the periodontium that attaches the teeth to the alveolar bone by anchoring is the periodontal ligament. Cementum is excreted by cells called cementoblasts within the root of the tooth and is thickest at the root apex. These cementoblasts develop from undifferentiated mesenchymal cells in the connective tissue of the dental follicle or sac.¹⁶⁶ Unlike ameloblasts and odontoblasts, which leave no cellular bodies in their secreted products, during the later steps within the stage of apposition, many of the cementoblasts become entrapped by the cementum they produce, becoming cementocytes. Thus cementum is more similar to alveolar bone, with its osteoblasts becoming entrapped osteocytes.¹⁶⁷ This tissue is capable of repairing itself to a limited degree and is not resorbed under normal conditions. Slightly softer than dentin, cementum consists of about 45% to 50% inorganic material (hydroxyapatite) by weight and 50% to 55% organic matter and water by weight. The organic portion is composed primarily of collagen and proteoglycans. Cementum is avascular, receiving its nutrition through its own imbedded cells from the surrounding vascular periodontal ligament. It has the highest fluoride content of all mineralized tissue and is also permeable to a variety of materials. It is formed continuously throughout life because a new layer of cementum is deposited to keep the attachment intact as the superficial layer of cementum ages. On the root ends it surrounds the apical foramen and may extend slightly onto the inner wall of the pulp canal.¹⁶⁸

Dentin consists of microscopic channels, called dentinal tubules, which radiate outward through the dentin from the pulp to the exterior cementum or enamel border.¹⁶⁹ The tubules extend from the dentino-enamel junction in the crown area, or dentino-cemental junction in the root area, to the outer wall of the pulp. They have a diameter of 2.5 μm near the pulp, 1.2 μm in the middle of the dentin, and 0.9 μm at the dentino-enamel junction. Their density is 59,000 to 76,000 per square millimeter near the pulp, whereas the density is only half as much near the enamel. In addition, there are branching canalicular systems that connect to

each other. The size range of these is as follows, the major being 500-1000 μm in diameter, fine being 300-700 μm , and micro being less than 300 μm . The major branches are the terminal ends of the tubules. About every 1-2 μm , there are fine branches diverging from dentinal tubules at 45 degree angles.¹⁷⁰ The microtubules diverge at 90 degree angles. The dentinal tubules contain the cytoplasmic extensions of odontoblasts that once formed the dentin and maintain it. Because of dentinal tubules, dentin has a degree of permeability, which increases the sensation of pain and the rate of tooth decay. Dentinal hypersensitivity is due to changes in the dentinal fluids associated with the hydrodynamic mechanism processes. Dentin is a bone-like matrix that is also porous and yellow-hued material. It is made up of 70% inorganic materials (hydroxyapatite and some non-crystalline amorphous calcium phosphate), 20% organic materials (90% collagen type 1 and the remaining 10% includes dentine-specific proteins), and 10% water. It decays rapidly and is subject to severe cavities if not properly treated. Due to its elastic properties it is a good support for enamel. Its flexibility prevents the brittle enamel fracturing.¹⁷¹ The characteristic structure of the tooth and its main tissues are shown in figure 33.

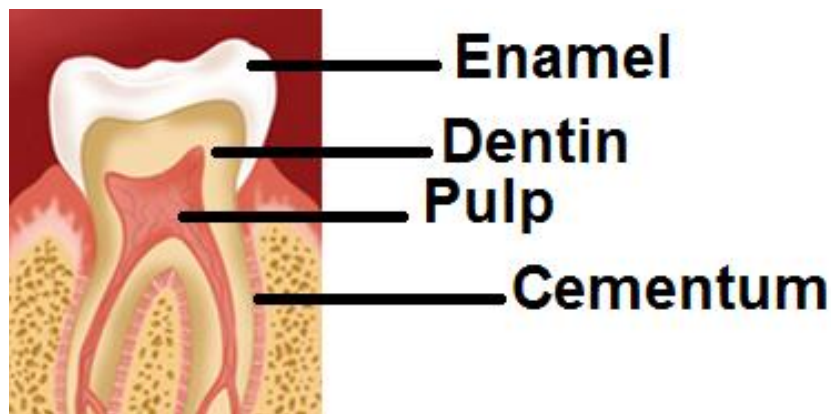


Figure 33. Characteristic structure of human tooth and its main tissues.

The first molars commonly experience increased pressure and wear compared to other tooth¹⁷² and therefore this teeth are more likely to suffer pulp damage culminating in an endodontic treatment. It is common that some years after having an endodontic treatment patients return to the dentist with pain and discomfort also and showing evidence of an infection in the gum area. One of the routine diagnostic techniques is to obtain an x-ray of the region. However the effectiveness of this technique is limited in addition to the risk linked to the use of ionizing radiation.¹⁷³ Dental caries processes are characterized by an increase in

the pathogenic microorganisms, in particular by the presence of *Streptococcus mutans*.¹⁷⁴ Despite the novel therapeutic strategies, oral diseases have elevated prevalence rates due to lack of effective early diagnosis techniques. It has been reported *S. mutans* plays an important role in the failure of root canal treatments, also the presence of *Enterococcus faecalis* within dentinal tubules after the treatment is a virulence factor. This is due to the ability of *E. faecalis* cells to maintain the capability to adhere to collagen in the tubules even after cleaning the roots canal with specialized products.¹⁷⁵

Raman spectroscopy can be implemented in a non-invasively manner to improve dental diagnostic techniques and avoid the use of ionizing radiation. The earliest carious changes involve chemical alterations, which are not normally visible on the tooth¹⁷⁶ but are expressed as changes in the biomolecules of the tissue. Raman spectroscopy is a technique which enables the identification of the energy levels of the molecules present in a sample. This energy levels are unique for individual molecules and can be associated with the vibrations of specific chemical bonds.^{50,51} The uses of Raman spectroscopy in biological measurements and applications are particularly oriented to clinical examinations related to detection of malignancies in tissues.⁵⁹ However for biological samples it is necessary to reduce the power of the laser sources, which results in a reduction of the signal used to extract information from the samples.⁶⁰

Sample preparation. Freshly extracted human first molars from volunteer subjects requiring the extractions as part of their dental treatment have been used for this study. The molars were studied immediately after extraction. Before Raman measurements a 60 seconds ultrasound rinse in deionized water was performed. The specimens were fractured and the regions with moderate decay at the external side of the root were selected. Also longitudinal and transversal sections of the dentinal tubules have been performed to analyze their interior.¹⁷⁷

Equipment and methods. Microphotographs of the selected tooth samples were acquired with a JEOL JSM-7800F microscope.

A total of 6 samples of dental tissue (DT) have been studied, three of them were breaded with AuSiO₂ powder and the other 3 were incubated colloidal naked AuNPs following the previously exposed protocol used for glandular tissue. Three regions

from each sample were selected randomly and measured by duplicate to identify characteristic Raman signals and evaluate their reproducibility. About 50 Raman spectra have been recorded for each sample, and averaged to obtain a representative spectrum of the sample. The differences found in the Raman signal between points in the mapped areas, attributed to the natural irregularities of the tissue, are not noticeable when considering the overall averages. A custom algorithm in Matlab® is made to obtain a mean spectrum that reflects the characteristics of the samples. The code searches the position of the peaks in each spectrum and outputs an average intensity for each peak present in the considered spectra. This way the representative average spectra shown in figure 47 were generated. The spectra have been collected using a Renishaw Raman System (inVia Raman Microscope) with a 20 X objective lens (N.A. 0.75); the excitation laser wavelength is 785 nm with a laser power of approximately 5mW on the entrance of the optical fiber. The integration time for each Raman measurement is 1s.¹⁰⁷

4.2.2. SERS activity of AuSiO₂ powder on dental tissue

Figure 34 shows SEM micrographs of the DT samples. The characteristic structure of the DT is characterized by the presence of dentinal tubules (see figure 34 (a) top view and (b) cross section). Figure 34 (c) and (d) show the DT after breeding with Au/SiO₂ and incubation AuNPs respectively.

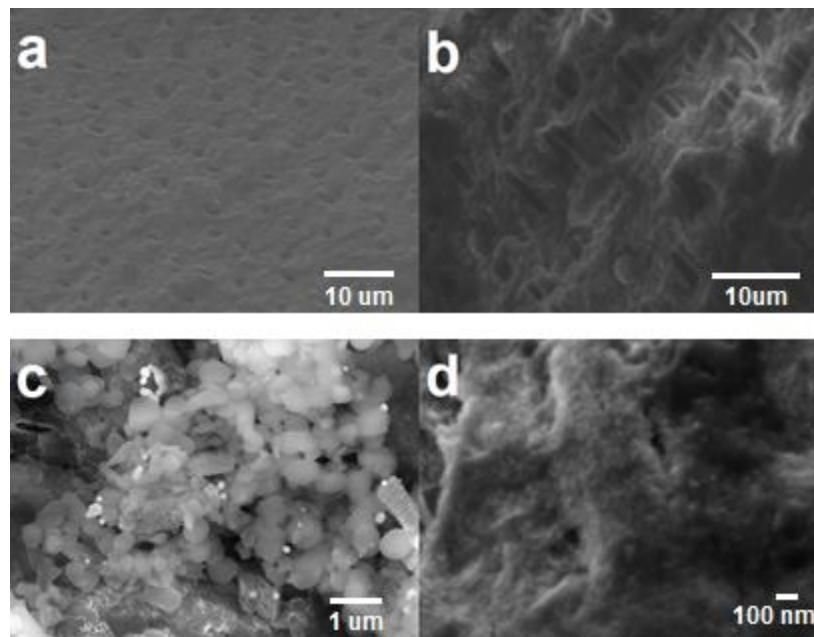


Figure 34. SEM micrographs of the samples of DT. (a) Top view of dental tubules. (b) Cross section of dental tubules. (c) DT breaded with Au/SiO₂. (d) DT incubated with AuNPs.

Figure 35 shows SERS spectra of DT. The typical bands of DT are located at 960 and 1452 cm⁻¹ and are assigned to PO₄³⁻ and C-H deformation respectively (see figure 35(a)). The PO₄³⁻ band is clearly observed in all spectra which is consistent with previous reports (see figure 35 a,b and c), while the C-H deformation band (collagen) appears clearly only in the SERS obtained using Au/SiO₂ (see figure 35 (c)); the spectrum shows also bands of amides and other features at 891 (saccharide band), 1001 (phenylalanine), 1041 (symmetric stretching vibration of PO₄³⁻), 1075 (carbonate band/ Si-O⁻), 1270 (Amide III), 1373 (saccharides), 1452 cm⁻¹ (proteins); which are related to pathological tissue history such as lesions produced by caries or previous dental treatments (see figure 35 (c)).^{59, 71, 154, 178, 179} The ratio of phosphate/carbonate peaks can be analyzed based on the relative integrated intensities to thereby obtain information on the status of the DT.⁷¹ As for the case of breast glandular tissue, DT incubation with AuNPs resulted in an increase in the Raman signal but it did not provide additional information. It was not possible to differentiate between the cementum and the dentin due to the biochemical similarity between the tissues.

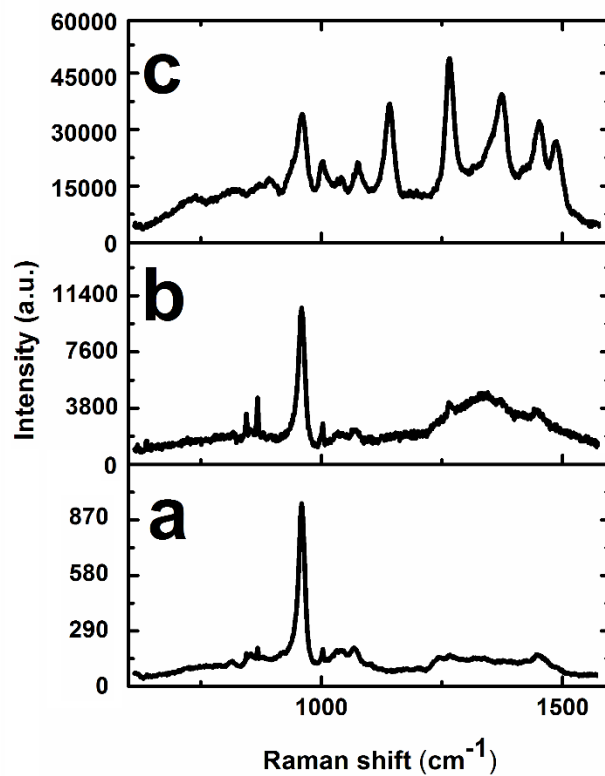


Figure 35. SERS spectra obtained of (a) DT, (b) after incubation with AuNPs and (c) breaded with Au/SiO₂. Following 785 nm excitation.

SERS activity of AuSiO₂ clouds in DT showed a similar behavior to that of adenocarcinoma. And generally for adenocarcinoma and dental tissues the peak of maximum SERS activity is observed in the middle region (1200~1370 cm^{-1}) when using Au/SiO₂. These results are also summarized in Table 1.

Table 1. Enhancement of the Raman signal obtained when using AuNPs and Au/SiO₂.

A	B	C	D	E	F	G
Spectral	Normal GBT		Cancerous GBT		Cementum DT	
region	AuNPs	Au/SiO₂	AuNPs	Au/SiO₂	AuNPs	Au/SiO₂
800-1000	1.6	1.3	1.9	3.5	1.1	0.6
100-1200	1.7	1.5	2.0	5.2	1.2	1.2
1200-1370	1.6	1.7	1.7	5.3	1.1	1.6
1370-1500	1.8	1.5	1.7	4.4	1.5	1.9

Summary

The dry Au/SiO₂ clouds are highly SERS-active when applied to wet tissue, allowing rapid distinction between normal glandular breast tissue and adenocarcinoma in the Amide III region of the Raman spectrum. The tendency of the Au/SiO₂ clouds to adhere to wet tissues promotes the formation of gold nanoparticle clusters in the nano-vicinity of the biomolecules located on the tissue surface. We can conclude that the enhancement of the Raman signal is attributed to the formation of the hotspots in the vicinity of adsorbed biomolecules. The excellent results demonstrate that Au/SiO₂ clouds have the potential to be applied to accurately classify *ex vivo* tissues and get a rapid diagnosis and discrimination between normal tissues and adenocarcinoma using low laser power and an integration time of one second. Moreover, this material also proved to be efficient for diagnosis of hard tissue as is dental tissue. Future endeavors will center on the toxicological analysis, the distinction between different adenocarcinomas and the possibility of using this technique for *in vivo* diagnosis, thereby reducing the number of excisional biopsies or the use of techniques involving ionizing radiation.

Chapter five

Conclusions and future work

A stable and repeatable synthesis of thioglycolic acid capped CdTe quantum dots by a wet chemical synthesis for biomedical applications is accomplished. It is noteworthy that the as-prepared QDs showed such stability that even one year after having been prepared the good luminescent properties are still present and require only simple instructions for storage at room temperature and moderate light. The wavelength of emission proved to be easily tunable by lengthening the time of reflux in the synthesis after the reaction occurred.

Similarly, the synthesis of naked anisotropic gold nanoparticles is simple and stable, however in this case there is no control over the proportion of each crystal structure. These ratios depend on the thermodynamic events during the synthesis and their study is a topic of current interest. However the same structures are present in all synthesis repetitions and each time they prove to be useful to obtain a non-selective SERS as predicted by Kneipp and co-workers.¹⁰⁷

Different responses are obtained for the study of the interaction of TGA@CdTe QD with plant and human cells. For the case of the microalgae cells, the findings of this study show that TGA@CdTe QDs interact with the ECM of *Haematococcus pluvialis* microalgae cells after 5 minutes of incubation and no internalization due to QD absorption is observed. Evidence of this interaction between the ECM and TGA@CdTe QDs in the Raman spectrum of a unicellular microalga is obtained by surface-enhanced Raman spectroscopy, the Raman signal is increased by ~ 500% when using the aggregated AuNPs. Changes between in the Raman spectrum of HPM/AuNPs and HPM-QDs/AuNPs are found and suggest the existence of interactions between the -COOH group of TGA@CdTe QDs with saccharides present in the ECM as well as possible damage to chloroplasts due to ROS. While for SHPM and SHPM-QDs no changes in the Raman spectra are detected.

While for the case of human cells this study showed that TGA@CdTe QDs internalize into fresh oral epithelial cells probably by facilitated diffusion. This process is mediated by the interaction with glycoproteins and membrane proteins and

occurs in a three-minute interval. Advanced imaging allowed to reveal the early interactions of TGA@CdTe QDs and AuNPs in whole OECs. Meanwhile, STEM-EDX confirmed adsorption of particles onto cell membranes, distribution into cytoplasm/cytoskeleton and in specific case achieving nuclear invasion with early signs of membrane damage. Specific interactions occurring at molecular level are for the first time identified by Raman spectroscopy corresponding to changes in biomolecules present in the cilia elements and in the tonofilaments. Characteristic Raman signals of the cells are increased up to 10^4 by using AuNPs. This information should be taken into account for the analysis and design of functional nanocrystals intended for *in vivo* applications.

In both cellular types, Raman spectroscopy offers an alternative for rapid and non-invasive analysis of adsorption and interaction of engineered nanoparticles with cellular models.

An innovative, repeatable and facile fabrication of Au/SiO₂ powder has been developed. It has been shown that the Au/SiO₂ structures are SERS-active to distinguish between normal glandular breast tissue and adenocarcinoma and to obtain characteristic Raman shifts from DT which could be useful to know the status of the tooth. The enhancement of the Raman signal is attributed to the increase of the hotspot because of the effective interactions of the Au/SiO₂ powder due to the interactions between the silica and biomolecules located on the tissue surface and its tendency to adhere to wet tissues. The excellent results demonstrate that Au/SiO₂ structures have the potential to be applied to accurately classify tissues and get a rapid diagnosis and discrimination between normal and cancerous tissues. Future endeavors will center on the possibility of using this technique for *in vivo* diagnosis, thereby reducing the number of excisional biopsies or the use of techniques involving ionizing radiation for diagnosis.

Future work includes improved characterization of the TGA@CdTe QD structure such as the confirmation of the presence of a core shell structure and a fine characterization of the temporal stability of the quantum dot in water. Moreover, various experiments varying the thiol capping agent could be made and their functionalization to certain cellular components.

In the same way, the affinity of the gold nanoparticles to certain cellular components could be improved thus improving the SERS signal to study specific interactions.

Uptake process for different cell types is specific and remains an open issue. Thus, determining cell damage and mechanisms of interaction between nanomaterials such as QDs and cells is relevant for environmental impact and safe biomedical applications. Also future endeavours will focus on the detection and isolation of sugars present in the ECM to analyse and validate these observations and the possible formation of QDs conjugates.

While Au/SiO₂ powders proved to be effective for tissue diagnosis, an improvement in the stability and uniformity during the synthesis process could be done in order to improve the result. Likewise, a more specific characterization of the interaction of biomolecules with the powders could be studied.

Appendix A

Focused ultrasound system for biomedical applications

Sonoporation

It is now known that there are physical methods for varying the concentration and rate of uptake of nanoparticles into cells. One of such methods is known as sonoporation and involves the use of an ultrasound source. Studies on ultrasound induced cell permeabilization introduced the term “sonoporation” to describe the temporal cell membrane openings that can arise after ultrasound exposure. As has been reported, the use of microbubbles amplifies the biophysical effects of ultrasound. Such microbubbles are gas-filled structures stabilized by a lipid, protein or polymer shell. Since these microbubbles are filled with gas they consist of a compressible core and therefore respond to the ultrasound pressure waves. The alternate growing and shrinking is known as cavitation and can be divided into stable cavitation, that mainly occurs at lower ultrasound intensities and inertial cavitation, occurring at higher ultrasound intensities that leads to microbubble implosion which results in abrupt biophysical effects.¹⁸⁰

The three main types of ultrasound application are: low intensity ultrasound that leads to stable cavitation of microbubbles, high intensity ultrasound, leads to inertial cavitation with bubble collapse, and ultrasound application in the absence of microbubbles.¹⁸¹ The interaction of ultrasound with tissue can induce mechanical effects, chemical effects and thermal effects, depending on the ultrasound intensity, which in turn can lead to several bio-effects. In the case of low intensity only mechanical effects are observed. However, any temperature increase during the experiments, changes the physicochemical state of the cell membranes and could render them more sensitive to membrane deformation. Recent literature suggests that endocytosis might be involved as well in ultrasound triggered drug delivery, this is important since the cells of interest in this study are epithelial cells known for their endocytic uptake processes.¹⁸²

At low ultrasound intensities, two mechanisms have been proposed to contribute to the uptake of cell-impermeable molecules: one is the formation of small pores and the second is endocytosis. The involvement of endocytosis is more extensive for larger molecules, and

pore formation is the main mechanism for smaller dextrans. Ultrasound-induced mechanical stress and chemical effects have been reported to be responsible for this pore formation. By ultrafast real-time transmission microscopy techniques, the mechanisms of membrane poration due to an interaction between microbubbles and the cell membranes have been observed.¹⁸³

Pore formation is attributed to the cavitation of microbubbles closely located to the cell membrane, gently pushing and pulling the cell membrane and disturbing the cellular membrane as a result of mechanical stress. Therefore, pore formation correlates with the oscillation amplitude of the microbubbles. Experiments performed with single cells indicate that a direct contact between microbubble and cell membrane is required to induce pore formation by stable cavitation.¹⁸⁴

Three main routes of endocytosis are involved in the ultrasound-mediated uptake: clathrin-mediated endocytosis, caveolae-mediated endocytosis and macropinocytosis, where clathrin-dependent mechanisms are predominant.¹⁸⁵

The mechanisms which are responsible for the ultrasound-induced endocytosis have been the subject of debate and have not been completely elucidated up till now. A first possible explanation is that microstreamings or acoustic streaming induces endocytosis, and shear stress can stimulate the endocytic uptake of fluid-phase markers in endothelial cells. Ultrasound-induced mechanical forces can lead to plasma membrane deformation which is accompanied by cytoskeletal rearrangements as a result of changes in cell membrane tension.¹⁸⁶

Ultrasound or oscillating microbubbles can induce cytoskeletal rearrangements, these processes add plasma membrane (exocytosis) or remove (endocytosis) and hence restore plasma membrane tension.¹⁸⁷

Exocytosis lowers the membrane tension in order to facilitate spontaneous resealing and the intracellular vesicles recruited by exocytosis fuse with each other and form a giant patch that subsequently fuses with the damaged plasma membrane and reseals the membrane disruption indicating that exocytosis may also be triggered by ultrasound, creating cell membrane disruptions.¹⁸⁸

Thus, ultrasound enhanced endocytosis may be a consequence of exocytosis. By low intensity ultrasound, the endocytic uptake of nanoparticles could be stimulated, while short

but intense ultrasound pulses induces pore formation and the direct cytoplasmic uptake of drugs which are sensitive to lysosomal degradation. Ultrasound intensities may be adapted to create pore sizes which correlate with the particle size. And small molecules are able to diffuse passively through small pores created by low intensity ultrasound treatment.¹⁸⁹

In this appendix, the description of the automatic system designed to excite biological samples with focused ultrasound is presented. Preliminary data on the response of the cells to a low power ultrasound beam for are shown.

A.1. Experimental setup

The focused ultrasound system is intended to work in cross-transmission mode, where the plane of interest in the sample is perpendicular to the propagation of the ultrasound beam. Thus it is possible to estimate the value of the attenuation of the field produced by the presence of a sample and the speed of sound in the sample by considering an analysis based on the flight time. The experimental setup proposed for the automated focused ultrasound system is shown in figure A1. The system consists of a tank filled with deionized and partially degassed water. Within the tank, the sample and transducer are placed in positions shown in figure A1.

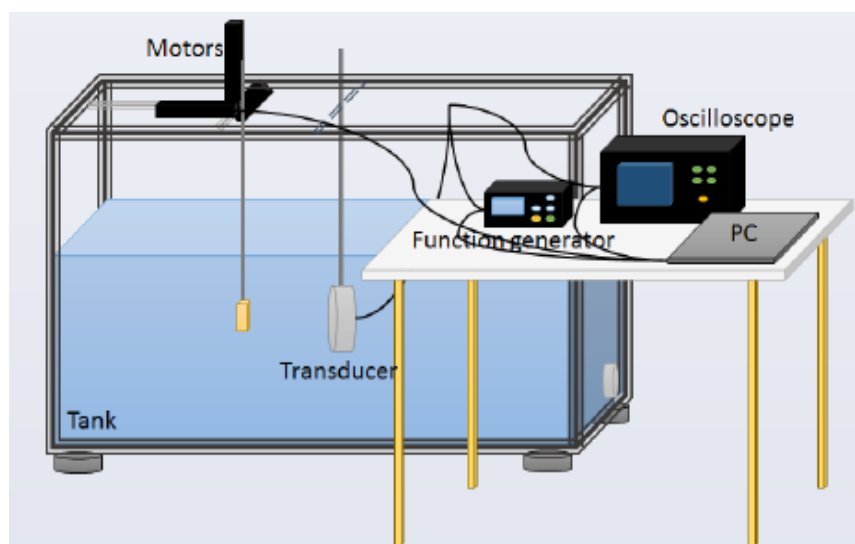


Figure A1. Experimental setup proposed for automated focused ultrasound system.

The transducer is mounted on a movement system which is controlled manually and it has three directions of movement. The movement system for the sample is controlled by computer by a LabView® program, as in the case of the transducer it has movement in three independent axes. The description of this system is explained below. The sample, which is mounted in a special holder is placed in front of the transducer so that the front is parallel to the transducer surface. The water inside the tank is heated at 37° Celsius, to emulate one of the conditions of the *in vivo* situation. To warm the water, recirculation heaters are placed as far as possible from the sample to avoid disturbances due to the movement of water. Given the current low power of the transducer it is not necessary to place absorbers in the tank walls. No internal reflections or possible interference effects that might affect the measurements are observed.

An ultrasound transducer made from a piezoelectric material and lead titanium zirconated (PZT) is used as transmitter and signal receiver. The geometry of the transducer is a split sphere with a focal length of ~7 cm (a curvature corresponding to a sphere of diameter 15 cm) and a diameter of 5 cm. The transducer has a center frequency of 1 MHz and is purchased from Precision Acoustics®. Data acquisition consists of two steps, the first is the alignment ensuring that the acoustic wave axis is perpendicular to the sample, and the second is the excitation of the sample. The transducer generates an acoustic wave propagating in the water. Where the focus has the shape of an ellipse of approximately 1.5 cm long and 1.5 mm radius. A schematic representation is shown in figure A2.

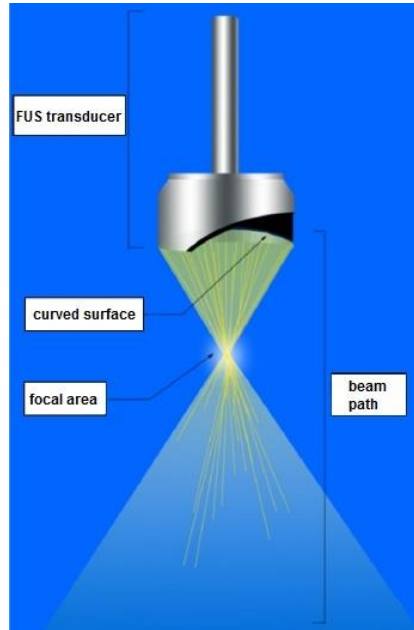


Figure A2. Ultrasound beam path. (Adapted from ref. ⁴)

In a cross-sectional view of the cone (see figure A2) the field propagates in circularly symmetric concentric rings, with maximum intensity in the central ring. Measurements could be obtained in different planes to characterize the ultrasound propagation. The sample is placed in the focal plane of the transducer, which is where the delivered power is concentrated. At the boundary between two media with different acoustic impedances, as in this case the border between water and the sample, reflection and refraction occurs. On smooth surfaces reflections are specular while on rough surfaces reflections are diffuse. Specular reflection is the basis of the ultrasound image, which is formed from the echo. Below, it is explained how the principle of reflection is used as an alignment method for the system. When a plane wave is incident on a flat surface, a reflected and a transmitted wave are generated. When the incidence is perpendicular, only longitudinal waves are present. According to the law of Snell-Descartes, the reflection angle θ_1 equals the angle of incidence of the wave and the transmitted wave is refracted at an angle θ_2 according to the equation 1.

$$\frac{\sin\theta_2}{c_2} = \frac{\sin\theta_1}{c_1} \quad (1)$$

Where c_1 and c_2 are the speeds of sound of the first and second medium. At normal incidence ($\theta_1 = 0$), the reflected and transmitted waves are also normal to the incidence surface. The ratio between the amplitude of the incident and reflected wave (sound pressure ratio) is called reflection coefficient (r). The ratio of the amplitude of the incident wave and the transmitted is called transmission coefficient (t).

When the acoustic axis and the plane of incidence are not perpendicular, transverse waves are also generated and a more complicated analysis is required. To simplify the analysis, we will restrict ourselves to the case of normal incidence, so a fundamental part of the experimental setup will ensure that the ultrasound waves impinge perpendicularly to the sample. It is also necessary to ensure that the acoustic wave is incident at the same phase in all the sample plane, the sample plane should be parallel to the focal plane. A first criterion of alignment corresponds to align the transducer with the framework of the sample support, thus ensuring normal incidence. The transducer is mounted in a manual system described above, and once it is in the desired position to start the measurements it should not be moved.

The optical axis of the transducer can be aligned with the bottom of the tank using a level as shown in figure A3. In the same way, the sample holder should be aligned with the focal plane.

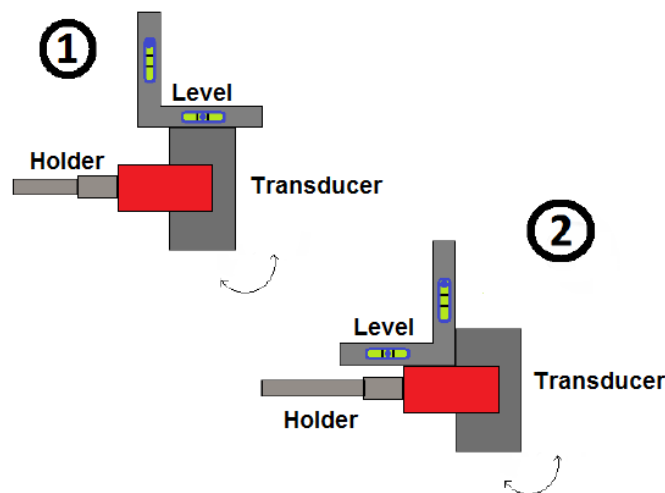


Figure A3. Transducer alignment. (Adapted from ref. ⁴)

To find the focal plane, sine-wave pulses of 30 cycles at 1000 KHz are programmed into a function generator and the signal is sent to the transducer; the signal and its echo are observed on the oscilloscope.

The broader pulse corresponds to the excitation signal and after a delay, the echo of the signal is observed. This scheme is shown in figure A4.

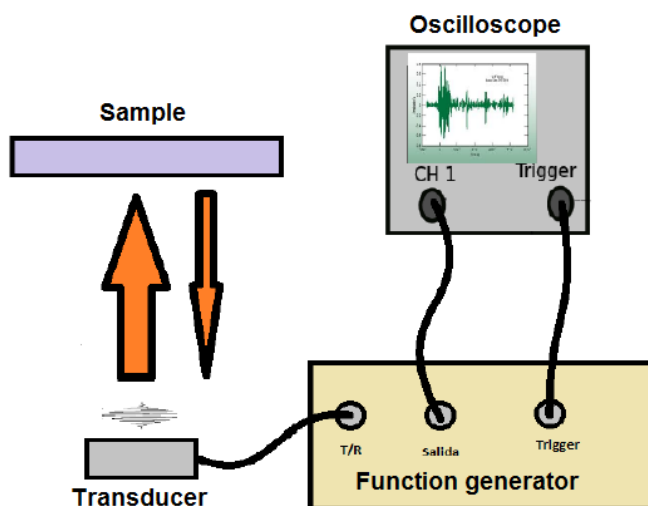


Figure A4. Eco-mode transducer configuration. (Adapted from ref. ⁴)

There are two criteria by which we can know when the sample holder is at the focal length. The first is to know the focal distance and consider the value of the speed of sound for the temperature of the water in the system. Then calculate the time it will take the signal to go and return and calculate the location of the focal plane. The other approach is to observe the amplitude of the echo signal on the oscilloscope: when the amplitude of the reflected signal is maximum, the sample is at the focal length. During the experiments both criteria are considered. Once the transducer and the frame are aligned the system is ready to begin the treatment.

The sample which is used to test the system consisted of a square flat bag (2x2 cm) made with Parafilm® tape containing about 1 ml of a suspension of human oral epithelial cells dispersed in saline solution and, depending on the sample, colloidal nanoparticles. During the treatment, the sample moves on the focal plane following the path shown in figure A5. In this configuration different regions of the sample are excited.

In figure A6 a signal of decreasing intensity was programmed and a decrease in the intensity of the echo signal is shown.

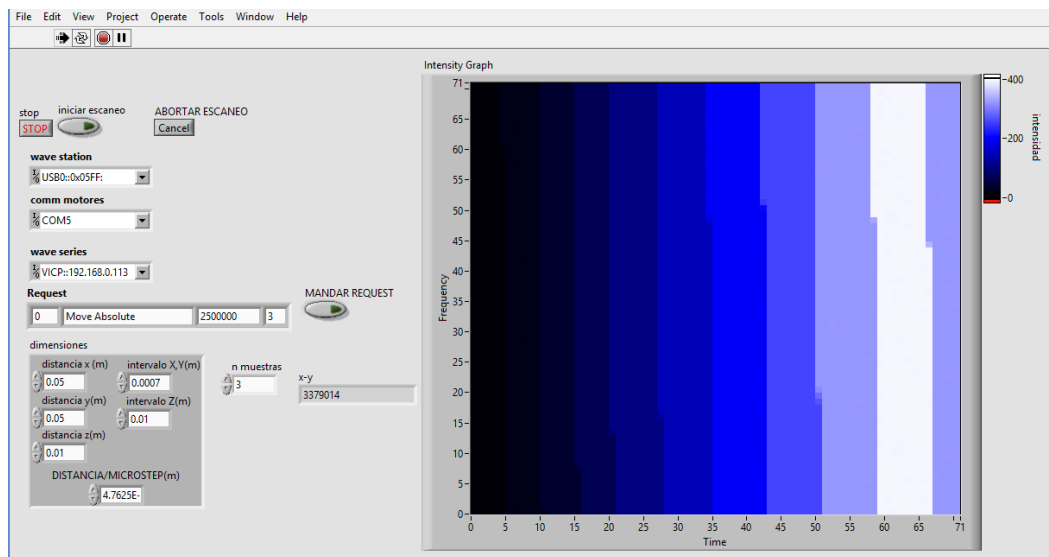


Figure A6. Graphical user interface (GUI) for the ultrasound system.

The following experiment is to obtain an image of the sample support by using the amplitude of the reflected echo signal as a pixel value. The image obtained is shown in figure A7. This system allows the acquisition of ultrasound imaging of solid pieces. The resolution of the system is defined by the focal area (0.065 cm^2) and the Nyquist–Shannon sampling theorem which states that accurate reconstruction of a periodic continuous baseband signal is mathematically possible if the signal is band-limited and the sampling rate is more than twice its bandwidth.

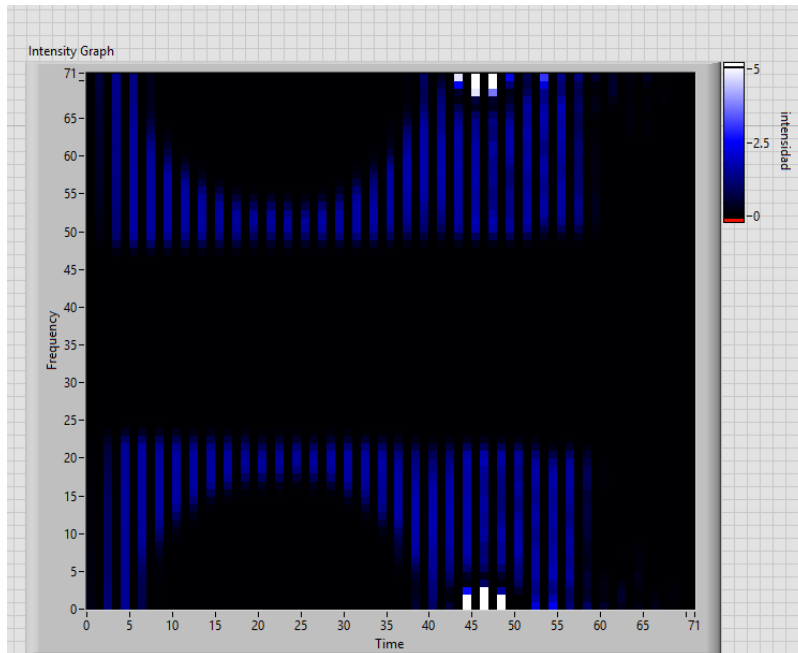


Figure A7. Echo image of the sample support by using the amplitude of the reflected signal as a pixel value.

The next step is the characterization of the Parafilm bag containing the samples. For this the echo signal received by the transducer is analyzed for single and double Parafilm layers. Figure A8 (a) Shows that the echo signal, as received after passing through one layer of Parafilm, has both a temporary delay as a slight decrease in the amplitude of about 0.25 V. In figure A8 (b) the original signal and its echo are displayed and similar behavior is shown. In the case of the cells experiments, the power delivered at the sample is: $P_c = P_0 - P_p$, where P_0 is the power at the focal plane in the absence of sample and P_p is the power absorbed by the Parafilm layer. Using the data provided by the manufacturer of the transducer, an input voltage of 20 V corresponds to a power of ~615 watts in the focus area. This low power is minimally affected by the presence of Parafilm (~38 watts). Therefore, the Parafilm is a good material to contain the samples without diminishing power in the focus area.

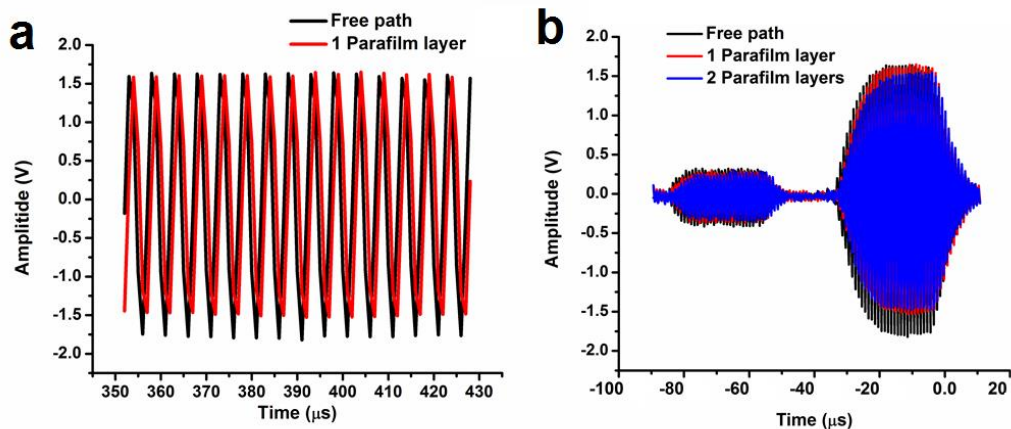


Figure A8. Signal attenuation in the focal plane due to the presence of Parafilm. (a) Reduction in amplitude of the echo signal, a close up. (b) The original signal and its echo.

A.3. SEM and EDS analysis of sonicated epithelial cells.

The duration of the ultrasound treatment varies is 60 minutes. In order to ensure that all cells receive treatment for at least 3 seconds. A test was performed to examine the state of cells after a one-hour incubation in TGA@CdTe QDs and AuNPs. The incubation protocol is identical to those presented in the previous chapter except for the incubation period and the fixation method for SEM microscopy. At the end of the procedure, from each of the 4 tubes 25 μl of the material are taken and placed on silicon wafers^{104, 105}. The wafers are placed in a preheated oven at 100° C for three minutes. The samples are cooled at room temperature and then analyzed. Thus to observe the integrity of the fixed OECs, fluorescence images are acquired and the presence of nanoparticles is studied by electron microscopy. Figure A9 (a) shows a fixed OEC incubated with BSA and then in TGA@CdTe QDs, excited at 470-490 nm, and the emission is collected at 520 nm. In the figure is possible to observe most aspects of the cell morphology remain after an incubation period of one hour and that fixation of OEC did also not alter their morphology, only slight changes in the intensity of luminescence (~10%). FSEM images of OECs are displayed in figure A9 (b) and (c). Figure A9(b) shows a fixed OEC incubated with AuNPs and figure A9 (c) shows a fixed OEC incubated with AuNPs-BSA- QDs. Disperse AuNPs (50 nm) are observed in OECs as shown in figure A9 (d).

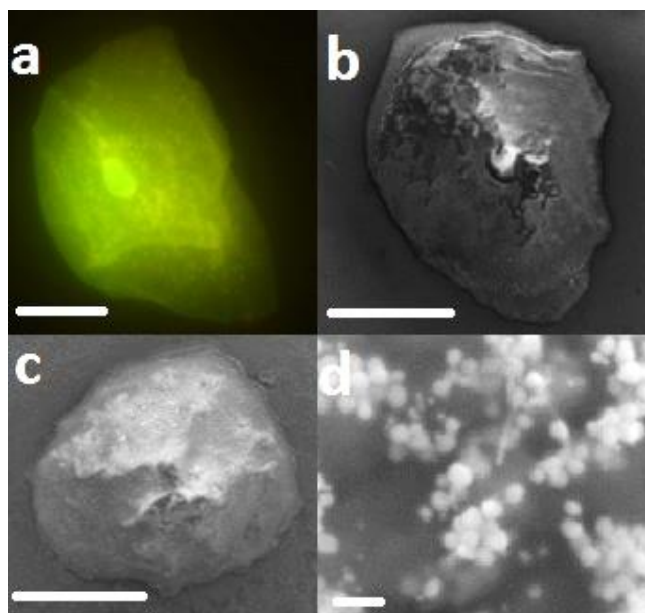


Figure A9. (a) Fixed OEC with QDs1 excited at 470-490 nm, the emission is collected at 520nm. (b), (c) FSEM images of OECs. (b) OEC incubated with AuNPs. (c) OEC incubated with AuNPs, BSA and TGA-CdTe QDs. Scale bar in (a), (b), (c) represents 20 μm . (d) AuNPs in OEC, scale bar corresponds to 100 nm.

Table A1 shows the chemical analysis found for: cadmium (Cd), tellurium (Te) and gold (Au) together with the elements naturally present in OEC, carbon (C), oxygen (O), nitrogen (N), phosphorus (P) and sulfur (S), obtained by EDS punctual analysis for the different OECs samples. The resulting amount of gold in OEC-AuNPs is 24% whereas for OEC-AuNPs is 2.3 %. The OEC-AuNPs-BSA-QD sample is the only one where Te (1.0%) is present and with the higher presence of Cd (4.4%). Otherwise if there is no presence of AuNPs, the tellurium does not appear in the OEC, see table 1. According to previous reports and our experimental results presented above when AuNPs are in the vicinity of the QD and the LSRP of AuNPs coincides with the peak emission of QD energy transfer phenomena occurs among both nanoparticles^{90, 190, 191}.

Table A1. Averages of WPV obtained by EDS punctual analysis in OEC-AuNPs, OEC-BSA-QD, OEC-AuNPs-BSA-QD samples of: gold (Au), cadmium (Cd), telluride (Te), carbon (C), oxygen (O), nitrogen (N), phosphorus (P) and sulfur (S). σ represents the error in Wt% ($\pm \sigma$).

Sample	Cd (Wt%)	σ	Te (Wt%)	σ	Au (Wt%)	σ	C (Wt%)	σ	O (Wt%)	σ	N (Wt%)	σ	P (Wt%)	σ	S (Wt%)	σ
OEC	0.0	--	0.0	--	0.0	--	51.7	0.1	20.8	0.6	22.3	1.1	1.2	0.2	2.9	0.2
OEC-AuNPs	0.0	--	0.0	--	21.7	1.1	47.2	0.6	14.2	0.4	14.3	0.9	0.3	0.1	1.6	0.2
OEC-AuNPs	0.0	--	0.0	--	1.2	0.6	55.0	0.6	22.4	0.4	18.5	0.7	0.6	0.1	2.3	0.1
OEC-BSA-QD	3.8	0.9	0.0	--	0.0	--	51.8	1.5	22.2	0.9	18.5	1.8	0.1	0.0	2.3	0.3
OEC-AuNPs-BSA-QD	4.4	0.1	1.0	0.2	0.7	0.3	51.2	0.3	21.8	0.2	15.0	0.4	0.6	0.0	3.7	0.1

Figure A10 shows an example of the mappings that are performed on the cells and one of the obtained spectra.

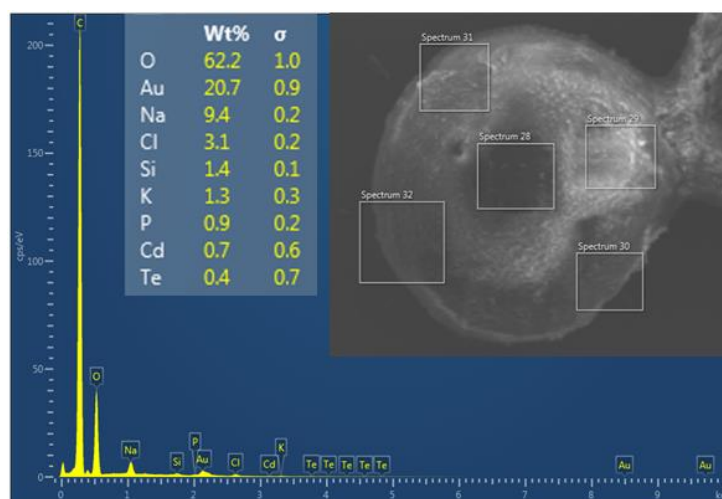


Figure A10. EDS elemental analysis performed on an OEC-BSA-QDs-AuNPs sample.

However, cellular metabolism tests should be performed taking into account that the rate of internalization of nanoparticles is time and size dependent. The possible effects of energy transfer between the TGA@CdTe QDs and AuNPs within the cells is a phenomenon that has not been reported or studied in depth.

Ultrasound experiments consist of incubating the cells for one hour with TGA@CdTe QDs or AuNPs while a scan is performed at the focal plane of the ultrasound. As a control an identical sample is placed away from the focal plane, at the bottom of the tank. About 20 repetitions of the experiment are performed. All samples of cells, both which received ultrasound treatment (figure A11 (b) and (d)) as well as the control samples (figure A11 (a) and (c)), retained characteristic cell structure and showed the presence of nanoparticles in the EDS mappings.

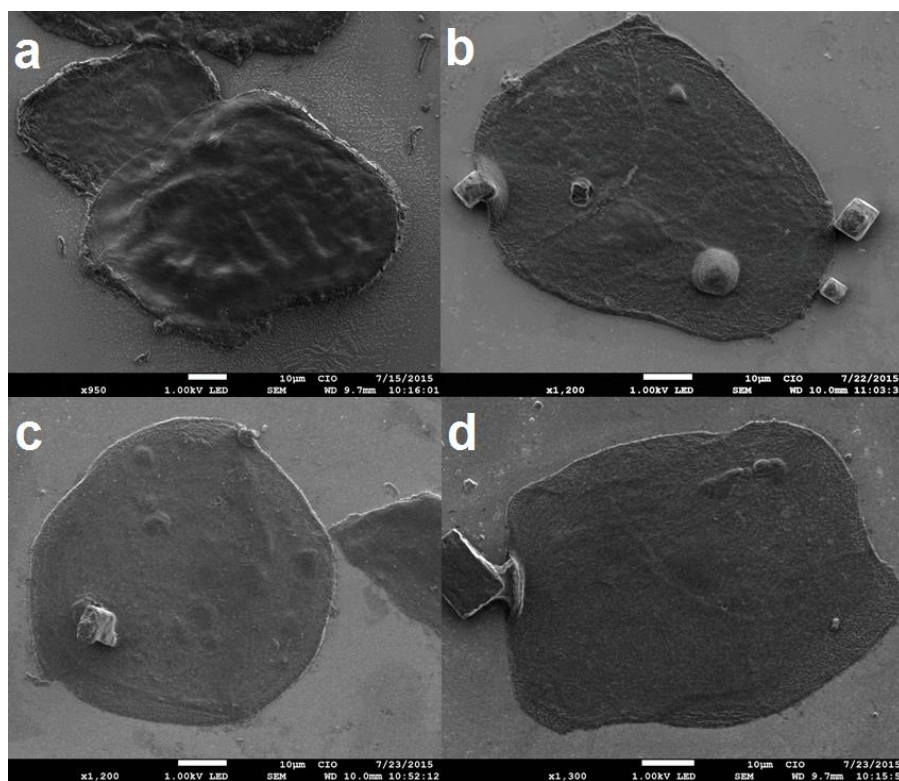


Figure A11. SEM images of cells incubated for one hour with (a) BSA-QDs, (b) BSA-QDs in the ultrasound focal plane, (c) BSA-AuNPs, (d) BSA-AuNPs the ultrasound focal plane.

Both ultrasound treated (figure A12 (a)) and untreated (figure A12 (b)) samples incubated with TGA@CdTe QDs are also analyzed under the fluorescence microscope showing similar characteristics.

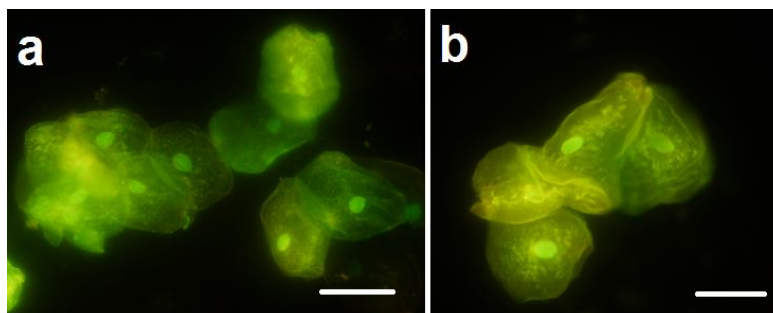


Figure A12. Fluorescence images of cells incubated for one hour with (a) BSA-QDs in the ultrasound focal plane, (b) BSA-QDs.

In the case of cells incubated only with quantum dots, by averaging the obtained punctual mappings an increase in the abundance of the elements related to TGA@CdTe QDs is obtained, see figure A13. However, this effect is only observed when considering an average and for individual measurements the standard deviation is high. Although this result may indicate a trend, repetitions of the experiment considering variations in power could confirm these results.

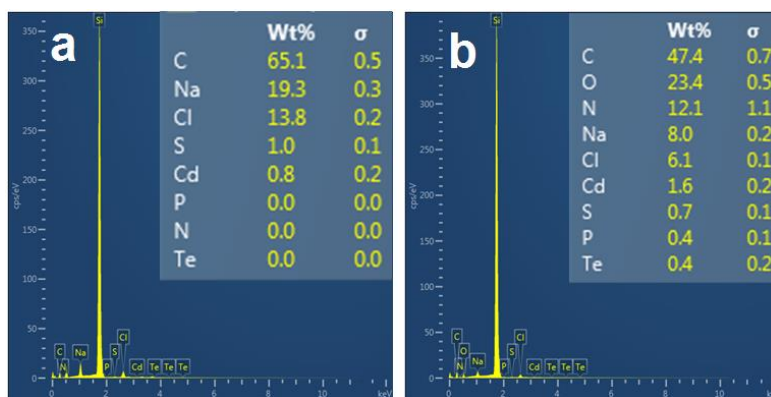


Figure A13. EDS elemental analysis of cells incubated for one hour with (a) BSA-QDs, (b) BSA-QDs at the ultrasound focal plane.

Similar behavior is observed in the case of the cells incubated with AuNPs, see figure A14. However, in this case the standard deviation is greater. This effect must be related to the larger size of the nanoparticle which causes that more power is needed to produce the sonoporation.

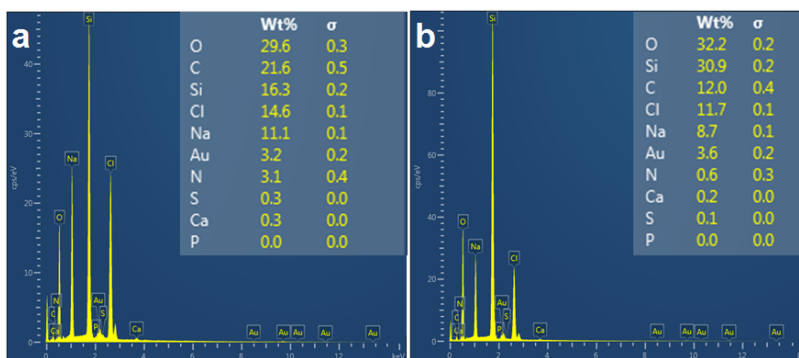


Figure A14. EDS elemental analysis of cells incubated for one hour with (a) BSA-AuNPs, (b) BSA-AuNPs at the ultrasound focal plane.

The focused ultrasound system was tested for a possible application regarding the internalization of TGA@CdTe QD and AuNPs into human cells during the incubation period. The state of the cells is evaluated after a one-hour incubation with and without ultrasound treatment. The cells showed to retain their physical structure however specific cellular metabolism tests should be conducted in the future. Both nanoparticles TGA@CdTe QD and AuNPs had higher elemental presence within the cell in the case of receiving treatment with focused ultrasound. However, given the low ultrasound power in the focal plane, the standard deviation of the results is very high and an optimization of the power is needed to confirm this result. Also the use of microbubble generating agents is needed to fully exploit the potential of this setup. Given that the internalization of the TGA@CdTe QD does not occur by endocytosis in these cells, it will be relevant and novel to study the effects of sonoporation in this particular biological system.

Currently, researchers worldwide are working on mechanisms that modify the uptake of engineered nanomaterials into cells for medical applications. One of such methods is focused ultrasound and the effect of cell sonoporation is a topic of increasing interest. In our country there are currently no facilities that have high-intensity focused ultrasound systems for medical applications. In this work the first steps in the experimental design and instrumentation of a focused ultrasound system are given. Preliminary results show that the equipment has the potential to for cell sonoporation experiments in the future.

Appendix B

Statistical and experimental description of microscopy and spectroscopy for cells and tissues

Photoluminescence spectroscopy

a) *Haematococcus pluvialis* microalgae cells

Following the protocol that was presented in Chapter Three, one sample of HPM, SHPM, HPM-QD and HPM-QD/AuNPs, and SHPM-QD and SHPM-QD/AuNPs have been prepared under room temperature. The samples were placed in quartz cells and gently stirred to avoid precipitation of microalgae in the bottom of the cell during measurements. Four to five spectra were acquired, all have similar characteristics. The spectra shown in figure 16 correspond to those that had a higher signal to noise ratio.

Bright field and fluorescence microscopy

a) *Haematococcus pluvialis* microalgae cells

Once again, following the protocol that was presented in Chapter Three, three samples of HPM, SHPM, HPM-QD, HPM-QD/AuNPs, SHPM-QD and SHPM-QD/AuNPs have been prepared. Thus a total of 18 samples were analyzed. On average, 5 images were acquired for each sample. Each image shows about 5 microalgae. A general trend for each type of sample was observed in the images, and this trend is what was discussed above. The only sample that shows considerable variations is the HPM-QD sample, where for one of the preparations, the number of nonviable cells (total structural loss) exceeded the number of intact specimens.

b) Human oral epithelial cells

Following the protocol that was presented in Chapter Three, 15 samples of OEC, OEC-QD, OEC-BSA-QD and OEC-BSA-QD-AuNPs have been prepared. Thus a total of 60 samples were analyzed. On average, 8 images were acquired for each sample. Each image shows about 4 OECs. A general trend for each type of sample was observed in the images, and this trend is what was discussed above.

Confocal microscopy

a) *Haematococcus pluvialis* microalgae cells

As for bright field microscopy, three samples of HPM, SHPM, HPM-QD and SHPM-QD have been prepared. Thus a total of 12 samples were analyzed. On average, 5 images were acquired for each sample. Each image shows one or two microalgae. A general trend for each type of sample was observed in the images, and this trend is what was discussed above. As before, the HPM-QD sample presented variations, where for one of the preparations, the number of nonviable cells (total structural loss) exceeded the number of intact specimens.

b) Human oral epithelial cells

Following the protocol that was presented in Chapter Three, one sample of OEC, OEC-BSA-QD and OEC-BSA-QD-NucBlue have been prepared. Thus a total of four samples were analyzed. On average, 4 images were acquired for each sample. Each image shows about one OECs. A general trend for each type of sample was observed in the images, and this trend is what was discussed above.

Scanning electron microscopy

a) *Haematococcus pluvialis* microalgae cells

Three samples of HPM, SHPM, HPM-QD, HPM-QD/AuNPs, SHPM-QD and SHPM-QD/AuNPs have been prepared. Thus a total of 18 samples were analyzed. On average, 5 images were acquired for each sample. Each image shows about 5 microalgae. A general trend for each type of sample was observed in the images, and this trend is what was discussed above. As before, the HPM-QD sample showed considerable variations, where for one of the preparations, the number of nonviable cells (total structural loss) exceeded the number of intact specimens. EDS elemental analysis was performed for three individual cells as described in Chapter Three.

b) Human oral epithelial cells

Following the protocol that was presented in Chapter Three, 15 samples of OEC, OEC-QD, OEC-BSA-QD and OEC-BSA-QD-AuNPs have been prepared. Thus a total of 60 samples were analyzed. On average, 8 images were acquired for each sample. Each image shows about 4 OECs. A general trend for each type of sample was observed in the images, and this trend is what was discussed above. As in the case of microalgae cells EDS elemental analysis was performed for three individual cells as described in Chapter Three.

STEM

One sample of OEC-BSA-QD and OEC-BSA-QD-AuNPs have been prepared following the protocol presented in Chapter Three. A pellet of approximately 100 μ l was obtained and fixed in the resin. Ultrathin sections (100 nm) were obtained with an ultramicrotome which were mounted in consecutive order on a grid. A total of 20 images were obtained and analyzed. Each image contained a complete cell or a fragment of interest.

c) Glandular breast tissue (EDS)

To observe the distribution of gold in the glandular breast tissue samples after having been breaded with Au/SiO₂ powder or incubated with naked AuNPs, EDS analysis was performed. Two samples obtained from a biopsy fragment of normal and cancerous glandular breast tissue were considered. A total of four biopsy fragments were analyzed and map readings (square geometry with side length of 10 μ m) were performed on each sample.

d) Dentin tissue

SEM micrographs of dentinal tissue have been acquired to gain a structural understanding at the microscopic level and properly correlate each tissue sample with its Raman spectrum. Two samples of dentinal tissue and dentinal tissue breaded with Au/SiO₂ powder or incubated with naked AuNPs were prepared and a total of 15 images were acquired and analyzed.

Raman spectroscopy

Raman spectrum of cells and tissues may change depending on the acquisition position. This study aims to give a general overview of the considered samples, not an interpretation for specific points; that is why a mapping was performed for each sample. As an example, the analysis performed for OEC is presented, the procedure for the other samples and tissues is analogous. This mapping was performed according to the grid shown in figure B1. Where figure B1 (a) shows two spectra obtained at different positions (1 and 2) of the same cell of an OEC–BSA- AuNPs sample, indicated in the image of the cell at the middle of the figure. In the same way figure B1 (b) shows two spectra obtained at different points of the same cell of an OEC–BSA-QDs- AuNPs sample. At each intersection of the grid superimposed on the image of the cells (figure B1) the Raman spectrum was acquired. As shown in the figure, the spectrum taken at a certain position differs from that taken in another place of the same cell. In figure B1 (a) and (b) circles indicate peaks present in each of these spectra that are also present in the average spectrum. While stars mark those peaks that differ and therefore we assume that these peaks are specific of the measurement point.

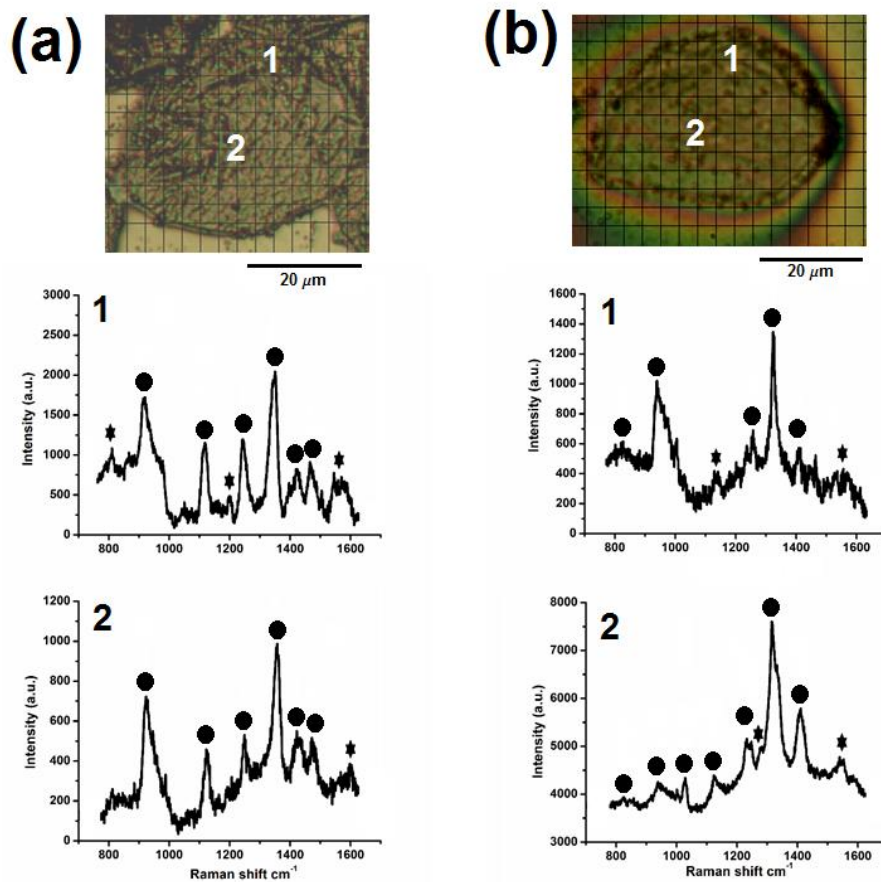


Figure B1. (a) Two spectra obtained at different points (1 and 2) of the same cell of an OEC-BSA-AuNPs sample indicated in the image of the cell at the middle of the figure. (b) Two spectra obtained at different points (1 and 2) of the same cell (1 and 2) of an OEC-BSA-QDs-AuNPs sample as indicated in the image of the cell at the middle of the figure. Circles indicate peaks present in each of these spectra that are also present in the average spectrum. While stars mark those peaks that are not present in the average spectrum.

In order to give an overview; in this study, a custom Matlab algorithm was developed in order to obtain an average spectrum that reflects the average characteristics of each sample. Therefore, the Raman spectra shown in shown throughout the dissertation correspond to the resulting average spectra. The Matlab code searches the position of the peaks in each spectrum and outputs an average intensity for each peak present in the considered spectra, therefore peak contributions due to a specific place in the cell tend to disappear the greater the number of spectra considered while the peaks appearing in most of the spectra consolidate their place in the average.

a) *Haematococcus pluvialis* microalgae cells

Three samples of HPM, SHPM, HPM-QD, HPM-QD/AuNPs, SHPM-QD and SHPM-QD/AuNPs have been prepared. Thus a total of 18 samples were analyzed. On average, 450 Raman spectra were acquired for each sample. The representative Raman spectra of each sample was found as described above.

b) Human oral epithelial cells

Following the protocol that was presented in Chapter Three, 15 samples of OEC, OEC-QD, OEC-BSA-QD and OEC-BSA-QD-AuNPs have been prepared. Thus a total of 60 samples were analyzed. On average, 2250 Raman spectra were acquired for each sample. About 1000 were selected considering the clarity and the signal to-noise ratio. The representative Raman spectra of each sample was found as described above. Since in this case no standardized cells were used, an additional statistical analysis shown below was performed.

The results of this analysis are summarized in Tables B1 and B2. Table B1 refers to the statistic for the spectrum found for OEC-BSA- AuNPs samples. Column B refers to the percentage of times that the peak indicated in column A appears considering all acquired spectra for the OEC-BSA- AuNPs samples. Column C shows the average peak width. Column D shows the standard deviation of the peak maximum and column E shows the relative average strength of the peak. The second section of the table shows the same analysis on the OEC-BSA- AuNPs spectrum but considering the peaks found for OEC-BSA-QDs-AuNPs.

Table B1. Statistic for the spectra found for OEC–BSA- AuNPs samples. Column B refers to the percentage of times that the peak indicated in column A appears. Column C shows the average peak width. Column D shows the standard deviation of the peak maximum and column E shows the relative average strength of the peak. The second section of the table shows the same analysis on the OEC–BSA- AuNPs spectrum but considering the peaks found for OEC–BSA-QDs- AuNPs.

A	B	C	D	E
Peak (cm ⁻¹)	Percentage of appearance in spectra (%)	Mean width (cm ⁻¹)	Standard deviation (cm ⁻¹)	Relative strength
Average peaks for OEC–BSA- AuNPs sample				
918	100	38	3	Strong
1120	100	25	3	Strong
1246	100	25	4	Strong
1353	100	29	4	Very strong
1433	90	40	3	Strong
1470	90	30	1	Strong
Average peaks for OEC–BSA-QDs- AuNPs sample				
845	0	--	--	--
938	0	--	--	--
1030	10	33	5	Very weak
1253	20	Sh.	--	Very weak
1322	10	Sh.	--	Very weak
1407	0	--	--	--

Sh. Found as shoulder.

Similar to Table B1, Table B2 refers to the statistic for the spectra found for OEC–BSA-QDs- AuNPs samples.

Table B2. Statistic for the spectra found for OEC–BSA-QDs- AuNPs samples. Column B refers to the percentage of times that the peak indicated in column A appears. Column C shows the average peak width. Column D shows the standard deviation of the peak maximum and column E shows the relative average strength of the peak. The second section of the table shows the same analysis on the OEC–BSA-QDs- AuNPs spectrum but considering the peaks found for OEC–BSA-AuNPs.

A	B	C	D	E
Peak (cm ⁻¹)	Percentage of appearance in spectra	Mean width (cm ⁻¹)	Standard deviation (cm ⁻¹)	Relative strength
Average peaks of OEC–BSA-QDs- AuNPs sample				
845	60	29	4	Weak
938	90	38	3	Weak
1030	80	20	2	Weak
1120	100	36	2	Weak
1253	50	24	4	Weak
1322	100	34	3	Very Strong
1407	90	19	4	Strong
Average peaks of OEC–BSA- AuNPs sample				
918	0	--	--	--
1246	0	--	--	--
1353	20	Sh.	--	Weak
1433	30	30	6	Weak
1470	0	--	--	--

Sh. Found as shoulder.

c) Glandular breast tissue

Three samples obtained from biopsy fragments of normal and cancerous glandular breast tissue before and after being breaded with Au/SiO₂ powder or incubated with naked AuNPs were considered. A total of six biopsy fragments were analyzed by Raman spectroscopy, of which 70 spectra of normal tissue and 80 of malignant lesions diagnosed as adenocarcinoma were considered.

d) Dentin tissue

Six samples from the same specimen of dentinal tissue and dentinal tissue breaded with Au/SiO₂ powder or incubated with naked AuNPs were considered. A total of 150 Raman spectra were acquired and analyzed.

Enhancement factors

The enhancement factors were calculated after fluorescence background subtraction from the representative average spectrum obtained as explained above. The integration interval of each peak was determined by the average width of the selected peak. Table B3 shows the enhancement factor values obtained for the strongest peaks from the average Raman spectrum of OEC. Considering the entire spectrum range (800-1600 cm^{-1}) ASERS= 4303890 and AREF= 608, thus $E \approx 7 \times 10^3$. The largest enhancement factor found for a given peak for the representative average spectrum is $\sim 8.6 \times 10^3$.

Table B3 Enhancement factor values obtained for the strongest peaks from the average Raman spectra of OEC.

Peak position (cm^{-1})	ASERS (a.u.)	AREF (a.u.)	$E = (\text{ASERS}) / (\text{AREF})$
1120	179631	42	4277
1246	132687	26	5103
1353	292852	34	8613

References

1. E. Cepeda-Pérez, I. Aguilar-Hernández, T. López-Luke, V. Piazza, R. Carriles, N. Ornelas-Soto and E. de la Rosa, "Interaction of Tga@Cdte Quantum Dots with an Extracellular Matrix of Haematococcus Pluvialis Microalgae Detected Using Surface-Enhanced Raman Spectroscopy (Sers)", *Applied Spectroscopy*, 2016, DOI: 10.1177/0003702816654076.
2. E. Cepeda-Pérez, T. López-Luke, G. Plascencia-Villa, L. Perez-Mayen, A. Ceja-Fdez, A. Ponce, J. Vivero-Escoto and E. Rosa, "Sers and Integrative Imaging Upon Internalization of Quantum Dots into Human Oral Epithelial Cells", *Journal of biophotonics*, 2016.
3. E. Cepeda-Pérez, T. López-Luke, P. Salas, G. Plascencia-Villa, A. Ponce, J. Vivero-Escoto, M. José-Yacamán and E. de la Rosa, "Sers-Active Au/Sio2 Clouds in Powder for Rapid Ex Vivo Breast Adenocarcinoma Diagnosis", *Biomedical Optics Express*, 2016, **7**, 2407-2418.
4. E. Cepeda-Pérez, Masters, UNAM, 2012.
5. C. Anthony Le, S. Alyona and N. Igor, "Biological Applications of Cadmium Telluride Semiconductor Quantum Dots", in *Cadmium Telluride Quantum Dots*, Pan Stanford Publishing, 2013, vol. -, ch. 6, pp. 173-204.
6. V. L. Colvin, "The Potential Environmental Impact of Engineered Nanomaterials", *Nature biotechnology*, 2003, **21**, 1166-1170.
7. S. Paul, C. Pearson, A. Molloy, M. Cousins, M. Green, S. Kolliopoulou, P. Dimitrakis, P. Normand, D. Tsoukalas and M. Petty, "Langmuir-Blodgett Film Deposition of Metallic Nanoparticles and Their Application to Electronic Memory Structures", *Nano Letters*, 2003, **3**, 533-536.
8. M. P. Sk, A. Jaiswal, A. Paul, S. S. Ghosh and A. Chattopadhyay, "Presence of Amorphous Carbon Nanoparticles in Food Caramels", *Scientific reports*, 2012, **2**.
9. K. S. Soppimath, T. M. Aminabhavi, A. R. Kulkarni and W. E. Rudzinski, "Biodegradable Polymeric Nanoparticles as Drug Delivery Devices", *Journal of controlled release*, 2001, **70**, 1-20.
10. Y. Wang, A.-J. Miao, J. Luo, Z.-B. Wei, J.-J. Zhu and L.-Y. Yang, "Bioaccumulation of Cdte Quantum Dots in a Freshwater Alga Ochromonas Danica: A Kinetics Study", *Environmental science & technology*, 2013, **47**, 10601-10610.
11. J. L. West and N. J. Halas, "Engineered Nanomaterials for Biophotonics Applications: Improving Sensing, Imaging, and Therapeutics", *Annual Review of Biomedical Engineering*, 2003, **5**, 285-292.
12. M. De, P. S. Ghosh and V. M. Rotello, "Applications of Nanoparticles in Biology", *Advanced Materials*, 2008, **20**, 4225-4241.
13. K. L. Dreher, "Health and Environmental Impact of Nanotechnology: Toxicological Assessment of Manufactured Nanoparticles", *Toxicological Sciences*, 2004, **77**, 3-5.
14. M. Liong, J. Lu, M. Kovichich, T. Xia, S. G. Ruehm, A. E. Nel, F. Tamanoi and J. I. Zink, "Multifunctional Inorganic Nanoparticles for Imaging, Targeting, and Drug Delivery", *ACS nano*, 2008, **2**, 889-896.
15. T. Wang, J. Bai, X. Jiang and G. U. Nienhaus, "Cellular Uptake of Nanoparticles by Membrane Penetration: A Study Combining Confocal Microscopy with Ftir Spectroelectrochemistry", *ACS nano*, 2012, **6**, 1251-1259.
16. L. Lou, K. Yu, Z. Zhang, B. Li, J. Zhu, Y. Wang, R. Huang and Z. Zhu, "Functionalized Magnetic-Fluorescent Hybrid Nanoparticles for Cell Labelling", *Nanoscale*, 2011, **3**, 2315-2323.
17. A. Verma, O. Uzun, Y. Hu, Y. Hu, H.-S. Han, N. Watson, S. Chen, D. J. Irvine and F. Stellacci, "Surface-Structure-Regulated Cell-Membrane Penetration by Monolayer-Protected Nanoparticles", *Nature materials*, 2008, **7**, 588-595.

18. F. Yuriel Núñez and I. V. Mikhail, "Optical Properties of Bulk and Nanocrystalline Cadmium Telluride", in *Cadmium Telluride Quantum Dots*, Pan Stanford Publishing, 2013, vol. -, ch. 1, pp. 1-22.
19. G. Iyer, F. Pinaud, J. Tsay and S. Weiss, "Solubilization of Quantum Dots with a Recombinant Peptide from Escherichia Coli", *Small*, 2007, **3**, 793-798.
20. M. Nurunnabi, K. J. Cho, J. S. Choi, K. M. Huh and Y.-k. Lee, "Targeted near-Ir Qds-Loaded Micelles for Cancer Therapy and Imaging", *Biomaterials*, 2010, **31**, 5436-5444.
21. W. Yvonne, C. Jennifer and V. Yuri, "Biocompatibility and Cellular Localisation of Cdte Quantum Dots", in *Cadmium Telluride Quantum Dots*, Pan Stanford Publishing, 2013, vol. -, ch. 7, pp. 205-229.
22. K. Boldt, O. T. Bruns, N. Gaponik and A. Eychmüller, "Comparative Examination of the Stability of Semiconductor Quantum Dots in Various Biochemical Buffers", *The Journal of Physical Chemistry B*, 2006, **110**, 1959-1963.
23. L. Balan, J. Lambert and C. Merlin, "The Exposure of Bacteria to Cdte-Core Quantum Dots: The Importance of Surface Chemistry on Cytotoxicity", *Nanotechnology*, 2009, **20**, 225101.
24. J. Lovrić, H. S. Bazzi, Y. Cuie, G. R. Fortin, F. M. Winnik and D. Maysinger, "Differences in Subcellular Distribution and Toxicity of Green and Red Emitting Cdte Quantum Dots", *Journal of Molecular Medicine*, 2005, **83**, 377-385.
25. G. Nikolai, "Assemblies of Thiol-Capped Cdte Nanocrystals", in *Cadmium Telluride Quantum Dots*, Pan Stanford Publishing, 2013, vol. -, ch. 3.
26. A. Verma and F. Stellacci, "Effect of Surface Properties on Nanoparticle–Cell Interactions", *Small*, 2010, **6**, 12-21.
27. P. Zrazhevskiy and X. Gao, "Quantum Dot Imaging Platform for Single-Cell Molecular Profiling", *Nature communications*, 2013, **4**, 1619.
28. A. Shiohara, S. Prabakar, A. Faramus, C.-Y. Hsu, P.-S. Lai, P. T. Northcote and R. D. Tilley, "Sized Controlled Synthesis, Purification, and Cell Studies with Silicon Quantum Dots", *Nanoscale*, 2011, **3**, 3364-3370.
29. D. V. Talapin, A. L. Rogach, E. V. Shevchenko, A. Kornowski, M. Haase and H. Weller, "Dynamic Distribution of Growth Rates within the Ensembles of Colloidal Ii-Vi and Iii-V Semiconductor Nanocrystals as a Factor Governing Their Photoluminescence Efficiency", *Journal of the American Chemical Society*, 2002, **124**, 5782-5790.
30. C. Pan, C. Kumar, S. Bohl, U. Klingmueller and M. Mann, "Comparative Proteomic Phenotyping of Cell Lines and Primary Cells to Assess Preservation of Cell Type-Specific Functions", *Molecular & Cellular Proteomics*, 2009, **8**, 443-450.
31. J. R. Masters, "Human Cancer Cell Lines: Fact and Fantasy", *Nature reviews Molecular cell biology*, 2000, **1**, 233-236.
32. J. R. Masters, "Hela Cells 50 Years On: The Good, the Bad and the Ugly", *Nature Reviews Cancer*, 2002, **2**, 315-319.
33. T. J. Stewart, J. Szlachetko, L. Sigg, R. Behra and M. Nachtgeal, "Tracking the Temporal Dynamics of Intracellular Lead Speciation in a Green Alga", *Environmental Science & Technology*, 2015, DOI: 10.1021/acs.est.5b02603.
34. S. Boussiba, "Carotenogenesis in the Green Alga Haematococcus Pluvialis: Cellular Physiology and Stress Response", *Physiologia Plantarum*, 2000, **108**, 111-117.
35. A. M. Collins, H. D. Jones, D. Han, Q. Hu, T. E. Beechem and J. A. Timlin, "Carotenoid Distribution in Living Cells of Haematococcus Pluvialis (Chlorophyceae)", *PloS one*, 2011, **6**, e24302.
36. A. Kaczor, K. Turnau and M. Baranska, "In Situ Raman Imaging of Astaxanthin in a Single Microalgal Cell", *Analyst*, 2011, **136**, 1109-1112.
37. M. Kobayashi, Y. Kurimura and Y. Tsuji, "Light-Independent, Astaxanthin Production by the Green Microalga Haematococcus Pluvialis under Salt Stress", *Biotechnology letters*, 1997, **19**, 507-509.

38. C. Hagen, S. Siegmund and W. Braune, "Ultrastructural and Chemical Changes in the Cell Wall of *Haematococcus Pluvialis* (Volvocales, Chlorophyta) During Aplanospore Formation", *European Journal of Phycology*, 2002, **37**, 217-226.
39. M. Wayama, S. Ota, H. Matsuura, N. Nango, A. Hirata and S. Kawano, "Three-Dimensional Ultrastructural Study of Oil and Astaxanthin Accumulation During Encystment in the Green Alga *Haematococcus Pluvialis*", *PLOS one*, 2013, **8**, e53618.
40. E. Morelli, P. Cioni, M. Posarelli and E. Gabellieri, "Chemical Stability of Cdse Quantum Dots in Seawater and Their Effects on a Marine Microalga", *Aquatic Toxicology*, 2012, **122**, 153-162.
41. E. Morelli, E. Salvadori, R. Bizzarri, P. Cioni and E. Gabellieri, "Interaction of Cdse/Zns Quantum Dots with the Marine Diatom *Phaeodactylum Tricornutum* and the Green Alga *Dunaliella Tertiolecta*: A Biophysical Approach", *Biophysical chemistry*, 2013, **182**, 4-10.
42. D. Han, J. Wang, M. Sommerfeld and Q. Hu, "Susceptibility and Protective Mechanisms of Motile and Non Motile Cells of *Haematococcus Pluvialis* (Chlorophyceae) to Photooxidative Stress1", *Journal of Phycology*, 2012, **48**, 693-705.
43. S. Lin, P. Bhattacharya, N. C. Rajapakse, D. E. Brune and P. C. Ke, "Effects of Quantum Dots Adsorption on Algal Photosynthesis", *The Journal of Physical Chemistry C*, 2009, **113**, 10962-10966.
44. A. Periasamy, *Methods in Cellular Imaging*, Springer, 2013.
45. L. W. Zhang and N. A. Monteiro-Riviere, "Mechanisms of Quantum Dot Nanoparticle Cellular Uptake", *Toxicological Sciences*, 2009, **110**, 138-155.
46. A. M. Schrand, J. J. Schlager, L. Dai and S. M. Hussain, "Preparation of Cells for Assessing Ultrastructural Localization of Nanoparticles with Transmission Electron Microscopy", *nature protocols*, 2010, **5**, 744-757.
47. G. S. Bumbrah and R. M. Sharma, "Raman Spectroscopy—Basic Principle, Instrumentation and Selected Applications for the Characterization of Drugs of Abuse", *Egyptian Journal of Forensic Sciences*, 2015.
48. D. C. Harris and M. D. Bertolucci, *Symmetry and Spectroscopy: An Introduction to Vibrational and Electronic Spectroscopy*, Courier Corporation, 1978.
49. R. Manoharan, Y. Wang and M. S. Feld, "Histochemical Analysis of Biological Tissues Using Raman Spectroscopy", *Spectrochimica Acta Part A: Molecular and Biomolecular Spectroscopy*, 1996, **52**, 215-249.
50. E. Le Ru and P. Etchegoin, *Principles of Surface-Enhanced Raman Spectroscopy: And Related Plasmonic Effects*, Elsevier, 2008.
51. I. R. Lewis and H. Edwards, *Handbook of Raman Spectroscopy: From the Research Laboratory to the Process Line*, CRC Press, 2001.
52. K. Kneipp, H. Kneipp and J. Kneipp, "Surface-Enhanced Raman Scattering in Local Optical Fields of Silver and Gold Nanoaggregates from Single-Molecule Raman Spectroscopy to Ultrasensitive Probing in Live Cells", *Accounts of chemical research*, 2006, **39**, 443-450.
53. Y. Liu, H. Miyoshi and M. Nakamura, "Nanomedicine for Drug Delivery and Imaging: A Promising Avenue for Cancer Therapy and Diagnosis Using Targeted Functional Nanoparticles", *International Journal of Cancer*, 2007, **120**, 2527-2537.
54. J. Oh, M. D. Feldman, J. Kim, C. Condit, S. Emelianov and T. E. Milner, "Detection of Magnetic Nanoparticles in Tissue Using Magneto-Motive Ultrasound", *Nanotechnology*, 2006, **17**, 4183.
55. A. G. Rockall, S. A. Sohaib, M. G. Harisinghani, S. A. Babar, N. Singh, A. R. Jeyarajah, D. H. Oram, I. J. Jacobs, J. H. Shepherd and R. H. Reznick, "Diagnostic Performance of Nanoparticle-Enhanced Magnetic Resonance Imaging in the Diagnosis of Lymph Node Metastases in Patients with Endometrial and Cervical Cancer", *Journal of Clinical Oncology*, 2005, **23**, 2813-2821.

56. S. H. Nam, Y. M. Bae, Y. I. Park, J. H. Kim, H. M. Kim, J. S. Choi, K. T. Lee, T. Hyeon and Y. D. Suh, "Long-Term Real-Time Tracking of Lanthanide Ion Doped Upconverting Nanoparticles in Living Cells", *Angewandte Chemie*, 2011, **123**, 6217-6221.
57. G. Plascencia-Villa, D. Bahena, A. R. Rodríguez, A. Ponce and M. José-Yacamán, "Advanced Microscopy of Star-Shaped Gold Nanoparticles and Their Adsorption-Uptake by Macrophages", *Metallomics*, 2013, **5**, 242-250.
58. G. Plascencia-Villa, C. R. Starr, L. S. Armstrong, A. Ponce and M. José-Yacamán, "Imaging Interactions of Metal Oxide Nanoparticles with Macrophage Cells by Ultra-High Resolution Scanning Electron Microscopy Techniques", *Integrative Biology*, 2012, **4**, 1358-1366.
59. A. C. S. Talari, Z. Movasaghi, S. Rehman and I. u. Rehman, "Raman Spectroscopy of Biological Tissues", *Applied Spectroscopy Reviews*, 2015, **50**, 46-111.
60. A. S. Haka, K. E. Shafer-Peltier, M. Fitzmaurice, J. Crowe, R. R. Dasari and M. S. Feld, "Diagnosing Breast Cancer by Using Raman Spectroscopy", *Proceedings of the National Academy of Sciences of the United States of America*, 2005, **102**, 12371-12376.
61. L. Pérez-Mayen, J. Oliva, A. Torres-Castro and E. De la Rosa, "Sers Substrates Fabricated with Star-Like Gold Nanoparticles for Zeptomole Detection of Analytes", *Nanoscale*, 2015, **7**, 10249-10258.
62. A. Ceja-Fdez, T. López-Luke, A. Torres-Castro, D. A. Wheeler, J. Z. Zhang and E. De la Rosa, "Glucose Detection Using Sers with Multi-Branched Gold Nanostructures in Aqueous Medium", *RSC Advances*, 2014, **4**, 59233-59241.
63. K. Kneipp, M. Moskovits and H. Kneipp, *Surface-Enhanced Raman Scattering: Physics and Applications*, Springer Science & Business Media, 2006.
64. J. Kneipp, H. Kneipp and K. Kneipp, "Sers—a Single-Molecule and Nanoscale Tool for Bioanalytics", *Chemical Society Reviews*, 2008, **37**, 1052-1060.
65. S. L. Kleinman, R. R. Frontiera, A.-I. Henry, J. A. Dieringer and R. P. Van Duyne, "Creating, Characterizing, and Controlling Chemistry with Sers Hot Spots", *Physical Chemistry Chemical Physics*, 2013, **15**, 21-36.
66. X.-M. Qian and S. Nie, "Single-Molecule and Single-Nanoparticle Sers: From Fundamental Mechanisms to Biomedical Applications", *Chemical Society Reviews*, 2008, **37**, 912-920.
67. L.-Y. Chen, K.-H. Yang, H.-C. Chen, Y.-C. Liu, C.-H. Chen and Q.-Y. Chen, "Innovative Fabrication of a Au Nanoparticle-Decorated Sio₂ Mask and Its Activity on Surface-Enhanced Raman Scattering", *Analyst*, 2014, **139**, 1929-1937.
68. A. Jemal, F. Bray, M. M. Center, J. Ferlay, E. Ward and D. Forman, "Global Cancer Statistics", *CA: a cancer journal for clinicians*, 2011, **61**, 69-90.
69. S. C. Robles and E. Galanis, "Breast Cancer in Latin America and the Caribbean", *Revista Panamericana de Salud Pública*, 2002, **11**, 178-185.
70. H. Tsuda and J. Arends, "Raman Spectroscopy in Dental Research: A Short Review of Recent Studies", *Advances in Dental Research*, 1997, **11**, 539-547.
71. K. Schulze, M. Balooch, G. Balooch, G. Marshall and S. Marshall, "Micro-Raman Spectroscopic Investigation of Dental Calcified Tissues", *Journal of Biomedical Materials Research Part A*, 2004, **69**, 286-293.
72. E. Hals and K. Selvig, "Correlated Electron Probe Microanalysis and Microradiography of Carious and Normal Dental Cementum", *Caries research*, 1977, **11**, 62-75.
73. N. Gaponik, D. V. Talapin, A. L. Rogach, K. Hoppe, E. V. Shevchenko, A. Kornowski, A. Eychmüller and H. Weller, "Thiol-Capping of Cdte Nanocrystals: An Alternative to Organometallic Synthetic Routes", *The Journal of Physical Chemistry B*, 2002, **106**, 7177-7185.
74. Z.-z. Sun, D. Ding, Q. Gong, W. Zhou, B. Xu and Z.-G. Wang, "Quantum-Dot Superluminescent Diode: A Proposal for an Ultra-Wide Output Spectrum", *Optical and Quantum Electronics*, 1999, **31**, 1235-1246.

75. D. Yao, Y. Liu, W. Zhao, H. Wei, X. Luo, Z. Wu, C. Dong, H. Zhang and B. Yang, "A Totally Phosphine-Free Synthesis of Metal Telluride Nanocrystals by Employing Alkylamides to Replace Alkylphosphines for Preparing Highly Reactive Tellurium Precursors", *Nanoscale*, 2013, **5**, 9593-9597.
76. W. W. Yu, L. Qu, W. Guo and X. Peng, "Experimental Determination of the Extinction Coefficient of Cdte, Cdse, and Cds Nanocrystals", *Chemistry of Materials*, 2003, **15**, 2854-2860.
77. J. K. Jaiswal, H. Mattoussi, J. M. Mauro and S. M. Simon, "Long-Term Multiple Color Imaging of Live Cells Using Quantum Dot Bioconjugates", *Nature biotechnology*, 2003, **21**, 47-51.
78. S. F. Wuister, I. Swart, F. van Driel, S. G. Hickey and C. de Mello Donegá, "Highly Luminescent Water-Soluble Cdte Quantum Dots", *Nano letters*, 2003, **3**, 503-507.
79. D. R. Larson, W. R. Zipfel, R. M. Williams, S. W. Clark, M. P. Bruchez, F. W. Wise and W. W. Webb, "Water-Soluble Quantum Dots for Multiphoton Fluorescence Imaging in Vivo", *Science*, 2003, **300**, 1434-1436.
80. M. N. Martin, J. I. Basham, P. Chando and S.-K. Eah, "Charged Gold Nanoparticles in Non-Polar Solvents: 10-Min Synthesis and 2d Self-Assembly", *Langmuir*, 2010, **26**, 7410-7417.
81. M. Hossain, Y. Kitahama, G. Huang, T. Kaneko and Y. Ozaki, "Spr and Sers Characteristics of Gold Nanoaggregates Withádifferent Morphologies", *Applied Physics B*, 2008, **93**, 165-170.
82. X. Liu, M. Atwater, J. Wang and Q. Huo, "Extinction Coefficient of Gold Nanoparticles with Different Sizes and Different Capping Ligands", *Colloids and Surfaces B: Biointerfaces*, 2007, **58**, 3-7.
83. A. Albanese and W. C. Chan, "Effect of Gold Nanoparticle Aggregation on Cell Uptake and Toxicity", *ACS nano*, 2011, **5**, 5478-5489.
84. B. Nikoobakht and M. A. El-Sayed, "Surface-Enhanced Raman Scattering Studies on Aggregated Gold Nanorods", *The Journal of Physical Chemistry A*, 2003, **107**, 3372-3378.
85. B. Nikoobakht, J. Wang and M. A. El-Sayed, "Surface-Enhanced Raman Scattering of Molecules Adsorbed on Gold Nanorods: Off-Surface Plasmon Resonance Condition", *Chemical Physics Letters*, 2002, **366**, 17-23.
86. A. K. Samal, T. S. Sreeprasad and T. Pradeep, "Investigation of the Role of Nabh 4 in the Chemical Synthesis of Gold Nanorods", *Journal of Nanoparticle Research*, 2010, **12**, 1777-1786.
87. N. R. Jana, L. Gearheart and C. J. Murphy, "Seed-Mediated Growth Approach for Shape-Controlled Synthesis of Spheroidal and Rod-Like Gold Nanoparticles Using a Surfactant Template", *Advanced Materials*, 2001, **13**, 1389.
88. P. R. Sajanlal, T. S. Sreeprasad, A. K. Samal and T. Pradeep, "Anisotropic Nanomaterials: Structure, Growth, Assembly, and Functions", *Nano reviews*, 2011, **2**, 5883_5881-5883_5862.
89. J. S. Kim, E. Kuk, K. N. Yu, J.-H. Kim, S. J. Park, H. J. Lee, S. H. Kim, Y. K. Park, Y. H. Park and C.-Y. Hwang, "Antimicrobial Effects of Silver Nanoparticles", *Nanomedicine: Nanotechnology, Biology and Medicine*, 2007, **3**, 95-101.
90. J. Guo, X. Liu, H. Gao, J. Bie, Y. Zhang, B. Liu and C. Sun, "Highly Sensitive Turn-on Fluorescent Detection of Cartap Via a Nonconjugated Gold Nanoparticle–Quantum Dot Pair Mediated by Inner Filter Effect", *RSC Advances*, 2014, **4**, 27228-27235.
91. L. Vladimir, G. Nikolai and E. Alexander, "Aqueous Synthesis of Colloidal Cdte Nanocrystals", in *Cadmium Telluride Quantum Dots*, Pan Stanford Publishing, 2013, vol. -, ch. 2, pp. 23-59.
92. X. Cui, M. Liu and B. Li, "Homogeneous Fluorescence-Based Immunoassay Via Inner Filter Effect of Gold Nanoparticles on Fluorescence of Cdte Quantum Dots", *Analyst*, 2012, **137**, 3293-3299.

93. J. Turkevich, G. Garton and P. Stevenson, "The Color of Colloidal Gold", *Journal of colloid Science*, 1954, **9**, 26-35.
94. W. Stöber, A. Fink and E. Bohn, "Controlled Growth of Monodisperse Silica Spheres in the Micron Size Range", *Journal of colloid and interface science*, 1968, **26**, 62-69.
95. X. Huang, X. Teng, D. Chen, F. Tang and J. He, "The Effect of the Shape of Mesoporous Silica Nanoparticles on Cellular Uptake and Cell Function", *Biomaterials*, 2010, **31**, 438-448.
96. W. Haiss, N. T. Thanh, J. Aveyard and D. G. Fernig, "Determination of Size and Concentration of Gold Nanoparticles from Uv-Vis Spectra", *Analytical chemistry*, 2007, **79**, 4215-4221.
97. N. G. Khlebtsov, "Determination of Size and Concentration of Gold Nanoparticles from Extinction Spectra", *Analytical chemistry*, 2008, **80**, 6620-6625.
98. J. Kimling, M. Maier, B. Okenve, V. Kotaidis, H. Ballot and A. Plech, "Turkevich Method for Gold Nanoparticle Synthesis Revisited", *The Journal of Physical Chemistry B*, 2006, **110**, 15700-15707.
99. H. Fan, K. Yang, D. M. Boye, T. Sigmon, K. J. Malloy, H. Xu, G. P. López and C. J. Brinker, "Self-Assembly of Ordered, Robust, Three-Dimensional Gold Nanocrystal/Silica Arrays", *Science*, 2004, **304**, 567-571.
100. V. Pol, A. Gedanken and J. Calderon-Moreno, "Deposition of Gold Nanoparticles on Silica Spheres: A Sonochemical Approach", *Chemistry of materials*, 2003, **15**, 1111-1118.
101. S. Oldenburg, R. Averitt, S. Westcott and N. Halas, "Nanoengineering of Optical Resonances", *Chemical Physics Letters*, 1998, **288**, 243-247.
102. M. Zhang, Y. Wu, X. Feng, X. He, L. Chen and Y. Zhang, "Fabrication of Mesoporous Silica-Coated Cnts and Application in Size-Selective Protein Separation", *Journal of Materials Chemistry*, 2010, **20**, 5835-5842.
103. L. Recht, A. Zarka and S. Boussiba, "Patterns of Carbohydrate and Fatty Acid Changes under Nitrogen Starvation in the Microalgae *Haematococcus Pluvialis* and *Nannochloropsis Sp*", *Applied microbiology and biotechnology*, 2012, **94**, 1495-1503.
104. A. Goldstein, Y. Soroka, M. FRUŠIĆ-ZLOTKIN, I. Popov and R. Kohen, "High Resolution Sem Imaging of Gold Nanoparticles in Cells and Tissues", *Journal of microscopy*, 2014, **256**, 237-247.
105. C. M. Krishna, G. Sockalingum, J. Kurien, L. Rao, L. Venteo, M. Pluot, M. Manfait and V. Kartha, "Micro-Raman Spectroscopy for Optical Pathology of Oral Squamous Cell Carcinoma", *Applied spectroscopy*, 2004, **58**, 1128-1135.
106. A. S. Kristoffersen, Ø. Svensen, N. Ssebiyonga, S. R. Erga, J. J. Stamnes and Ø. Frette, "Chlorophyll a and NADPH Fluorescence Lifetimes in the Microalgae *Haematococcus Pluvialis* (Chlorophyceae) under Normal and Astaxanthin-Accumulating Conditions", *Applied spectroscopy*, 2012, **66**, 1216-1225.
107. K. Kneipp, A. S. Haka, H. Kneipp, K. Badizadegan, N. Yoshizawa, C. Boone, K. E. Shafer-Peltier, J. T. Motz, R. R. Dasari and M. S. Feld, "Surface-Enhanced Raman Spectroscopy in Single Living Cells Using Gold Nanoparticles", *Applied Spectroscopy*, 2002, **56**, 150-154.
108. S. Singh, A. Sahu, A. Deshmukh, P. Chaturvedi and C. M. Krishna, "In Vivo Raman Spectroscopy of Oral Buccal Mucosa: A Study on Malignancy Associated Changes (Mac)/Cancer Field Effects (Cfe)", *Analyst*, 2013, **138**, 4175-4182.
109. Z. Han, J. Lu, Y. Liu, B. Davis, M. S. Lee, M. A. Olson, G. Ruthel, B. D. Freedman, M. J. Schnell and J. E. Wrobel, "Small-Molecule Probes Targeting the Viral Ppxy-Host Nedd4 Interface Block Egress of a Broad Range of RNA Viruses", *Journal of virology*, 2014, **88**, 7294-7306.
110. M. Chen and R. Lord, "Laser-Excited Raman Spectroscopy of Biomolecules. VIII. Conformational Study of Bovine Serum Albumin", *Journal of the American Chemical Society*, 1976, **98**, 990-992.

111. F. Franck, P. Juneau and R. Popovic, "Resolution of the Photosystem I and Photosystem II Contributions to Chlorophyll Fluorescence of Intact Leaves at Room Temperature", *Biochimica et Biophysica Acta (BBA)-Bioenergetics*, 2002, **1556**, 239-246.
112. P. Régnier, J. Bastias, V. Rodriguez-Ruiz, N. Caballero-Casero, C. Caballo, D. Sicilia, A. Fuentes, M. Maire, M. Crepin and D. Letourneur, "Astaxanthin from *Haematococcus Pluvialis* Prevents Oxidative Stress on Human Endothelial Cells without Toxicity", *Marine drugs*, 2015, **13**, 2857-2874.
113. Z. Wu, Y. Zhu, W. Huang, C. Zhang, T. Li, Y. Zhang and A. Li, "Evaluation of Flocculation Induced by pH Increase for Harvesting Microalgae and Reuse of Flocculated Medium", *Bioresource technology*, 2012, **110**, 496-502.
114. A. Tatyana, K. Min Seok, H. Jong Won, M. Taizo, N. Chikako and K. Gwang Hoon, "Cold-Tolerant Strain of *Haematococcus Pluvialis* (Haematococcaceae, Chlorophyta) from Blomstrandhalvøya (Svalbard)", *Algae*, 2013, **28**, 185-192.
115. P. Heraud, J. Beardall, D. McNaughton and B. R. Wood, "In Vivo Prediction of the Nutrient Status of Individual Microalgal Cells Using Raman Microspectroscopy", *FEMS microbiology letters*, 2007, **275**, 24-30.
116. B. R. Wood, P. Heraud, S. Stojkovic, D. Morrison, J. Beardall and D. McNaughton, "A Portable Raman Acoustic Levitation Spectroscopic System for the Identification and Environmental Monitoring of Algal Cells", *Analytical chemistry*, 2005, **77**, 4955-4961.
117. Z.-L. Cai, H. Zeng, M. Chen and A. W. Larkum, "Raman Spectroscopy of Chlorophyll D from *Acaryochloris Marina*", *Biochimica et Biophysica Acta (BBA)-Bioenergetics*, 2002, **1556**, 89-91.
118. X. Wei, D. Jie, J. J. Cuello, D. J. Johnson, Z. Qiu and Y. He, "Microalgal Detection by Raman Microspectroscopy", *TrAC Trends in Analytical Chemistry*, 2014, **53**, 33-40.
119. Y. Koyama, Y. Umemoto, A. Akamatsu, K. Uehara and M. Tanaka, "Raman Spectra of Chlorophyll Forms", *Journal of molecular structure*, 1986, **146**, 273-287.
120. I. Notingher, "Raman Spectroscopy Cell-Based Biosensors", *Sensors*, 2007, **7**, 1343-1358.
121. J. De Gelder, K. De Gussem, P. Vandenabeele and L. Moens, "Reference Database of Raman Spectra of Biological Molecules", *Journal of Raman Spectroscopy*, 2007, **38**, 1133-1147.
122. A. Kaczor and M. Baranska, "Structural Changes of Carotenoid Astaxanthin in a Single Algal Cell Monitored in Situ by Raman Spectroscopy", *Analytical chemistry*, 2011, **83**, 7763-7770.
123. Z. Pilát, S. Bernatová, J. Ježek, M. Šery, O. Samek, P. Zemánek, L. Nedbal and M. Trtílek, 2011.
124. C. Uragami, E. Yamashita, A. Gall, B. Robert and H. Hashimoto, "Application of Resonance Raman Microscopy to in Vivo Carotenoid", *Acta Biochimica Polonica*, 2012, **59**, 53.
125. J. C. Merlin, "Resonance Raman Spectroscopy of Carotenoids and Carotenoid-Containing Systems", *Pure and Applied Chemistry*, 1985, **57**, 785-792.
126. A. Dementjev and J. Kostkevičiene, "Applying the Method of Coherent Anti-Stokes Raman Microscopy for Imaging of Carotenoids in Microalgae and Cyanobacteria", *Journal of Raman Spectroscopy*, 2013, **44**, 973-979.
127. J. S. Mak, A. A. Farah, F. Chen and A. S. Helmy, "Photonic Crystal Fiber for Efficient Raman Scattering of CdTe Quantum Dots in Aqueous Solution", *ACS nano*, 2011, **5**, 3823-3830.
128. J. Zhao, Z. Zhang, Z. Yu, Z. He, S. Yang and H. Jiang, "Nucleation and Characterization of Hydroxyapatite on Thioglycolic Acid-Capped Reduced Graphene Oxide/Silver Nanoparticles in Simplified Simulated Body Fluid", *Applied Surface Science*, 2014, **289**, 89-96.
129. M. Josè-Estanyol and P. Puigdomènech, "Plant Cell Wall Glycoproteins and Their Genes", *Plant Physiology and Biochemistry*, 2000, **38**, 97-108.
130. A. Galat, "Study of the Raman Scattering and Infrared Absorption Spectra of Branched Polysaccharides", *Acta Biochimica Polonica*, 1980, **27**, 135-142.

131. J. Coulon, I. Thouvenin, F. Aldeek, L. Balan and R. Schneider, "Glycosylated Quantum Dots for the Selective Labelling of *Kluyveromyces Bulgaricus* and *Saccharomyces Cerevisiae* Yeast Strains", *Journal of fluorescence*, 2010, **20**, 591-597.
132. D. De Veld, M. Witjes, H. Sterenberg and J. Roodenburg, "The Status of in Vivo Autofluorescence Spectroscopy and Imaging for Oral Oncology", *Oral oncology*, 2005, **41**, 117-131.
133. G. L. Francis, "Albumin and Mammalian Cell Culture: Implications for Biotechnology Applications", *Cytotechnology*, 2010, **62**, 1-16.
134. I. Nabiev, S. Mitchell, A. Davies, Y. Williams, D. Kelleher, R. Moore, Y. K. Gun'ko, S. Byrne, Y. P. Rakovich and J. F. Donegan, "Nonfunctionalized Nanocrystals Can Exploit a Cell's Active Transport Machinery Delivering Them to Specific Nuclear and Cytoplasmic Compartments", *Nano Letters*, 2007, **7**, 3452-3461.
135. W. F. Ganong and K. E. Barrett, *Review of Medical Physiology*, McGraw-Hill Medical ^ eNew York New York, 2005.
136. B. Thorens, "Facilitated Glucose Transporters in Epithelial Cells", *Annual review of physiology*, 1993, **55**, 591-608.
137. L. Vitkov, W. D. Krautgartner, M. Hannig and K. Fuchs, "Fimbria-Mediated Bacterial Adhesion to Human Oral Epithelium", *FEMS microbiology letters*, 2001, **202**, 25-30.
138. M. Zhou and I. Ghosh, "Quantum Dots and Peptides: A Bright Future Together", *Peptide Science*, 2007, **88**, 325-339.
139. J. Weng, X. Song, L. Li, H. Qian, K. Chen, X. Xu, C. Cao and J. Ren, "Highly Luminescent Cdte Quantum Dots Prepared in Aqueous Phase as an Alternative Fluorescent Probe for Cell Imaging", *Talanta*, 2006, **70**, 397-402.
140. M. Yu, Y. Yang, R. Han, Q. Zheng, L. Wang, Y. Hong, Z. Li and Y. Sha, "Polyvalent Lactose– Quantum Dot Conjugate for Fluorescent Labeling of Live Leukocytes", *Langmuir*, 2010, **26**, 8534-8539.
141. S. E. Gratton, P. A. Ropp, P. D. Pohlhaus, J. C. Luft, V. J. Madden, M. E. Napier and J. M. DeSimone, "The Effect of Particle Design on Cellular Internalization Pathways", *Proceedings of the National Academy of Sciences*, 2008, **105**, 11613-11618.
142. M. S. Cartiera, K. M. Johnson, V. Rajendran, M. J. Caplan and W. M. Saltzman, "The Uptake and Intracellular Fate of Plga Nanoparticles in Epithelial Cells", *Biomaterials*, 2009, **30**, 2790-2798.
143. S. Ge, C. Zhang, Y. Zhu, J. Yu and S. Zhang, "Bsa Activated Cdte Quantum Dot Nanosensor for Antimony Ion Detection", *Analyst*, 2010, **135**, 111-115.
144. P. Del Pino, B. Pelaz, Q. Zhang, P. Maffre, G. U. Nienhaus and W. J. Parak, "Protein Corona Formation around Nanoparticles–from the Past to the Future", *Materials Horizons*, 2014, **1**, 301-313.
145. D. B. DeOliveira, W. R. Trumble, H. K. Sarkar and B. R. Singh, "Secondary Structure Estimation of Proteins Using the Amide Iii Region of Fourier Transform Infrared Spectroscopy: Application to Analyze Calcium-Binding-Induced Structural Changes in Calsequestrin", *Applied spectroscopy*, 1994, **48**, 1432-1441.
146. A. Sahu, A. Deshmukh, A. Ghanate, S. Singh, P. Chaturvedi and C. M. Krishna, "Raman Spectroscopy of Oral Buccal Mucosa: A Study on Age-Related Physiological Changes and Tobacco-Related Pathological Changes", *Technology in cancer research & treatment*, 2012, **11**, 529-541.
147. H. H. Bragulla and D. G. Homberger, "Structure and Functions of Keratin Proteins in Simple, Stratified, Keratinized and Cornified Epithelia", *Journal of anatomy*, 2009, **214**, 516-559.
148. M. M. Weiser, "Intestinal Epithelial Cell Surface Membrane Glycoprotein Synthesis I. An Indicator of Cellular Differentiation", *Journal of Biological Chemistry*, 1973, **248**, 2536-2541.

149. S. C. Tseng, M. J. Jarvinen, W. G. Nelson, J.-W. Huang, J. Woodcock-Mitchell and T.-T. Sun, "Correlation of Specific Keratins with Different Types of Epithelial Differentiation: Monoclonal Antibody Studies", *Cell*, 1982, **30**, 361-372.
150. G. F. Springer, P. R. Desai and I. Banatwala, "Brief Communication: Blood Group Mn Antigens and Precursors in Normal and Malignant Human Breast Glandular Tissue", *Journal of the National Cancer Institute*, 1975, **54**, 335-339.
151. M. Çakır, T. Küçükartallar, A. Tekin, N. Selimoğlu, N. Poyraz, M. M. Belviranlı and A. Kartal, "Comparison of Mammography Sensitivity after Reduction Mammoplasty Targeting the Glandular and Fat Tissue", *Ulusal Cerrahi Dergisi*, 2015, **31**, 068-071.
152. Z. Huang, A. McWILLIAMS, S. Lam, J. English, D. I. McLEAN, H. Lui and H. Zeng, "Effect of Formalin Fixation on the near-Infrared Raman Spectroscopy of Normal and Cancerous Human Bronchial Tissues", *International journal of oncology*, 2003, **23**, 649-655.
153. J. C. Fanburg-Smith, J. M. Meis-Kindblom, R. Fante and L.-G. Kindblom, "Malignant Granular Cell Tumor of Soft Tissue: Diagnostic Criteria and Clinicopathologic Correlation", *The American journal of surgical pathology*, 1998, **22**, 779-794.
154. J. D. Hunt, A. Kavner, E. A. Schauble, D. Snyder and C. E. Manning, "Polymerization of Aqueous Silica in H₂O-K₂O Solutions at 25–200° C and 1bar to 20kbar", *Chemical Geology*, 2011, **283**, 161-170.
155. N. I. Afanasyeva, S. F. Kolyakov, V. G. Artiushenko, V. V. Sokolov and G. A. Frank, 1998.
156. K. E. Shafer-Peltier, A. S. Haka, M. Fitzmaurice, J. Crowe, J. Myles, R. R. Dasari and M. S. Feld, "Raman Microspectroscopic Model of Human Breast Tissue: Implications for Breast Cancer Diagnosis in Vivo", *Journal of Raman Spectroscopy*, 2002, **33**, 552-563.
157. H. Yuan, A. M. Fales, C. G. Khoury, J. Liu and T. Vo-Dinh, "Spectral Characterization and Intracellular Detection of Surface-Enhanced Raman Scattering (Sers)-Encoded Plasmonic Gold Nanostars", *Journal of Raman Spectroscopy*, 2013, **44**, 234-239.
158. J. W. Kang, P. T. So, R. R. Dasari and D.-K. Lim, "High Resolution Live Cell Raman Imaging Using Subcellular Organelle-Targeting Sers-Sensitive Gold Nanoparticles with Highly Narrow Intra-Nanogap", *Nano letters*, 2015, **15**, 1766-1772.
159. J. Jiang, K. Bosnick, M. Maillard and L. Brus, "Single Molecule Raman Spectroscopy at the Junctions of Large Ag Nanocrystals", *The Journal of Physical Chemistry B*, 2003, **107**, 9964-9972.
160. K. L. Kelly, E. Coronado, L. L. Zhao and G. C. Schatz, "The Optical Properties of Metal Nanoparticles: The Influence of Size, Shape, and Dielectric Environment", *The Journal of Physical Chemistry B*, 2003, **107**, 668-677.
161. T. Lopez-Luke, D. A. Wheeler, E. de la Rosa, A. Torres-Castro, S. A. Adams, L. S. Zavodivker and J. Z. Zhang, "Synthesis, Characterization and Surface Enhanced Raman Scattering of Hollow Gold–Silica Double Shell Nanostructures", *Biomedical Spectroscopy and Imaging*, 2012, **1**, 275-291.
162. H. Ali, M. Irwin, L. Morris, S. Dawson, F. Blows, E. Provenzano, B. Mahler-Araujo, P. Pharoah, N. Walton and J. Brenton, "Astronomical Algorithms for Automated Analysis of Tissue Protein Expression in Breast Cancer", *British journal of cancer*, 2013, **108**, 602-612.
163. Z. Movasaghi, S. Rehman and D. I. ur Rehman, "Fourier Transform Infrared (Ftir) Spectroscopy of Biological Tissues", *Applied Spectroscopy Reviews*, 2008, **43**, 134-179.
164. A. A. Vertegel, R. W. Siegel and J. S. Dordick, "Silica Nanoparticle Size Influences the Structure and Enzymatic Activity of Adsorbed Lysozyme", *Langmuir*, 2004, **20**, 6800-6807.
165. C. Young, S. Terada, J. Vacanti, M. Honda, J. Bartlett and P. Yelick, "Tissue Engineering of Complex Tooth Structures on Biodegradable Polymer Scaffolds", *Journal of dental research*, 2002, **81**, 695-700.
166. A. Nanci and D. D. Bosshardt, "Structure of Periodontal Tissues in Health and Disease*", *Periodontology 2000*, 2006, **40**, 11-28.

167. K. A. Selvig, "The Fine Structure of Human Cementum", *Acta Odontologica Scandinavica*, 1965, **23**, 423-441.
168. J. K. Avery and P. F. Steele, *Essentials of Oral Histology and Embryology: A Clinical Approach*, Mosby, 2006.
169. G. W. Marshall, S. J. Marshall, J. H. Kinney and M. Balooch, "The Dentin Substrate: Structure and Properties Related to Bonding", *Journal of dentistry*, 1997, **25**, 441-458.
170. I. Thesleff and M. Mikkola, "The Role of Growth Factors in Tooth Development", *International review of cytology*, 2002, **217**, 93-135.
171. D. Pashley, "Clinical Correlations of Dentin Structure and Function", *The Journal of prosthetic dentistry*, 1991, **66**, 777-781.
172. J. F. Esquivel-Upshaw, W. F. Rose, A. A. Barrett, E. R. Oliveira, M. C. Yang, A. E. Clark and K. J. Anusavice, "Three Years in Vivo Wear: Core-Ceramic, Veneers, and Enamel Antagonists", *Dental Materials*, 2012, **28**, 615-621.
173. M.-C. Lin, C. Lee, C. Lin, Y. Wu, H. Wang, C. Chen, F. Sung and C. Kao, "Dental Diagnostic X-Ray Exposure and Risk of Benign and Malignant Brain Tumors", *Annals of oncology*, 2013, **24**, 1675-1679.
174. S. Saha, C. Tomaro-Duchesneau, L. Rodes, M. Malhotra, M. Tabrizian and S. Prakash, "Investigation of Probiotic Bacteria as Dental Caries and Periodontal Disease Biotherapeutics", *Beneficial microbes*, 2014, **5**, 447-460.
175. R. M. Love, "Enterococcus Faecalis— a Mechanism for Its Role in Endodontic Failure", *International Endodontic Journal*, 2001, **34**, 399-405.
176. C. Robinson, "Dental Caries", in *Metabolism of Human Diseases*, Springer, 2014, pp. 87-92.
177. L. R. d. R. S. Costa, I.-S. WATANABE and M. C. Kronka, "Coronal Dentinal Tubules of Non-Erupted Deciduous Incisors", *Pesquisa Odontológica Brasileira*, 2002, **16**, 12-17.
178. S. Yang, B. Li, A. Akkus, O. Akkus and L. Lang, "Wide-Field Raman Imaging of Dental Lesions", *Analyst*, 2014, **139**, 3107-3114.
179. S. P. Ho, P. Senkyrikova, G. W. Marshall, W. Yun, Y. Wang, K. Karan, C. Li and S. J. Marshall, "Structure, Chemical Composition and Mechanical Properties of Coronal Cementum in Human Deciduous Molars", *dental materials*, 2009, **25**, 1195-1204.
180. Z. Fan, H. Liu, M. Mayer and C. X. Deng, "Spatiotemporally Controlled Single Cell Sonoporation", *Proceedings of the National Academy of Sciences*, 2012, **109**, 16486-16491.
181. T. Tran, S. Roger, J.-Y. Le Guennec, F. Tranquart and A. Bouakaz, "Effect of Ultrasound-Activated Microbubbles on the Cell Electrophysiological Properties", *Ultrasound in medicine & biology*, 2007, **33**, 158-163.
182. K. Kooiman, M. Foppen-Harteveld, A. F. van der Steen and N. de Jong, "Sonoporation of Endothelial Cells by Vibrating Targeted Microbubbles", *Journal of controlled release*, 2011, **154**, 35-41.
183. R. Dijkink, S. Le Gac, E. Nijhuis, A. van den Berg, I. Vermes, A. Poot and C.-D. Ohl, "Controlled Cavitation—Cell Interaction: Trans-Membrane Transport and Viability Studies", *Physics in medicine and biology*, 2007, **53**, 375.
184. N. Mizrahi, E. H. Zhou, G. Lenormand, R. Krishnan, D. Weihs, J. P. Butler, D. A. Weitz, J. J. Fredberg and E. Kimmel, "Low Intensity Ultrasound Perturbs Cytoskeleton Dynamics", *Soft matter*, 2012, **8**, 2438-2443.
185. G. Apodaca, "Modulation of Membrane Traffic by Mechanical Stimuli", *American Journal of Physiology-Renal Physiology*, 2002, **282**, F179-F190.
186. J. Hutcheson, R. Schlicher, H. Hicks and M. Prausnitz, "Saving Cells from Ultrasound-Induced Apoptosis: Quantification of Cell Death and Uptake Following Sonication and Effects of Targeted Calcium Chelation", *Ultrasound in medicine & biology*, 2010, **36**, 1008-1021.

187. A. Draeger, K. Monastyrskaya and E. B. Babiychuk, "Plasma Membrane Repair and Cellular Damage Control: The Annexin Survival Kit", *Biochemical pharmacology*, 2011, **81**, 703-712.
188. P. L. McNeil, "Cellular and Molecular Adaptations to Injurious Mechanical Stress", *Trends in cell biology*, 1993, **3**, 302-307.
189. T. Kono, T. Nishikori, H. Kataoka, Y. Uchio, M. Ochi and K. i. Enomoto, "Spontaneous Oscillation and Mechanically Induced Calcium Waves in Chondrocytes", *Cell biochemistry and function*, 2006, **24**, 103-111.
190. J. Guo, H. Li, M. Xue, M. Zhang, X. Cao, Y. Luo, F. Shen and C. Sun, "Highly Sensitive Detection of Organophosphorus Pesticides Represented by Methamidophos Via Inner Filter Effect of Au Nanoparticles on the Fluorescence of Cdte Quantum Dots", *Food Analytical Methods*, 2014, **7**, 1247-1255.
191. I. Zarazúa, E. De la Rosa, T. López-Luke, J. Reyes-Gomez, S. Ruiz, C. Angeles Chavez and J. Z. Zhang, "Photovoltaic Conversion Enhancement of Cdse Quantum Dot-Sensitized Tio₂ Decorated with Au Nanoparticles and P3ot", *The Journal of Physical Chemistry C*, 2011, **115**, 23209-23220.